Materials study for potassium-ion batteries : Mechanistic insights and full cell application

Phuong Nam Le Pham

THÈSE POUR OBTENIR LE GRADE DE DOCTEUR
DE L'UNIVERSITÉ DE MONTPELLIER

En Chimie et Physico-Chimie des Matériaux

École doctorale Sciences Chimiques Balard

Unité de recherche UMR 5253 – Institut Charles Gerhardt Montpellier

Materials study for potassium-ion batteries: Mechanistic insights and full cell application

Présentée par Phuong Nam LE PHAM
Le 15 Septembre 2022

Sous la direction de Lorenzo STIEVANO
Laure MONCONDUIT et Patrik JOHANSSON

Devant le jury composé de

William R. BRANT, Assoc. Pr., Uppsala University	Rapporteur
Matteo BIANCHINI, Pr., University of Bayreuth	Rapporteur
Laurence CROGUENNEC, Dr., ICMCB, CNRS Bordeaux	Examinatrice/ Présidente
Alessandro LONGO, Dr., ID20, ESRF	Examinateur
Patrik JOHANSSON, Pr., Chalmers University of Technology	Examinateur
Laure MONCONDUIT, Dr., ICGM, Université de Montpellier	Co-directrice de thèse
Lorenzo STIEVANO, Pr., IGCM, Université de Montpellier	Directeur de thèse

UNIVERSITÉ DE MONTPELLIER

ACKNOWLEDGEMENTS

The journey of my Ph.D. finally ends with this dissertation. Words are not enough to express my gratefulness for three years full adventures, new discoveries, happiness, and maturity.

First of all, I would like to thank Prof. Matteo Bianchini, Prof. William Brant, Dr. Laurance Croguennec and Dr. Alessandro Longo for accepting to evaluate my thesis and to participate in my dissertation. It was a great honor to discuss with you in more details about my work, from which I have a better view of the stories and self-reevaluate my strength and weakness for my career in the future.

A huge acknowledgement is devoted to ALISTORE group for my Ph.D. grant and TROPIC project for their support throughout my thesis research. Being a part of those association gives me great opportunities to meet amazing students and scientists out there and to have valuable scientific discussions that somehow inspire me during my work.

A special appreciation is dedicated to my supervisors, Laure, Lorenzo, and Patrik, who have taken me on as their graduate student and taught me to think and reason as an independent researcher. Since the very beginning of my Ph.D., you have guided me step-by-step to approach the topic, from what we had to what are missing. You taught me not only to look at the smallest detail, but also to build up meaningful stories. Three of you with so different characters have miraculously harmoniously upgraded me to an advanced version of myself. Madam Laure, it is always a pleasure to work with you. A lovely morning in the lab sometimes started by meeting you in the corridor, sharing instantly one or two pieces of my work or our near-future plans, or just chitchatting a bit non-science topic. You are the one who always showed me my blind spots in my work, and this somehow has widened my vision. Your encouragement helped me gain back my confidence every time I started doubting myself. Thank you for all your supporting resources, for being a great mother all these times. Mr. Patrik, although we didn't talk to each other frequently, partly due to the geographic distances, I'm always grateful for your support and hospitality during my visits at Chalmers. You gave great opportunities to learn how to use DFT calculations and to access to the spectroscopic platform at Chalmers. You taught me to treat all the data properly and precisely, and to build up our stories logically, which I will keep in mind for my whole scientific career to have better products in the future. And finally, Mr. Lorenzo. I still remember my first day in Building 15, meeting you in person for the first time. You were super friendly and slightly expose your sense of humor (which I have been fully

experiencing in three years). And I will never forget how I was impressed when you unveiled the secret of science during our monthly meetings, how you used a clementine to explain me the quadrupole splitting, how you visualized the PCA for a dummy me with my ruler. I truly appreciate all the opportunities you and Laure gave me, all the conferences, two wonderful beamtimes that open me a whole new world with Mössbauer, Raman, and X-ray spectroscopies. You taught me to stay calm and be positive in every bad situation. You were always patient with my procrastination and my wetness. You raised me up every time I'm drowning in my self-disappointment. Thank you for your guidance and your personal advice that help my keep in the right track of my scientific future and for sure handle much more complicated issues ahead. Last but not least, thank you for your chocolate most of the time I disturbed you in your office by the end of the days.

My whole PhD research would have never been completed without the aid of all researchers at ICGM (Montpellier) and KMF (Chalmers University). Many thanks to Bernard, Julien, Domi, and Léa for having shared with me your experiences, for your advice, and for always being so kind and supportive. What I have learnt from you will go with me throughout my career. Monsieur Moulay, it is always a great pleasure to work with you. You're not just a scientist with a great open mind, but also a great man with a warm heart. Thank you for always keep your smiles for me even when I wasted so many expensive Al foils. Discussing Mössbauer spectroscopy with you was so interesting. Our trip to Nancy surely is one of the most memorable journeys in my Ph.D. I would like to thank Fabrice, Gustav and Athmane for their contribution in our beautiful paper. Without you guys, it wouldn't have been as appealing as it is. A special thanks to Prof. Aleksandar Matic, Ezio and all the postdocs and students at KMF for your hospitality and your help during my stay at Chalmers. And also, Giuliana and Alessandro for your support and advice during our beamtimes. Ales, it is a huge honor to know such an amazing scientist like you. I hope that we will soon meet again in the future.

My life in the lab has been fulfilled with tons of memories without my beloved friends. Justine, my little adorable JuJu, thank you for always caring for me, and for always the first person realizing that I wasn't OK, no matter how far we were. Thank you for your encouragements that cheered me up in my bad days. It's a pity that I couldn't join your defense. I wish you all the best in your bright future. And Vincent, mon enseignant, PIBs were much less difficult at my beginning thanks to you. Working with you was a great honor for me. Khaled, my boss – for whom I worked as a "part-time secretary"! You were my companion in these three years, to all of the ALISTORE meeting. With you here, I have never felt alone. You

are not only a lab-mate, but like a big brother to me. You are a great researcher, and I'm so sure that no matter where you go to, you will always succeed. Armando, Marine, Coumba, Rafael, Théo, Clément, Patricia, Eunice, Lucie, Sabrine and Jérôme, thank you all of you for every single moment that we have shared together, and thank you for always cheering me up by your own ways. Thank you, Imane, for always having a smile on your face whenever we met. Last but not least, I would like to thank my master students, Clément Pons, Luka, and Dat for their contributions in my PhD work.

I would like to thank Romain, Badre, and Louiza, all the students of TROPIC project. Romain, my beamline buddy, it was a great honor to know you, such an excellent prospective scientist with a huge love for FT. My first beamtime in Trieste was full of joy thanks to you and Lorenzo. I wish you all the best in the next step of your career and hope to see you soon. Badre and Louiza, working with you was also a great honor. You have opened my mind to some aspects that I didn't notice before. I wish you all the best in your last year of PhD. A special thanks is dedicated to Long, my senior, my advisor. Our scientific discussions were so enthusiastic. Thank you very much for your advice, which help me a lot not only in my PhD research, but also in my choice of career.

I couldn't have gone this far without unlimited support from my mother. Mom, millions of words are not enough to express how grateful I am after all these years. You have dedicated your whole life to raise me to become a good person. You are always a solid support for me to spread my wings to everywhere I want to go. "Con yêu mẹ" is not enough to tell you how important you are in my heart. And thank you to my chosen brothers, Lĩnh, Hải Nam, Khoa, and Khang, and my sisters, Nhạn, Phương-Anh Hoàng, and Anh Nguyễn, no matter how far we are, regardless the time difference, you are always here when I need you. You healed me, and somehow taught me to be more mature.

The last words are dedicated to my little furry boys, Galasea and Petit Pois. Your presence lights up my life every time my internal battery runs out. Mommy loves you.

TABLE OF CONTENT

CHAPTER 1.
INTRODUCTION

1.1. General context

1.1.1. Rechargeable batteries

It is no exaggeration to say that batteries, particularly rechargeable batteries, have boosted up the modern civilization and significantly improved our lives. Batteries energize the world, from portable electronic devices (PEDs) to vehicles. In a larger scale, batteries can store unused electricity and deliver it back to the grids with the power up to decades of MWhs.[1]

The dawn of rechargeable batteries can be dated back to the middle of XIX century with the invention of lead-acid battery by Gaston Planté. Regardless the primitiveness and the historical aspect, this technology still endures nowadays due to its simple manufacture and low cost. Lead-acid batteries are mainly installed in vehicles and power stations.[1] A lead-acid battery exhibits a specific energy density of 30-50 Wh kg^{-1}, which is lower than other commercial batteries. Besides, such weaknesses as short lifetime (~500 cycles), slow charge rate, high toxicity and hazard restrain the usability of lead-acid batteries in PEDs.[2]

Being introduced in 1899, the Ni-Cd battery rapidly became the power storage of choice. It overcame the several limitations of lead-acid batteries, providing long cycle life, higher energy density (Figure 1.1), faster charge/discharge rate. Ni-Cd batteries were widely used in various scales of application until being defeated by nickel-metal hydride (Ni-MH) and Li-ion batteries in 1990s and being prohibited for private usage in 2006 due to the environmental crisis caused by toxic cadmium.[3]

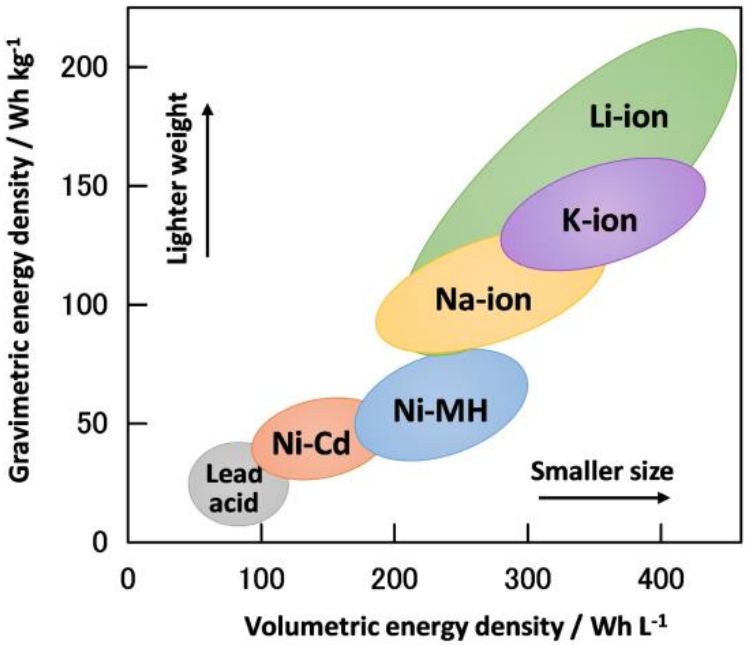

Figure 1.1. Gravimetric and volumetric energy density of rechargeable batteries [4].

Ni-MH battery was first commercialized in 1989, offering outstanding performance compared to the former generations. Therefore, Ni-MH batteries have been widely used not only in PEDs but also in hybrid electric cars in the beginning of 1990s. However, this technology quickly lost its popularity to Li-ion batteries.

1.1.2. Lithium-ion batteries

Lithium-ion batteries (LIBs) first commercialized by SONY in 1991 exhibit remarkable properties with two times energy density to Ni-MH batteries (Figure 1.1) and the lifetime up to 2000 cycles with lower costs [2,5]. LIBs have been soon dominating the market of energy storages for a wide range of applications, e.g., handheld electronics, electric vehicles (EVs), and power plants [1,2,6]. The introduction and development of LIBs encourage an efficient utilization of renewable energy sources (wind, solar, tide, etc.) and accelerate the transport electrification with millions of electric cars on sale over the last five years [7–9].

The research on LIBs began in the 1970s and reached their golden era in the 1980s with three famous pioneers John Goodenough, Stanley Whittingham and Akira Yoshino, whose contributions were acknowledged by their Nobel Prize in 2019. In the primary configuration demonstrated by S. Whittingham, Li metal and TiS_2 as negative and positive electrodes, respectively.[10] When the cell works, Li^+ ions act as the charge carrier, being transfer from one side to the other. However, limited cell voltage (< 2.5 V) and safety issues coming from the dendrite growth on Li electrode prevented this cell from going into market.[11] Li metal was then replaced with petroleum coke (proposed by A. Yoshino)[12] and then graphite[13], which were able to deliver high capacity and maintain the same working voltage and to get rid of the instability of lithium metal. On the positive side, the discovery of layered oxides by J. Goodenough in 1980s was a breakthrough in the development of LIBs. Layered oxides, e.g., $LiCoO_2$, increase the operating voltage up to *ca.* 4 V,[14] and hence, somehow provide higher energy density. On the other hand, a layer oxide itself is a lithium source for the battery, hence, it can be coupled with a lithium-free electrode, such as hard carbon [15] (SONY cells, 1991) or graphite in present-day batteries.

Over three decades, tremendous improvement on performance, cycle life and production cost created a golden era for LIBs. The discovery and development of new materials, e.g., layered compounds ($LiNi_xMn_yCo_zO_2$) and spinel ($LiMn_2O_4$ and its derivatives) increase the cell voltage, and hence, the energy density comparing with the first in-sale batteries (from 80 Wh kg^{-1} to *ca.* 220 Wh kg^{-1}).[16] On the other hand, LIBs composed of olivine-type $LiFePO_4$ (cathode) and $Li_4Ti_5O_{12}$ (anode) exhibit superb cyclability (~ 20,000 cycles) at high current

rates.[17] This configuration reduces the heat release and eliminates overheating issues, which help building up high-power storages. [18–20]

1.1.3. Electrochemical principles of LIBs

A typical LIB is composed of a positive electrode (or the cathode, as the reduction occurs on this site during the discharge) and a negative electrode (commonly called the anode, which is oxidized during the discharge), a Li-containing electrolyte and a separator which allows Li^+ transport and prevents the contact between two electrodes (Figure 1.2). The basic chemistry of batteries is based on intercalation or insertion concepts. The electrodes consist in stacked layers, tunnels or frameworks facilitating the Li^+ migration. An insertion/extraction of Li^+ correlates with a reduction/oxidation of the active elements of host material. For instance, when a $LiCoO_2$ | graphite cell (Figure 1.2) is charged, the following reactions take place:

Positive: $$LiCoO_2 \rightleftharpoons xLi^+ + xe^- + Li_{1-x}CoO_2 \qquad (0 < x \leq 1)$$

Negative: $$xLi^+ + xe^- + 6C \rightleftharpoons Li_xC_6 \qquad (0 < x \leq 1)$$

When the cell works (discharge process), the reactions inverse.

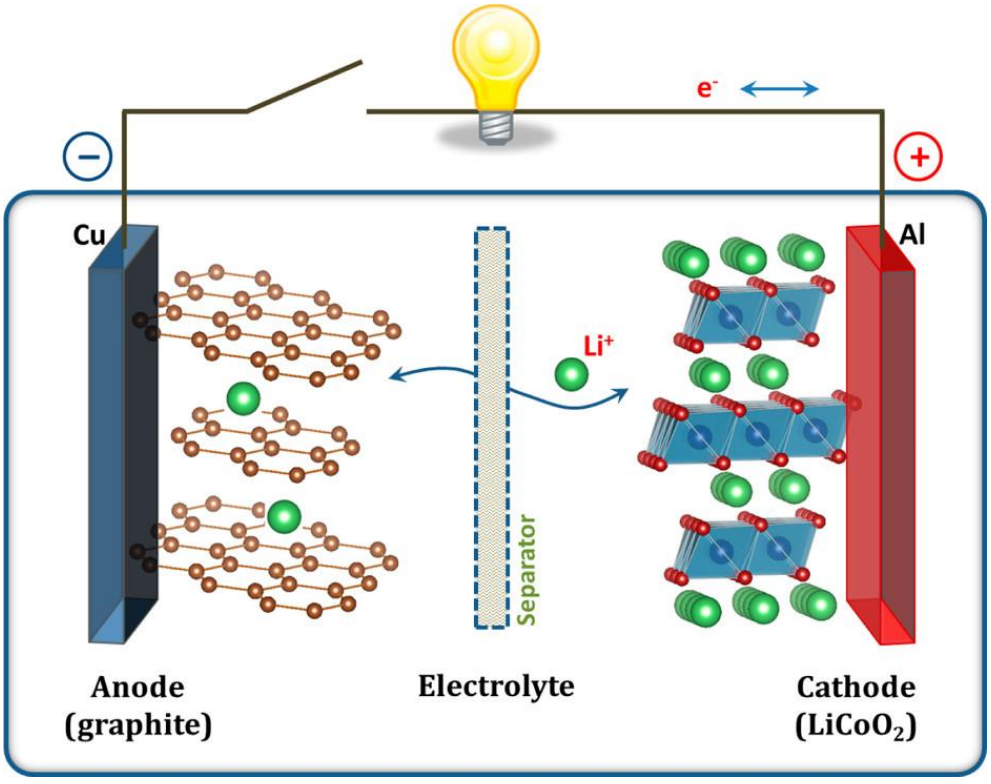

Figure 1.2. Diagram of a LIB using graphite and $LiCoO_2$ as electrode materials.[5]

The number of exchanged Li^+ ion (x) determines the capacity of the materials as well as the cell. Besides, several concepts referring to evaluation of battery performance are introduced below.

a) Voltage

The voltage of a battery is calculated by the potential difference between two electrodes by the following formula:

$$E = E_{cathode} - E_{anode}$$

In a half-cell, where the anode is an alkaline metal (Li, Na, or K), this is the potential of the active material *versus* the metal.

The working voltage range of an electrode material is determined by the potentials of its redox couples, which can be evaluated from Nernst equation:

$$E = E_0 + \frac{RT}{nF} ln \frac{a_{Ox}}{a_{Red}}$$

b) Current density and current rate

Galvanostatic cycling is one of the most popular electrochemical techniques used to evaluate the performance of a battery, in which a constant current is applied in a defined voltage range. The current can be measured by the density (mA g^{-1}) or rate (C/*n*). The latter corresponds to the achievement of full capacity which is equivalent to one mole of alkali ions exchanged in *n* hours.

c) Capacity

The capacity **C** (mAh) corresponds to the amount of charge that can be stored in a battery and can be determined by the integral of the current as a function of the time:

$$C = \int_0^t I(t)dt = nzF$$

in which, *z* is the charge of the electroactive ion (e.g., *z* = 1 for alkali ions), *n* is the number of ions exchanged (mol), and F is the Faraday constant (96500 C mol^{-1})

To evaluate the charge storability of a material, the specific capacity $\mathbf{Q_m}$ (mAh g^{-1}) is commonly used. This value is the capacity per unit of mass of the material. It can be calculated from the following equation:

$$Q_m = \frac{1000 \cdot F \cdot n}{M \cdot 3600}$$

where M is the molar mass (g mol^{-1}) of the electrode material.

d) Energy density

One of the key factors to evaluate the quality of a battery is its energy, which depends on the voltage (E) and discharge capacity (C):

$$energy = E \cdot C$$

In practice, the energy density, gravimetric (Wh kg^{-1} or Wh g^{-1}) or volumetric (Wh L^{-1}), is more favorable. For instance, the gravimetric energy density is the product between voltage and specific capacity. However, in most cases, the voltage is not constant during the electrochemical processes, thus, the energy density is calculated by the following equation:

$$energy\ density = \int_0^{Q_m} V(Q)dQ$$

e) Coulombic efficiency

The Coulombic efficiency (CE) is the ratio of the capacities obtained/extracted in the charge and discharge processes of a full cycle. The CE of a negative electrode is defined as:

$$E\ (\%) = \frac{C_{charge}}{C_{discharge}} \cdot 100$$

For a positive electrode, the formula of CE is inversed.

1.2. Potassium-ion batteries: Promises and challenges

LIBs have been playing a prominent role in the quest of a carbon-neutral society. However, dramatic increase in energy demand together with the necessity of a compromise between the low cost and high energy density may somehow limit the application of LIBs in the future. On the other hand, this is an opportunity to develop new storage technologies known as next-generation batteries (or post lithium-ion batteries) to diversify the storage market and to find alternatives for LIBs in electric vehicles. Based on the same concept "rocking-chair" as LIBs,[21] sodium-ion batteries (SIBs), potassium-ion batteries (PIBs) and multivalent-ion batteries (e.g., Mg^{2+}, Ca^{2+}, Al^{3+}, Zn^{2+}) have been investigated widely since 2005.[22–26] Nowadays, SIBs have achieved a considerable success to be the first post-lithium technology going into mass production[27], nevertheless, the quest to a sustainable society with a wide range of battery choices is still open for alternative technologies. Among them, PIB is considered as the most promising option because of several notable advantages.

First, PIBs can be a compensation of low cost and high energy density. In PIBs, Cu foil – the common anode current collector in LIBs – can be replaced by cheaper aluminum, as K does not alloy with Al at low potential. The ability to use Mn, Fe or V instead of costly Ni and Co in the best performing cathode materials in PIBs is expected to reduce the price of the practical K-ion cells.[8] Besides, K resources are equally distributed all over the world with high abundance (2.09 wt %), while Li content is limited both quantitatively (0.0017 wt %) and

geographically (mainly found in South America),[28] which to some extent makes the price of K_2CO_3 sensibly lower than that of Li_2CO_3 (1000 \$ ton^{-1} and 8750 \$ ton^{-1}, respectively).[29]

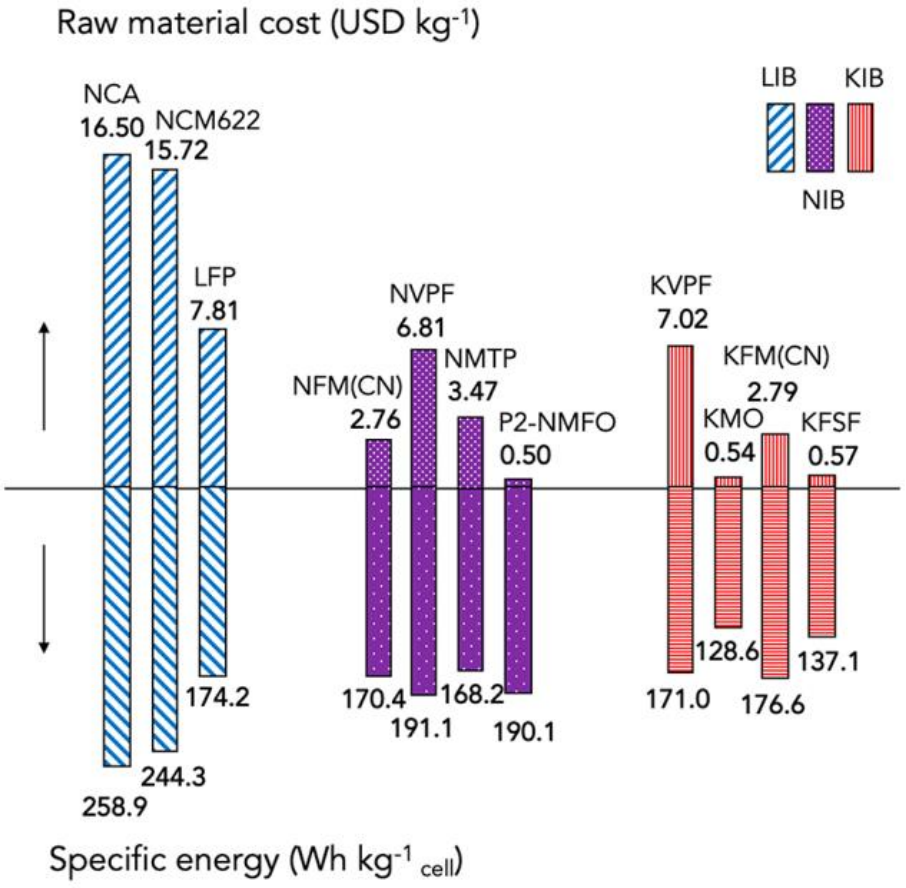

Figure 1.3. Cost (direction up) and specific energy (direction down) of selected cathode materials used in LIBs, SIBs, and PIBs.[8]

With respect to the electrochemistry, PIBs can offer higher cell voltage than those of LIBs and SIBs. Experimental and computational chemistry have proven that the standard potential of K^+/K in ester-based electrolyte is lower than that of Li^+/Li (Table 1.1).[30,31] This allows the anode in PIBs to work at lower potential without suffering from potassium plating on the electrode surface. Furthermore, the ionic radius of K^+ is larger than those of Li^+ and Na^+ (Figure 1.4), hence, K^+ possesses the smallest Stoke radius, leading to the weakest ion-solvent interactions among the three alkalis. This feature is a privilege of K-based electrolytes, as they offer faster ionic diffusion and higher ionic conductivity.[4] Last but not least, the K^+ can reversibly intercalate into graphite – the commercial anode of LIBs, thus, this technology could be transferred to PIBs. This is an advantage over SIBs, since Na^+ cannot migrate into graphite under the same conditions due to the thermodynamically unfavored issue, [32,33] leading to the employment of hard carbon anode with much lower initial CE in SIBs[34]. The possibility of

using graphite anode is another advantage for PIBs to compete with its counterparts in the battery market in the future.

Table 1.1. Physico-chemical characteristics of Li, Na, and K.

	Li	Na	K
Relative atomic mass (g mol^{-1})	6.9	23.0	39.1
Ionic radius (Å)	0.76	1.02	1.38
E^0 ($A^+_{(aq)}$/A) vs. SHE (V)	-3.04	-2.71	-2.93
E^0 ($A^+_{(PC)}$/A) (V)[30]	0	0.23	-0.09
E^0 ($A^+_{(EC/DEC)}$/A) (V)[31]	0	0.3	-0.15

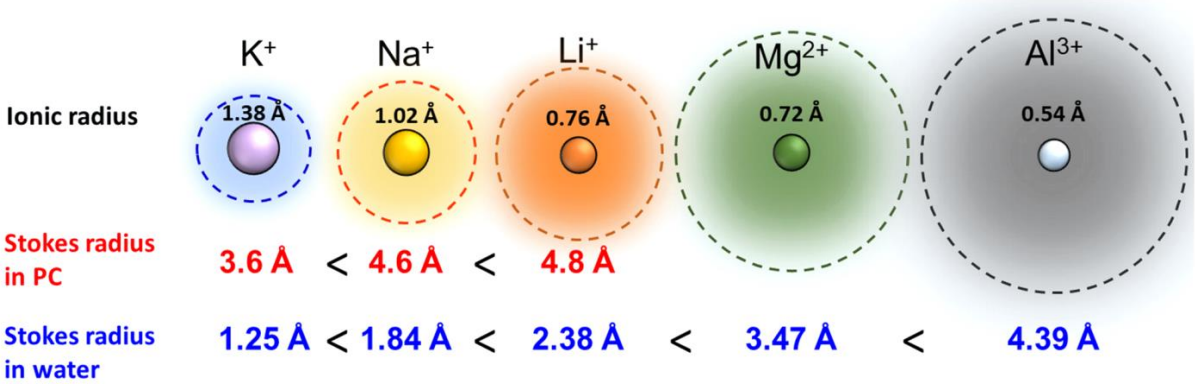

Figure 1.4. Ionic radii and Stoke radii in propylene carbonate (PC) and in water of K^+ in comparison with other cations.[35]

1.3. Negative-electrode materials

1.3.1. Graphite

a) Status

With the ability to accommodate K^+ ions, graphite has become the center of attention among carbonaceous negative electrodes for PIBs. In PIBs using conventional carbonate electrolytes, graphite exhibits a relatively high capacity of *ca.* 279 mAh g^{-1}, but the cycling retention strongly depends on the electrolyte.[36]

Graphite consists of graphene layers that are stacked in ABAB (hexagon) or ABCABC (rhombohedron) sequences. An insertion of a guest cation M^+ (M = Li, K) leads to the re-ordering of the slabs from either of those stacks to AMA-type structure. This characteristic transformation – known as staging process – can be easily followed by X-ray diffraction (XRD), yet the structural evolution sequence is still a matter of debate. *Ex situ* XRD described the electrochemical potassiation of graphite in three consecutive stages (Figure 1): $KC_{36} \rightarrow KC_{24}$

→ KC_8.[37] By *operando* XRD, however, Fan and co-workers suggested a four-stages mechanism: KC_{48} → KC_{36} → KC_{24} → KC_8.[36] On the other hand, Luo *et al.*[38] compared computed potential profiles of several staging routes with the experimental electrochemistry, and proposed that KC_{24}, KC_{16} and KC_8 correspond to stage III to stage I, respectively.

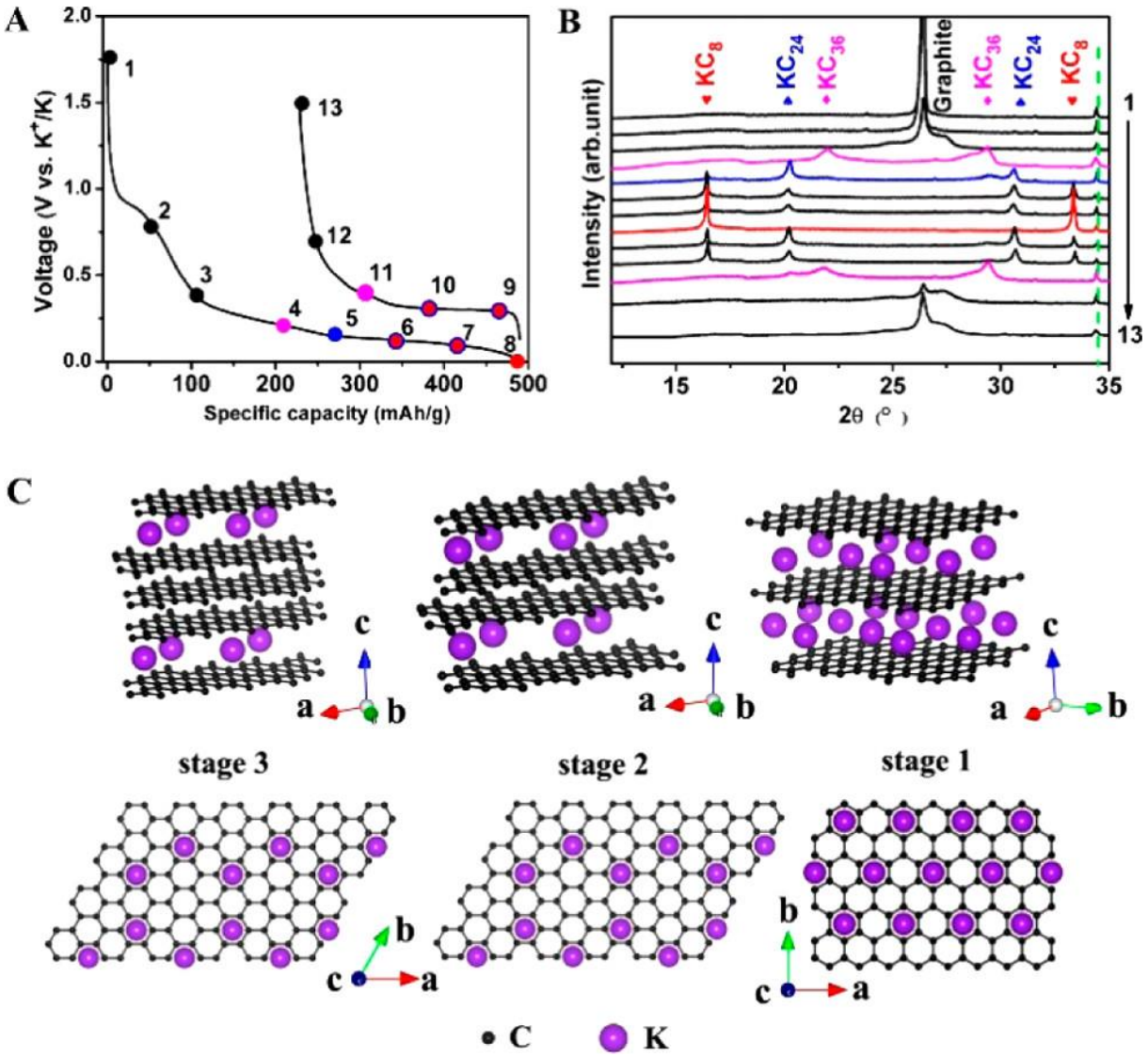

Figure 1.5. (A) Galvanostatic profile of graphite | K cell in the first cycle; (B) ex situ XRD patterns at selected states of charge; and (C) Structure diagrams of 3 main stages: KC_{36} (stage III), KC_{24} (stage II) and KC_8 (stage I), side view (top) and top view (bottom).[37]

An interesting phenomenon of graphite is the co-intercalation of K^+ and solvent molecules when using low-concentration glyme-based electrolytes. The co-intercalation occurs at higher potential (*ca.* 1.0 V vs. K^+/K) than the pure intercalation (*ca.* 0.2 V vs. K^+/K) and undergoes a larger volume expansion due to the size of the intercalated species. Despite this volumetric hindrance, the electrochemical performance of graphite in 1 M KPF_6/diglyme was stable up to 1000 cycles with the initial capacity of 100 mAh g^{-1} at 2 A g^{-1}.[39] More interesting,

highly increasing salt concentration alters the mechanism from co-intercalation to K^+ intercalation.[40] For a long time, this alternation was associated with the stability of the solid-electrolyte interphase (SEI) and its ability to block the solvent molecules,[41–44] yet no evidence was found to confirm its influence on the mechanism. On the other hand, the solvation characteristics of the electrolytes were suggested to determine the storage properties of graphite in the similar Na^+/DME system[45] or the well-known $LiPF_6$/PC case[46].

b) Current and future challenges

The major quest for graphite is to improve the cycle life and reduce the irreversible capacity caused by continuous electrolyte decomposition leading to SEI formation and lower coulombic efficiency, and at the same time provide high capacity. Each component of the battery, such as electrolyte (salt and solvents), counter electrode, binder, carbon additives, even the nature of graphite itself, can affect the electrochemical performance of graphite electrodes. Comparing the two storage mechanisms of graphite, bare intercalation is indeed superior in terms of capacity and energy density. Therefore, electrolytes that can boost K^+ intercalation are preferred. Either conventional carbonate-based or high-concentration glyme-based electrolytes promote this condition. However, the choice of the potassium salt is essential for the stability of the SEI, which is one of the key factors influencing the cycling performance. KPF_6 and KFSI are the most common salts used for half cells; while KPF_6 is safe for the current collectors but has low solubility in all solvents and leads to an unstable SEI, and thus short cycle life, KFSI can form an inorganic rich SEI and provides excellent electrochemistry, but strongly corrodes Al current collectors. For these reasons, appropriate salt or of salt mixtures should be considered to meet the cell life requirements.

Given its high chemical reactivity, K metal is not a good counter/reference electrode to couple with graphite in half-cell experiments. Most electrolytes do react with K metal, inducing the formation of shuttling species that can migrate to the working electrode and further react at its surface, modifying its electrochemical behavior.[47] In addition, the potential of K metal is unstable, which makes the precise measurement of the electrode potential difficult. It is thus preferable to evaluate graphite's performance in full cells, or three-electrode systems with suitable references.

Binders also play an important role in electrochemical performance of graphite, strongly influencing both physicochemical and mechanical properties of the electrodes. According to Wu *et al.*, CMCNa (carboxymethylcellulose sodium) and PANa (polyacrylate sodium) are more efficient than PVdF (poly(vinylidene fluoride)).[48] Graphite | K cells using CMCNa or PANa as

the binder show higher initial Coulombic efficiency (ICE) than when using PVdF. Additionally, PANa acts as an artificial SEI which prevents cracks on electrode surface, and hence, allows a long and stable cycle life.

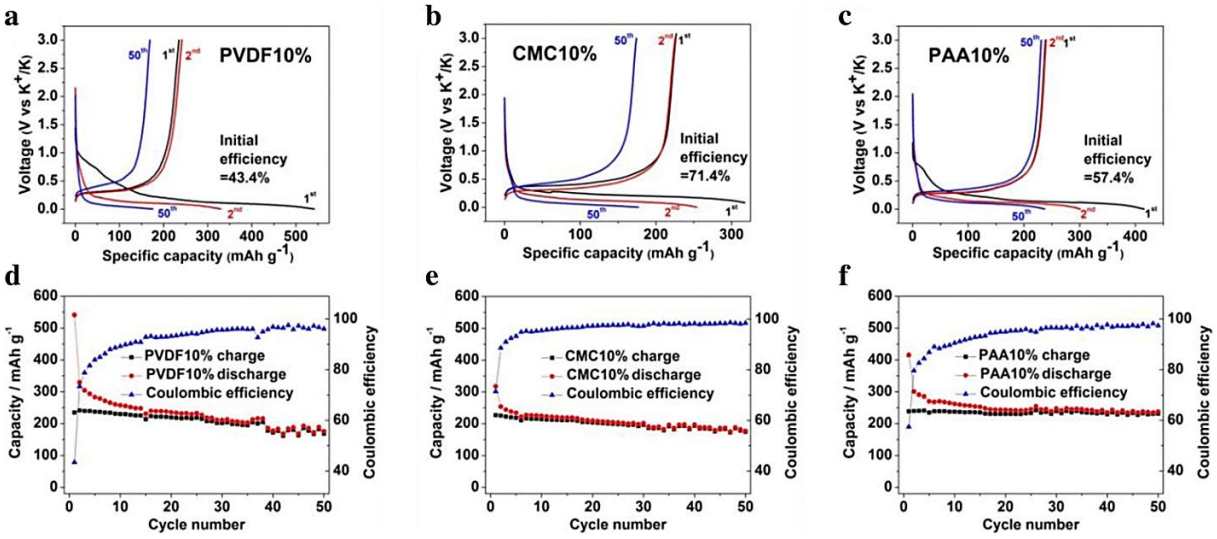

Figure 1.6. (a,b,c) The galvanostatic profiles and (d,e,f) the cyclability of graphite using PVdF, CMC, or PAA as binder.[48]

The nature and the morphology of graphite is also challenging for battery scientists. The insertion/extraction of K^+ ions engender an interlayer breathing of 60 % (from 3.36 Å to 5.35 Å). This drastic volume expansion/shrinkage can break the SEI layer formed in the first discharge, leading to continuous electrolyte decomposition to recompose the SEI in the following cycles – a possible reason for battery failure. Besides, crystallinity, shape and size of graphite particles deserve more consideration. Tuning one of these properties may improve the performance of graphite in both half cells and full cells. Despite their importance, up to now, there is no statistical study on their impact on graphite in PIBs.

c) Scientific advances and promises

Several strategies have been worked out recently to improve both ICE and cyclability of graphite. One major approach is altering electrolyte components without any severe modification on the electrode. As mentioned, carbonate-based electrolytes always promote K-intercalation. Binary-salt KPF_6/KFSI in EC-DEC at the appropriate molar ratios (10 or 25 % of KFSI) enhanced the ICE and cycling retention of graphite comparing with those when using single salt electrolytes [40]. On the other hand, replacing carbonate ester with ether solvents was an effective practice to extend graphite's cycle life. Highly concentrated KFSI in DME (1,2-dimethoxyethane) provided K^+ intercalation with a specific capacity close to the theoretical value up to 50 cycles.[40]

The large volume expansion of graphite is another issue that needs to be tackled. Expanded graphite with larger interlayer distance (3.87 Å) exhibits superior cyclability and stable capacity over 200 mAh g^{-1} at 50 mA g^{-1} up to 200 cycles.[49] Etching graphite with KOH at high temperature can slightly enlarge the space between graphene layers, which increases the initial discharge capacity of graphite up to 350 mAh g^{-1} at the current rate of 50 mA g^{-1}.[50] This mechanical expansion increases K^+ diffusion up to seven times, which indeed improves the electrochemistry of graphite.

As discussed above, a stable SEI is essential for long-lifetime batteries. However, electrochemical SEI is not uniform due to the continuous decomposition/reformation when the battery is working. A thin homogeneous layer of artificial SEI formed by the deposition of the products of the chemical reaction between KFSI/DME and K metal reduces the irreversible capacity and enhances the lifetime of graphite | K cells up to 1000 cycles with an ICE of 93 % and capacity retention approaching 100 %.[51] This artificial SEI, mainly consisting of inorganic compounds, sufficiently prevents the electrolyte from further decomposition, hence, excellent cyclability could be obtained.

Many studies have confirmed that graphite is a promising anode material for PIBs. With an appropriate electrolyte, graphite can provide high capacity via K^+ intercalation mechanism. Despite the big efforts made, the cyclability of graphite in PIBs is still far from being comparable with that in Li-ion systems. Nonetheless, the current attempts to improve the electrochemical performance have provided interesting hints, thus encourage new studies to further optimize electrolyte and electrode formulation. Moreover, computational chemistry, modelling and machine learning will be good accompanies for hands-on practices on the way bringing graphite-PIB to industry.

1.3.2. Non-graphitic carbons

With the expectation to avoid the large volume expansion occurring in graphite, non-graphitic carbons were also investigated in PIBs. These materials can be synthesized by the pyrolysis of carbohydrates or agricultural wastes. Depending on the synthetic conditions (precursors, atmosphere, temperature, etc.), the product could be hard carbon, soft carbon, or porous carbon with different proportion of disordered domains and surface area.

a) Hard carbon

As mentioned previously, hard carbon was used as anode for the first commercialized LIBs, but then defeated by graphite which provides higher CE. However, recently, hard carbon has reclaimed its crown in SIBs since graphite is unable to lodge Na^+. Hard carbons are

produced by pyrolyzing oxygen-rich compounds, e.g., carbohydrates, at high temperatures (≥ 1000 °C) under Ar atmosphere.[52–55] Hard carbons consist of arbitrarily oriented graphitic domains with higher interplanar spacing than graphite, and those regions are connected by micropores of different sizes (Figure 1.7a). This structure allows the alkali insertion via two mechanisms: intercalation into the layers and adsorption in the pores.[34] Until today, a general model of the structure of hard carbons could not be sketched, since any changes in the carbon sources, pre-treatment, or carbonization conditions can vary the degree of disorder, pore sizes, interlayer distance, and/or other properties. Generally, hard carbons produced from appropriate carbonization can deliver a reversible capacity of 260-300 mAh g^{-1} (Figure 1.7b)[52,56], but the irreversible capacity is higher (> 20 %) than that of graphite. Observing a decrease in the interplanar space after one potassiation/depotassiation cycle, Wang *et al.*[57] proposed an explanation for the high capacity loss, whereby the K^+ intercalation irreversibly graphitizes the carbon layers in short-range, hence in the depotassition, K^+ cannot exit the graphitic stacking completely. In contrast, Katorova and co-workers[58] believed that the closed cages formed by curled graphitic layers trap K^+ ions, leading to high capacity loss in the first cycle. Indeed, more efforts should be made to have an insightful understanding on the electrochemical mechanism of hard carbon and to design a suitable synthesis that can improve its ICE. Nevertheless, hard carbon is still a good choice as anode for PIBs.

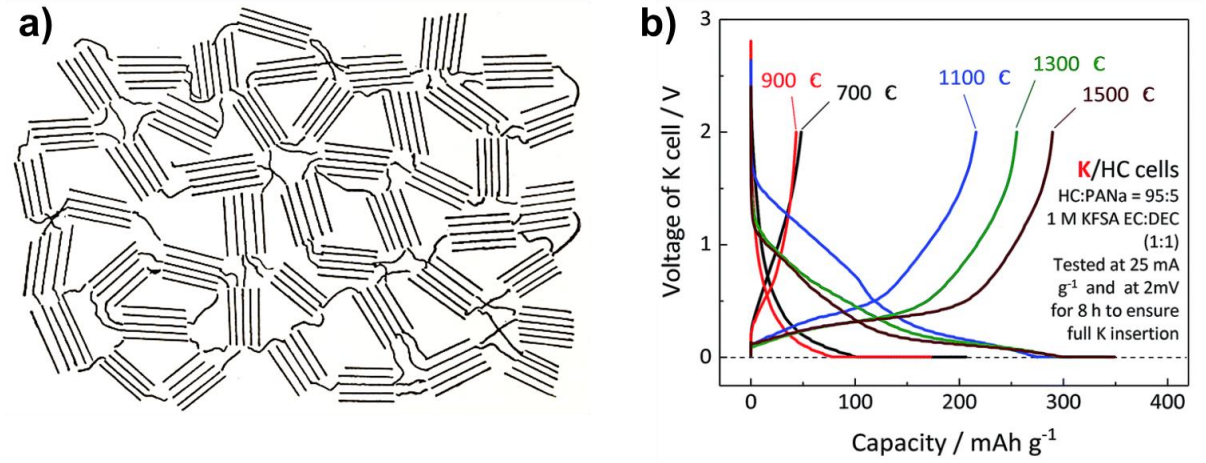

Figure 1.7. (a) Schematic illustration of hard carbon [59] and (b) the galvanostatic profiles vs. K^+/K of hard carbons prepared at different post-treatmet temperature[56].

b) Soft carbon

Different from hard carbon, soft carbon materials are synthesized via the carbonization of organic aromatic compounds and polymers.[60,61] Soft carbon possesses lower crystallinity than hard carbon or graphite, and plenty of defects, resulting in high degree of disorder ($I_D/I_G > 1$)[61,62] Soft carbon exhibits sloped galvanostatic profiles with long cycle life and high

long-term CE (up to 99.5 %). However, ICE issue is more severe for soft carbon (ICE < 60 %)[61,62] comparing with hard carbon, which makes this material less attractive than its counterparts.

c) Porous carbon

Porous carbon materials are mainly derived from biomass; therefore, they could be doped by other elements (e.g., S, N, or O) and possess various morphologies. Generally, porous carbon are rich of defects and thus, exhibits large surface area,[63] and to some extent maintains the structural stability during the K^+ migration. In K-ion half-cells, porous carbon can offer a stable long-term performance with a specific capacity of *ca.* 300 mAh g^{-1}.[63] Similar to other non-graphitic carbons, porous carbon suffer from poor ICE due to the large surface area. Therefore, further synthesis optimization is essential to make porous carbon, as well as other non-graphitic carbon applicable.

1.3.3. Non-carbonaceous materials

a) Alloy materials

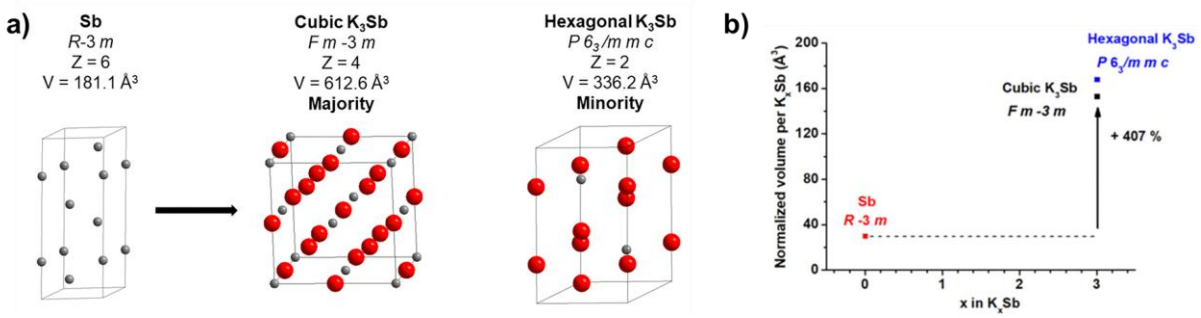

Figure 1.8. Structural transformation (a) and normalization of volume changes (b) of Sb during the potassation.[64]

Based on alloying reactions with alkali ions, p-group elements such as tin (Sn), antimony (Sb), bismuth (Bi) and phosphorus (P) and their binary alloys were extensively investigated in various systems, from lithium-ion to post-lithium batteries. These materials are famous for their excellent specific and volumetric capacities. For instance, Sn offers a specific capacity of 226 mAh g^{-1} corresponding to the formation of KSn as the fully potassiated phase,[65] while Sb/C nanocomposite can lodge up to 3 K^+ (equivalent to 660 mAh g^{-1})[66]. Interestingly, their binary alloy SnSb prepared by high-energy ball milling exhibits a sustainable long-term performance, with a specific capacity of 282 mAh g^{-1} after 40 cycles.[67] However, these metalloids and alloys suffer from drastic volume expansion (up to 400 %)[64] and extended electrochemically-driven pulverization, often resulting in poor cyclability.[68,69] High irreversible capacity is another critical problem which is mainly caused by the parasitic reactions between K metal and the

electrolyte.[47] As the aforementioned issues are unavoidable, so far the realization of a practical K-ion cell using these materials is still a challenge.

b) Potassium titanates

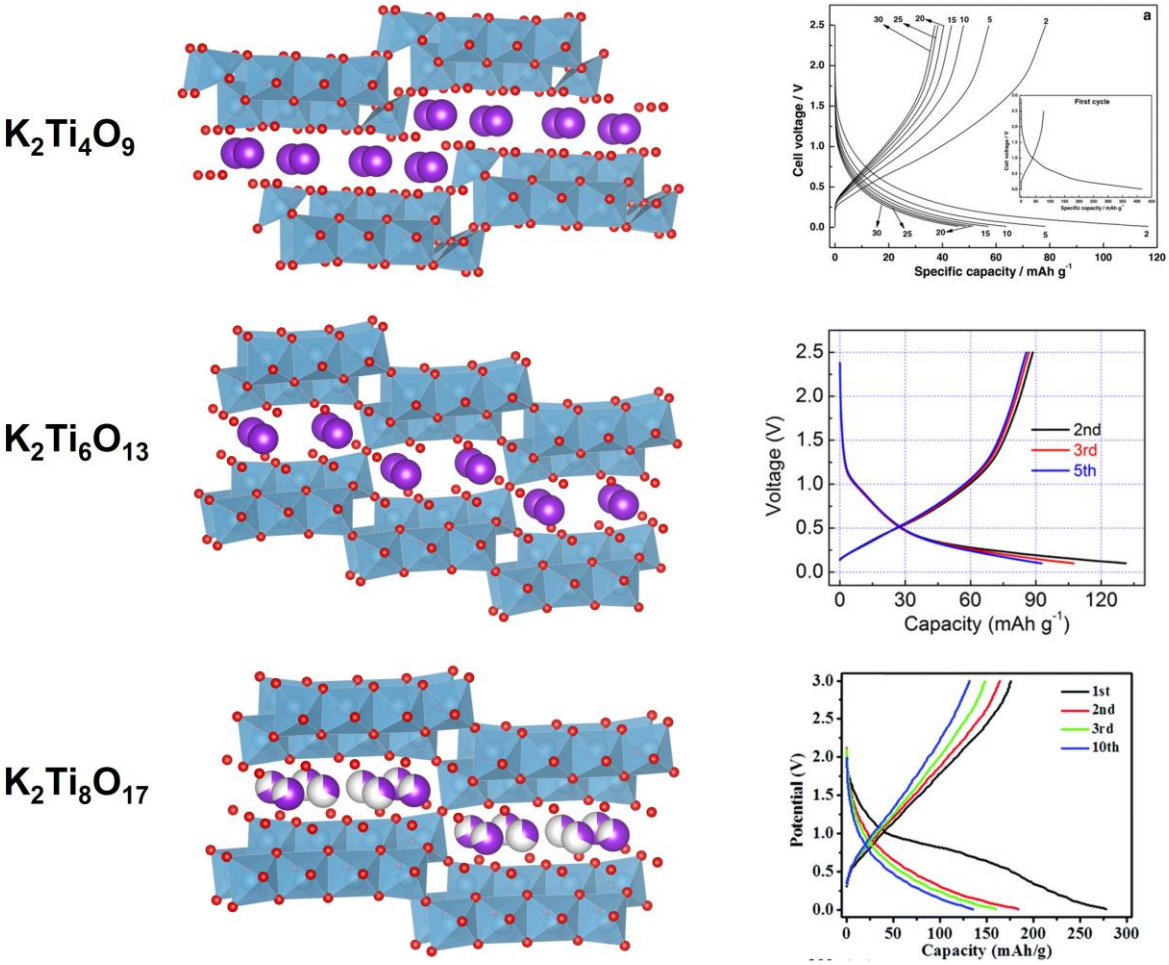

Figure 1.9. Crystal structures (left) and galvanostatic profiles (right) of three KTO materials: $K_2Ti_4O_9$ (top)[70], $K_2Ti_6O_{13}$ (middle)[71], and $K_2Ti_8O_{17}$ (bottom)[72].

Titanium oxides or titanates are famous anode materials following insertion mechanism with the redox reaction of Ti^{4+}/Ti^{3+} couple. One famous member of this class is $Li_4Ti_5O_{12}$ having gained a huge success in LIBs. Based on the same mechanistic concept, several potassium titanates (KTOs) have been investigated in PIBs recently.[70–72] They crystallize in *C/2m* space group (SG), with 2D channels allowing K^+ transportation (Figure 1.9). Despite the size of the inserted ions, KTO do not encounter large volume increase like most of other anode materials, and the potassiated structure (*i.e.*, $K_4Ti_4O_9$) is maintained almost unchanged.[71] Depending on the chemical formula, the specific capacity of KTO is relatively low (*ca.* 100 mAh g^{-1}), additionally, low ICE (< 50 %) and poor cyclability limit the practical application of these materials.

1.4. Cathode materials

1.4.1. Prussian blue analogues

a) Structure, compositions, and electrochemistry

Prussian blue (PB), discovered unintentionally in the beginning of 18th century,[73] were first used as a pigment in painting in 19th century owing to its unique deep blue color. For years, PB and its analogues (PBAs) have been to be versatile materials in various application, such as in pharmaceutics, analytical chemistry,[73] and recently as cathode materials for SIBs[74–76], and PIBs[77–79].

The chemical formula of PBAs can be generally represented as $A_xM1[M2(CN)_6]_y \cdot zH_2O$ ($0 \leq x \leq 2$, $y \leq 1$), in which A is commonly an alkali (Li, Na, K, etc.), M1 and M2 are 3d metals. H_2O can occupy interstitial positions (such as A sites) or coordinate to M1 in defect sites (Figure 1.10).[80] The local structure and electrochemical properties of the TMs are determined by two important features: oxidation state and spin state of the two metals M1 and M2. The former can be related to the content of A^+ ions in PBAs, and the latter is decided by the strength of the ligands. Low-spin (LS) M2 and high-spin (HS) M1 respectively locate in octahedra of six -C (strong-field ligand) and -N (weak-field ligand).[81] The octahedra are bridged by -C≡N- groups, creating a cubic-like framework with large cages where the A cations are usually located (Figure 1.10). Such large cages do facilitate the accommodation of cations of different sizes and charges.[82,83] Depending on the size and content of the guest ions as well as on the oxidation state (and thus electronic configuration and spin state) of the M1 and M2 ions, the crystalline structure of PBAs can be cubic (SG: *Fm-3m*) or distorted.[84–86] At low content of the exchangeable A cations ($x \leq 1$), PBAs can have conventional cubic lattice, while A-rich PBAs (A = Na, K, $1.5 \leq x \leq 2$) mostly crystallize in monoclinic ($P2_1/n$) structure or rhombohedral ($R\bar{3}$) for Na-based PBAs under special conditions.[84,86,87] Therefore, a monoclinic (or rhombohedral) → cubic phase transition together with a variation in lattice size are often observed when electrochemically extracting A^+ ions. Interestingly, while Na^+ removal from Na-based PBAs leads to a decrease in lattice size, volume expansion happens during K^+ extraction.[88] This surprising difference has not be totally understood up to now: apparently it is not supposed to come from the size influence, but has been rather attributed to a probably different ionic selectivity between K^+ and Na^+,[89–92] which to some extent makes PBAs the materials of choice for PIBs.

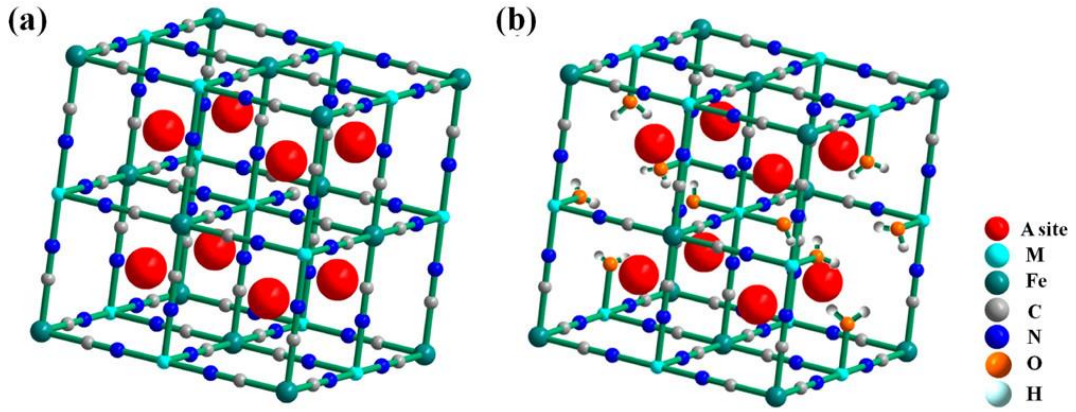

Figure 1.10. A typical structure of PBA without (a) and with (b) defects.[80]

In non-aqueous PIBs, a fully potassiated PBA ($K_2M1[(M2(CN)_6]_y \cdot zH_2O$) can offer a theoretical capacity of *ca*. 155 mAh g^{-1}, equivalent to the insertion/extraction of 2 K^+ ions, yet in reality their specific capacities can reach up to 120–140 mAh g^{-1} as some K^+ cannot be removed from the host. The redox reactions of PBAs depend on the chemical composition (Figure 1.11).[93] For example, the electrochemical reactions of $K_2Fe[(Fe(CN)_6]$ can be described in the following equations:

$$K_2Fe^{II}[Fe^{II}(CN)_6] \rightarrow KFe^{III}[Fe^{II}(CN)_6] + K^+ + e^- \quad (\sim 3.4 \text{ V vs. } K^+/K)$$

$$KFe^{III}[Fe^{II}(CN)_6] \rightarrow Fe^{III}[Fe^{III}(CN)_6] + K^+ + e^- \quad (\sim 4.1 \text{ V vs. } K^+/K)$$

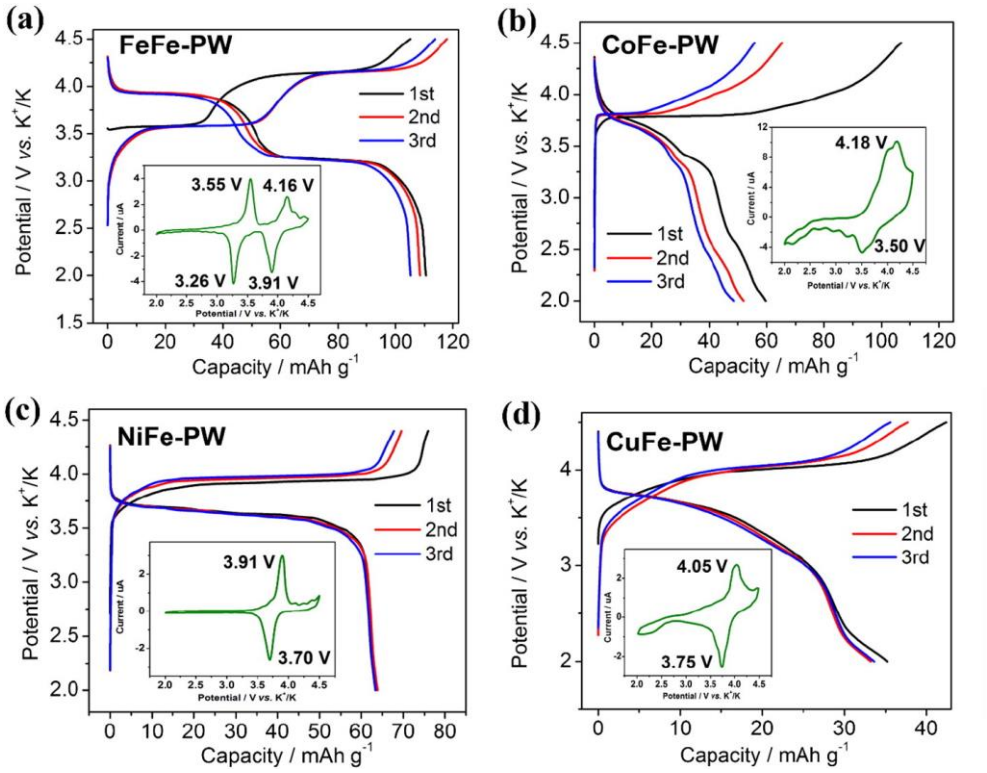

Figure 1.11. Galvanostatic profiles and cyclic voltammetric curves (insets) of different PBAs at the current density of 20 mA/g.[93]

Among the PBAs studied in the literature, $K_xMn[Fe(CN)_6]$ (MnFe-PBA) is the most attractive analog owing to its superb performance. Both HS $Mn^{2+/3+}$ and LS $Fe^{2+/3+}$ redox couples are electrochemically active at high potentials (*ca.* 4 V vs. K^+/K), and the material can offer a reversible capacity of 135 mAh g^{-1}, sustaining up to 100 cycles.[94–97] During the migration of K^+ ions, MnFePBA undergoes several phase transitions: monoclinic ↔ cubic ↔ tetragonal (Figure 1.12).[95] The second transition was explained by Jahn-Teller effect on Mn^{3+} causing the increase in *c* axis (Figure 1.12b).

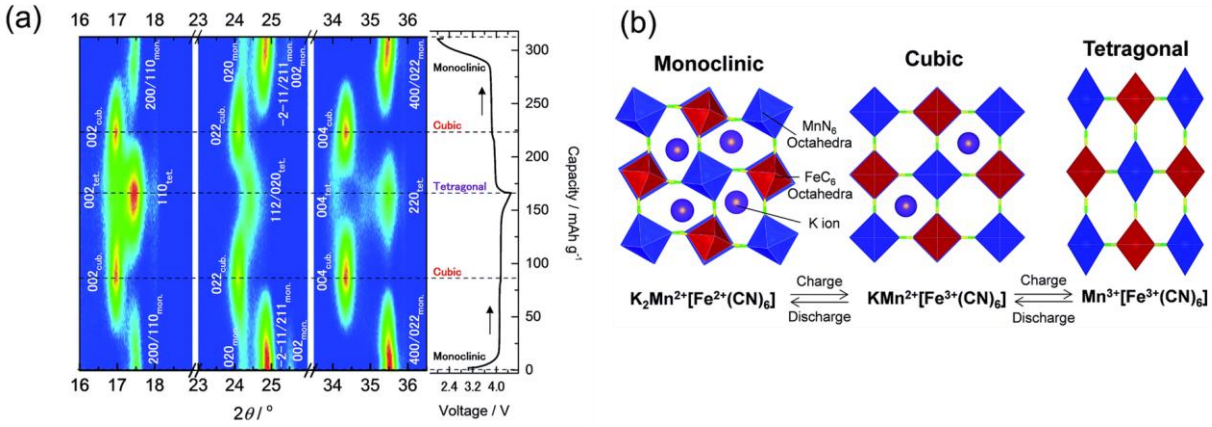

Figure 1.12. (a) Operando XRD of $K_2Mn[Fe(CN)_6]$ recorded during the first galvanostatic cycle and (b) phase transitions observed in the operando XRD.[95]

Another promising PBA is $K_xFe[Fe(CN)_6]$ (FeFe-PBA) with a specific capacity of *ca.* 120 mAh g^{-1}.[93,95] Despite its lower capacity and operating potential comparing with MnFe-PBA, a Fe replacement for Mn can avoid large volume changes due to the Jahn-Teller effect. This inspired a study on partial Fe-doped MnFe-PBA with water-in-salt electrolytes, in which $K_xMn_{2/3}Fe_{1/3}[Fe(CN)_6]$ was found to show the best cyclability.[98]

b) Challenges and opportunities

Although PBAs, especially MnFe-PBA and FeFe-PBA, have demonstrated stable long cycling life, yet not exceeding 100 cycles, several factors, such as particles sizes, hydration degree, and vacancies, should be considered to improve the cycling performance. These parameters can be controlled during the synthesis. Simple precipitation was usually preferred to prepare PBAs as this method can produce nano cubic particles (< 50 nm) and suppress the water content and $Fe(CN)_6$ vacancies which could facilitate the K^+ storage.[99,100] Furthermore, the presence of a chelating agent, for instance ethylenediaminetetraacetate salt (EDTA), can control the rate of nucleation, hence, significantly reduce the defects and amount of water and enhance the capacity (up to 150 mAh g^{-1}) and cycle life.[94]

As reported in the literature, composition influences not only the electrochemistry, but also the structural evolution. Volume expansion is unavoidable, yet too small to collapse the structure of PBA. However, Jahn-Teller effect could be a serious issue. Continuous lengthening/shortening in the bonding of HS Mn can lead to mechanical stress, and therefore cycling irreversibility and poor capacity retention. An insightful understanding in the structural evolution, as well as local geometry is essential to better choose the TMs composition in PBAs.

Electrolyte is also an important factor. In the literature, PBAs were studied in K-ion half-cells using 0.8 M KPF_6 in carbonate-based solvents, which were found to be instable towards K metal,[47] resulting in fairly low ICE, and battery failure with short lifetime. Therefore, finding an appropriate combination of salt, solvent(s) and concentration is a big challenge to bring PBAs into practical batteries.

Despite all the mentioned challenges, PBAs demonstrate plenty of merits as a promising family of cathode materials for PIBs. They can be obtained via facile synthesis method, and offer high capacity, high working voltages, and good reversibility. It is not exaggerated to say that PBAs are leading candidates for large-scale application of PIBs. Further chemical, morphological, and mechanical optimizations can improve the performance of PBAs, not just for lab-scale research, but also for mass production of practical PIBs.

1.4.2. Layer oxides

Layered materials, AMO_2 (A = alkali metal, M = 3d metals), have been intensively studied as cathodes for LIBs and SIBs for over four decades. Figure 1.13 illustrates the crystal structures of different types of layered oxides. These materials are built from MO_2 sheets consisting of edge-sharing MO_6 octahedra; and they are classified by the site (octahedral – O or prismatic – P) in which the alkali ions occupy and the number of MO_2 layers in a stacking repeat unit. While Li^+ tends to locate in an O site, bigger cations like Na^+ or K^+ prefer to stay in the P site.[35]

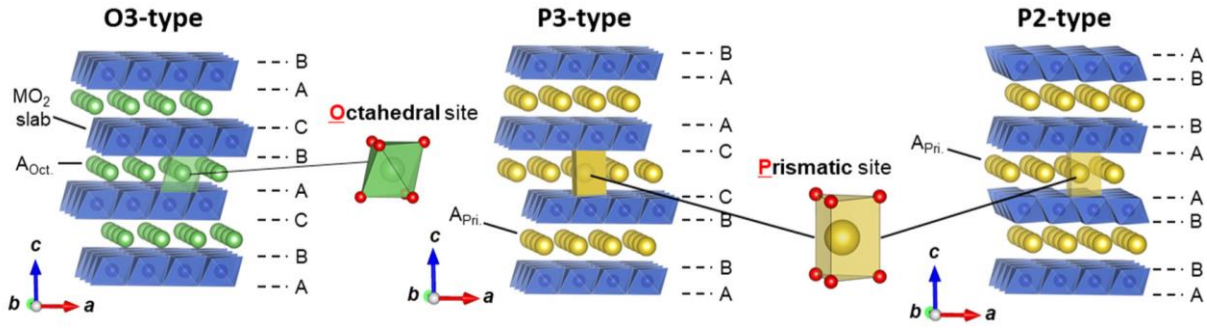

Figure 1.13. Schematic illustrations of the crystal structures of O3-, P3-, and P2-type A_xMO_2.[35]

In the last five years, an increasing number of studies on the electrochemical behaviors of K_xMO_2 compounds have been published. Most of them demonstrate inferior electrochemistry to Li- and Na- counterparts, in terms of operation voltage and capacity (Figure 1.14). Regardless the chemical composition and structure, the (de-)intercalation processes of K_xMO_2 occur below 4.0 V vs. K^+/K leading to lower power density.[35]. For example, P2- and P3- K_xCoO_2 provides a low reversible capacity (<*ca.* 60 mAh g^{-1}, equivalent to *ca.* 0.3 K^+ ion).[101] In contrast, P3-K_xCrO_2 exhibits high capacity (*ca.* 100 mAh g^{-1}) and long durability (up to 1000 cycles).[102] Nanotube $K_{0.7}Fe_{0.5}Mn_{0.5}O_2$ can deliver an initial specific capacity of 180 mAh g^{-1} maintaining 70 % at 20 mA g^{-1} after 45 cycles.[103]

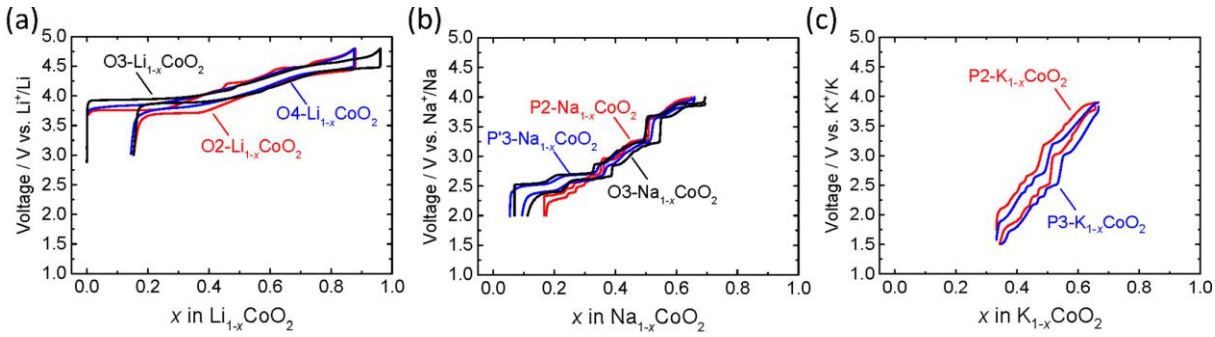

Figure 1.14. Galvanostatic cycling profiles of (a) O3-, O4-, and O2-type $LiCoO_2$ in LIBs, (b) P2-, P'3-, and O3-type Na_xCoO_2 in SIBs, and (c) P2- and P3-type K_xCoO_2 in PIBs.[4]

Theoretically, K-based metal oxides are good cathode candidates for PIBs. When prepared with appropriate compositions, they can demonstrate high volumetric and specific capacities. Yet one cannot deny that these materials suffer from many severe intrinsic disadvantages. Large interlayer distances due to the accommodation of K^+ ions are not favorable for the host, reflecting in low (de-)intercalation voltage and multiple phase transitions during the processes (Figure 1.14c)[104]. Additionally, air and moisture sensitivities can be serious problems, which require strict storage conditions and battery manufacture.[101]

1.4.3. Polyanionic compounds

Compared to PBAs or layered oxides, polyanionic compounds with the general formula $AM_x(XO_4)_y$, in which M is a TM and X is a non-metal element (e.g., P or S), display distinctive features, such as wide structural diversity and thermal stability (Figure 1.15).[105–107] To date, Fe- and V-based materials are the most attractive polyanionic frameworks for PIBs since they offer high capacity together with high working potentials.

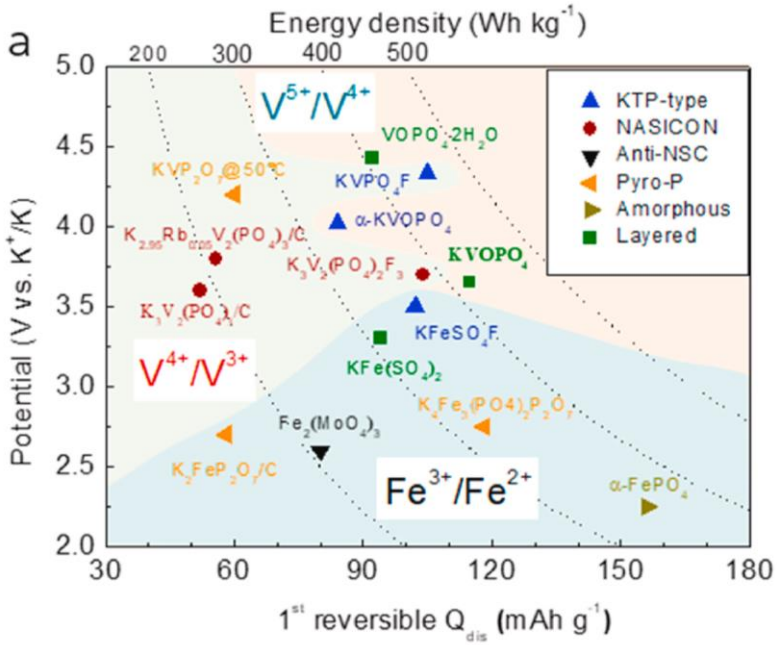

Figure 1.15. Polyanionic materials have been studied for K-ion batteries with their active redox couples, working potential initial discharge capacity (mAh g^{-1}) and energy density (Wh·kg^{-1}).[108]

Possessing wide 3D tunnels in the structure, polyanionic materials facilitate the diffusion of K^+ ions inside the framework. Less interstitial water and no vacancies are the features making this class somehow surpass PBAs. $KFeSO_4F$ was the first polyanionic material reported for K-ion batteries in 2012.[106] This material is isostructural to orthorhombic $KTiOPO_4$ (denoted as KTP, SG: *Pna2₁*) (Figure 1.16a), and it allows an insertion/extraction of 0.8 K^+ ion in the first cycle, equivalent to a specific capacity of 110 mAh g^{-1}. The material shows a good reversibility with capacity retention of 78 % after 20 cycles (Figure 1.16b).[107] Henceforth, there are more publications on polyanionic compounds. Amongst those, KTP-type materials have been intensively studied recently. Two famous representatives are $KVPO_4F$ and $KVOPO_4$.[109–111] Their electrochemistry is based on the redox reactions of V^{5+}/V^{4+} couple occurring above 4.0 V vs. K^+/K, which also makes them advantage over PBAs in term of energy density. However, their specific capacities are relatively low, *ca.* 80-90 mAh g^{-1} (Figure 1.16c,d)[109] comparing with those of MnFe- and FeFe-PBAs. Besides, working at high voltage (> 4.5 V) is a risk of electrolyte decomposition, and consequently, low CE and battery failure.

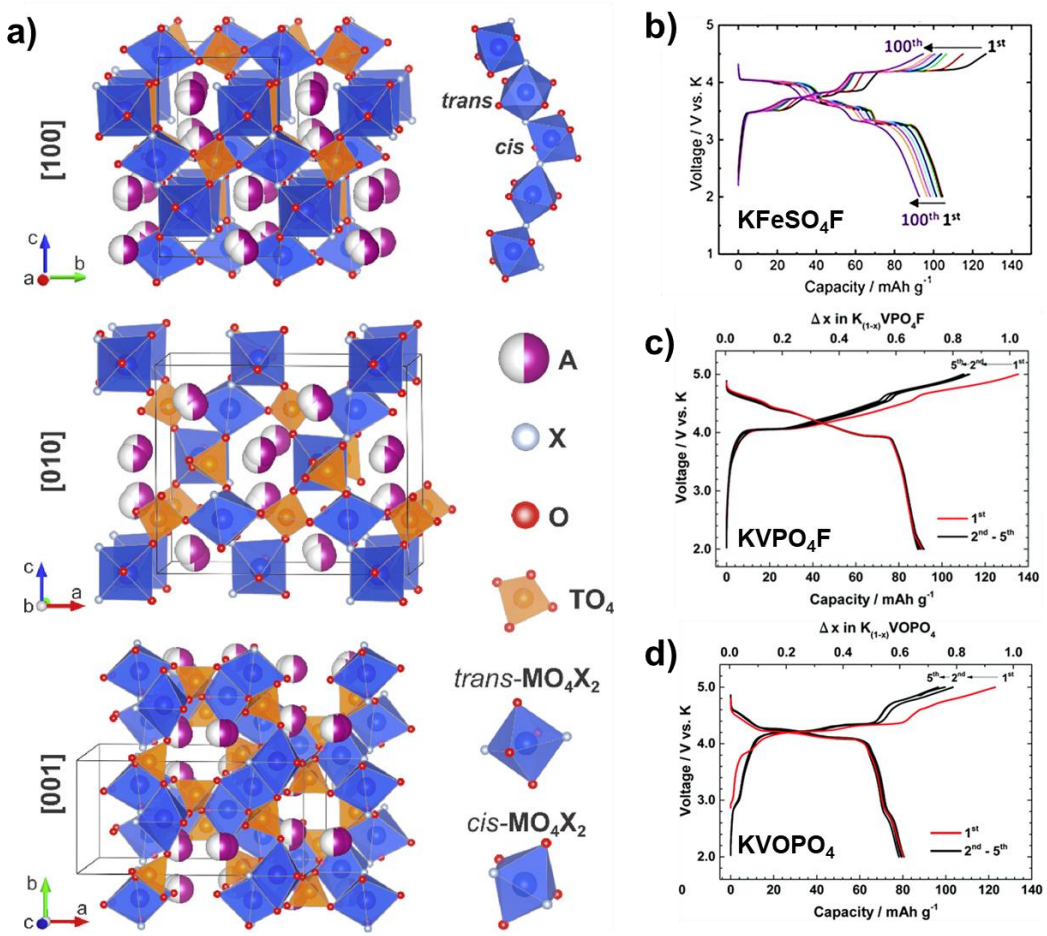

Figure 1.16. (a) Crystal structure of $KTiOPO_4$-type materials with different lattice planes[111] *and the cycling profiles of (b) $KFeSO_4F$*[107]*, (c) $KVPO_4F$ and (d) $KVOPO_4$*[109] *in K-ion half-cells.*

1.5. Electrolyte

In a battery, the electrolyte acts as a medium facilitating the ion transportation between two electrodes. In conventional LIBs, the electrolytes were made up of an inorganic salt ($LiPF_6$) dissolved in organic solvents (e.g., ethylene carbonate – EC, dimethyl carbonate – DMC, diethyl carbonate – DEC, etc.). Nowadays, there are various new electrolyte concepts based on varying the salts, solvents, concentrations, and their physical states (liquid or solid). Regardless the intrinsic properties, the electrolytes must meet the following criteria to be used in batteries:

- The electrolytes must possess good chemical and thermal stability.
- The electrochemical stability window (ESW) of the electrolyte needs to be larger than the operating voltage range of the cell. The ESWs of common electrolytes stay in the range from 0 to 4.5 V vs. K^+/K, therefore, electrolyte decomposition at high and low voltages is unpreventable.
- The electrolyte (especially liquid) must also allow fast cationic solvation/desolvation at an adequate charge/discharge current of the battery.

- The electrolyte must have high ionic conductivity (3×10^{-3} to 2×10^{-2} S cm^{-1}) over a wide range of temperature.
- Finally, simple preparation and low production cost are also required for practical application.

In PIBs, common electrolytes consist of a salt and single or mixed solvent(s) as those used in LIBs and SIBs. Each component strongly influences the electrochemical processes of the battery. A utilization of inappropriate electrolyte could render continuous SEI formation, and dendrite growth. Besides, a change in the solvent, or concentration can alter the electrochemical mechanism of negative electrodes, particularly graphite, and somehow can downgrade the battery performance. Each component of the electrolyte is discussed independently below.

1.5.1. Salts

KPF_6 was the first choice of most of the primary studies on the new materials of PIBs[37,95,109] thanks to the success of its lithium and sodium counterparts. The PF_6^- ion can passivate Al current collectors and avoid further corrosion, and contemporaneously decompose to form an SEI layer on the anode. However, solubility is a limit for KPF_6 usage, as its concentration cannot exceed 1.0 M in all common organic solvents. $KClO_4$ and KBF_4 cannot dissolve in the mixture EC/DEC,[4] meanwhile one can prepare highly concentrated electrolyte with KFSI (potassium bis(fluorosulfonyl)imide) and KTFSI (potassium bis(trifluoromethane)sulfonimide).[40,112] Besides, KFSI was found to be more stable towards K metal than KPF_6,[47] yet it decomposed at high potential in PBA | K half-cells, while KTFSI not only possess the same stability as KFSI, but also promote superior battery lifetime[113].

1.5.2. Solvents

Carbonate esters are use as solvents for electrolytes in LIBs. This class of electrolytes is blessed by their high dielectric constant, excellent solvation/devolation capability, and a wide ESW. Therefore, they have been employed in SIBs and PIBs. However, carbonates, *i.e.*, EC/DEC (v/v = 1/1), is not as compatible with graphite as electrolytes using 1,2-dimethoxyethane (DME, monoglyme), resulting in lower CE and cycling performance.[114]

DME and diglyme (bis(2-methoxyethyl) ether) are two well-known members of ether family. Their instability at high voltage (> 4 V), high denticity[115] (the ability to polychelate cations) enabling the unfavorable co-intercalation into graphite have limited their application in LIBs. Nevertheless, at high concentration, ether-based electrolytes can enhance the CE of

electrode materials,[40,113,116] forming stable SEI rich in inorganic compounds on graphite,[41,117] and thus, improve the cycling retention of batteries.

1.5.3. Status and challenges

So far, the question "What is the electrolyte of choice for PIBs?" has not yet got its answer. Extreme reactivity of K metal towards most of the chemicals used in batteries is one of the biggest obstacles. While Li- or Na-based electrolytes are mostly stable against their respective metals even when their batteries are working, K-containing electrolytes are reduced when contacting the metal,[47] thus, the results of long-term measurements in K-ion half-cells are not completely accurate and reliable. Besides, K-ion SEI is likely more fragile than those formed in LIBs and SIBs. Lower content of inorganic species in the SEI leads to higher chances of dissolution of its components,[118] consequently, a continuous electrolyte decomposition to reform the SEI is unpreventable. The additives, for instance FEC (fluoroethylene carbonate), which were successful in enriching the inorganic content and stabilizing the SEI in LIBs and SIBs, are likely helpless in PIBs. On one hand, FEC enhances the cycling retention of MnFe-PBA,[119] but on the other hand, it deteriorates the carbon anode performance,[120] induces non-ion-conductive SEI that obstruct the K^+ diffusion[121]

1.6. Scope of the thesis

As discussed in the previous sections of this introduction, graphite and PBA are among the most promising candidates as negative and positive electrodes for PIBs. This thesis aims at investigating the electrochemical mechanism of graphite and PBA, and finally at attempting to couple the materials to make K-ion full cells. The content of this PhD work is thus divided into three parts:

- Part 1: Interpreting the (co-)intercalation mechanisms of graphite when altering the concentration of KFSI in DME by combining *operando* XRD, FT-Raman spectroscopy, DFT calculations at different approaches.
- Part 2: Investigating the electrochemical properties of PBA $K_xMn_{2/3}Fe_{1/3}[Fe(CN)_6]$ in K-ion half-cells, and in-depth understanding the influence of local geometry and structural transformation on the electrochemistry of this PBA by the application of complementary techniques: Mössbauer spectroscopy, *operando* XRD and *operando* X-ray absorption spectroscopy (XAS).

- Part 3: Studying the long-term retention of PBA | Graphite full cells using highly concentrated electrolyte at different positive-to-negative mass ratios in two-electrode and three-electrode systems.

CHAPTER 2.
(CO-)INTERCALATION MECHANISMS OF GRAPHITE: FROM THE POINT-OF-VIEW OF CATION SOLVATION

Co-intercalation of cation and solvent molecules into graphite is a phenomenon commonly observed in alkali-ion battery systems when using ether-based electrolytes [32,40,42,122,123]. An increased salt concentration of the electrolyte can alter the electrochemical mechanism from co-intercalation to bare cation intercalation, particularly in PIBs. These mechanisms have commonly been associated with and suggested to originate from the stability of the formed SEI [41,43,44]; a thick inorganic-rich SEI formed by decomposition of highly concentrated electrolytes to act like a solvent-blocking layer preventing co-intercalation. Cation solvation was also found to be an important factor possibly controlling the storage mechanism [45,46].

Herein, the potassium (co-)intercalation of graphite is investigated by both experimental and computational methods. Galvanostatic cycling and *operando* XRD of graphite in K-ion half-cells using *x* M KFSI in DME (*x* = 1.0, 3.0, and 5.0) exhibits the electrochemical signatures and the staging evolution of the two mechanisms. Co-intercalation takes place when using a 1.0 M electrolyte and the process starts at *ca.* 0.8 V with a drastic interplanar expansion (~ 12 Å). The process occurs irreversibly, resulting in battery failure after a few cycles. In contrast, the 5.0 M electrolyte promotes bare K^+ intercalation, which occurs at lower potential with excellent reversibility and gentler structural breathing. For the medium concentration (3.0 M), both mechanisms were observed at their corresponding potentials and the two phases co-existed at the end of the discharge. Raman spectroscopy complemented by DFT calculations provides fruitful information about the cation solvation of the electrolyte in a wide concentration range that can explain the mechanism alteration as a function of salt concentration. Thermodynamics obtained from DFT calculations helps determining the conformational population of the DME molecules in the pure solvent, as well as the principal solvated species in the electrolyte. Computed Raman spectra of DME conformers at room temperature and their comparison to the experimental ones allows the conformational assignment of the observed bands for both free and coordinated solvent molecules, and enable the calculation of solvation numbers (SNs). At low and medium concentrations, the SN is approximately constant, *ca*. 2.7; while in highly concentrated electrolytes, the SN is < 2. The reduction of SN thermodynamically favors the K^+ intercalation. Additionally, Monte-Carlo (MC) simulation shows the presence of K^+ with 1 DME in the final co-intercalated phase, confirming the difference between the SNs, in agreement with potential difference between the two mechanisms. The electrochemistry, *operando* XRD and MC simulation were performed at ICGM, while the FT-Raman spectroscopy and DFT calculations were carried out at the Department of Physics, Chalmers University of Technology.

Potassium-ion batteries using KFSI/DME electrolytes: Implications of cation solvation on the K^+-graphite (co-)intercalation mechanism

Phuong Nam Le Pham[1,2], Vincent Gabaudan[1], Athmane Boulaoued[3], Gustav Åvall[3], Fabrice Salles[1], Patrik Johansson[2,3], Laure Monconduit[1,2,4] and Lorenzo Stievano[1,2,4]

1- ICGM, Univ. Montpellier, CNRS, Montpellier, France

2- Alistore-ERI, CNRS FR 3104, Amiens, France

3- Department of Physics, Chalmers University of Technology, Göteborg, Sweden

4- RS2E, CNRS, Amiens, France

(Published in *Energy Storage Materials*, 2022, 45, 291–300)

Abstract

Recently potassium-ion batteries have been proposed as a promising next generation battery technology owing to cost effectiveness and a wide range of electrode materials as well as electrolytes available. Potassium bis(fluorosulfonyl)imide (KFSI) in monoglyme (DME) is one potential electrolyte, wherein the K^+ solvation heavily depends on the salt concentration and strongly affects the electrochemistry. Pure K^+ intercalation occurs for highly concentrated electrolytes (HCEs), while co-intercalation is dominant for less concentrated electrolytes. The mechanisms are easily distinguished by their galvanostatic curves as well as by *operando* XRD. Here Raman spectroscopy coupled with computational chemistry is used to provide in-depth knowledge about the cation solvation for a wide concentration range, all the way up to 5 M KFSI in DME. Starting from pure DME experimental and computed Raman spectra provides a detailed conformational assignment enabling us to calculate the solvation number (SN) of K^+ by DME as a function of salt concentration for all the electrolytes. For low to medium KFSI concentrations, the SN is approximately constant, *ca.* 2.7, and/as there is a surplus of DME solvent available, while for HCEs, with much less DME available, the SN is <2. This reduced SN results in a thermodynamically more favored desolvation at the graphite surface, leading to intercalation, as compared to the higher SN of conventional electrolytes leading to co-intercalation, as observed also by electrochemical cycling.

2.1. Introduction

The rapid increase in the global energy demand urges for a faster development of additional energy storage technologies both to meet demand and circumvent/mitigate resource and cost issues [6]. It is today clear that much of that demand will be for electrochemical storage in the shape of various batteries – their efficiencies and versatilities lead the way [9]. Being commercialized in the early 1990s, lithium-ion batteries (LIBs) reign the power source market for a wide range of applications: from portable devices to electric vehicles [124,125]. This can lead to a depletion of lithium reserve in the Earth's crust [126] and therefore next generation batteries are needed. Amongst the post-LIB technologies researched, potassium-ion batteries (PIBs) have recently attracted huge interest owing to the high availability of potassium and foreseen comparable cell energy densities to both LIBs and some post-LIBs, such as sodium-ion batteries (SIBs) [35,127]. Moreover, potassium forms no alloys with aluminum, and hence there is, as for SIBs but in contrast to LIBs, no need for expensive copper current collectors.

Graphene-based materials recently attracted a huge attention due to their applicability in energy storage [128–131]. Amongst those, graphite – the well-known negative electrode material in commercial LIBs – has significant promise also for PIBs due to its ability to intercalate K^+ ions, with a resulting high reversible specific capacity of 278 mAh g^{-1}, corresponding to the formation of KC_8.[36–38,49,132,133] However, its electrochemical behavior strongly depends on the electrolyte; a conventional KPF_6 in EC/DEC electrolyte has relatively low compatibility, towards both graphite and K metal, and results in substantial capacity losses and relatively short cycle-life of cells [37,114]. In contrast, glyme-based electrolytes, in particular those based on 1,2-dimethoxyethane (a k a monoglyme, G1 or DME), such as the herein used potassium bis(fluorosulfonylimide) (KFSI) in DME electrolytes, have a high compatibility to both graphite [40,134] and K metal [113,135]. The electrolyte salt concentration, however, can alter the storage mechanism, and hence the capacity, as proven by graphite half-cell experiments to vary from $K(DME)_x$ co-intercalation to K^+ intercalation [39,40,136,137]. Both mechanisms, co-intercalation and intercalation, have already been thoroughly discussed in many reviews of LIBs and SIBs [32,42,122,123,138–140] and are commonly related to the presence of a stable solid electrolyte interphase (SEI) acting as a solvent-blocking layer [41,43,44,117]. The co-intercalation of Na^+ with diglyme in graphite occurs reversibly with excellent rate and cycling performance [141], either due to negligible SEI formed, both for graphite [142] and hard carbon [143], and/or a specific stabilization of the Na^+-diglyme complex (within graphite)[144]. Some recent reports on the stability of the SEI formed by DME-based electrolytes in PIBs show improved coulombic

efficiency and cycling retention of graphite [145,146], but its influence on the charge storage mechanism has not been clarified yet.

As an alternative and/or additional factor, the cation solvation has been suggested to affect the storage mechanism [45,46], as this is a function of the electrolyte salt concentration. At low salt concentrations each cation has a relatively stable first solvation shell, often predominantly composed of solvent, since weakly coordinating anions such as the FSI anion are often employed, and comparatively high solvation number (SN) and coordination number (CN). With increasing salt concentration, the SN at some point starts to decrease and this is often concurrent with anions replacing solvent, leading to contact ion-pairs (CIP) and higher aggregates (AGGs). We expected the same for KFSI in DME, but while many efforts have been made to understand the solvation of K^+-DME systems by Raman spectroscopy [116,135,147], yet none of them have provided an unambiguous picture. This is much due the conformational flexibility of pure DME, existing as five stable conformers: TGG, TGG', TGT, TTG and TTT at 20 °C [148], each having different cation coordinating properties. To resolve this, density functional theory (DFT) calculations together with Raman (or IR) spectroscopy can provide thermodynamic properties, *i.e.*, relative stabilities of both conformers and complexes, as well as Raman activities for each, and experimental verification with high accuracy.

Herein, we investigate the K^+ cation solvation for various differently concentrated KFSI in DME electrolytes by a combined Raman spectroscopy and DFT approach, and correlate this bulk local electrolyte structure to the observed storage mechanism in graphite followed by *operando* X-ray diffraction (XRD). To further clarify the intercalation mechanism Monte Carlo (MC) simulations were performed to provide additional information on the DME to K^+ ratio and organization in the interlayer spacing of graphite.

2.2. Experimental and computational methods

2.2.1. Sample preparation

KFSI (99.90%, Solvionic) and DME (99.50%, Sigma-Aldrich) were used as received. A series of KFSI in DME electrolytes was prepared by simple mixing of stoichiometric amounts using magnetic stirring, with solvent-to-salt molar ratios from 1.5 to 30, *i.e. ca.* 0.5 – 6 M, inside an argon-filled glove box (H_2O < 5 ppm, $O_2 \leq 1$ ppm). Pure DME and all electrolytes were stored in sealed glass vials before any measurements.

2.2.2. Electrode preparation and electrochemical tests

Graphite (SLP6, TIMCAL^{TM}) was mixed with carboxymethyl cellulose, CMC, as the binder with the mass ratio of 90:10 in deionized water using planetary ball milling. The slurry was then coated on copper foil (17.5 μm, Goodfellow) using the doctor blade method. The film was dried under vacuum at 80 °C for 12 hours and then cut into 12.7 mm diameter electrodes (area = 1.27 cm^2).

CR2032 coin cells of graphite were assembled in an argon-filled glove box using a potassium metal disk (Sigma-Aldrich, 99.5%) as the counter-electrode and a Whatman glass fiber separator. Three electrolytes, with DME:KFSI molar ratios of 15:1, 3:1 and 2:1, respectively, corresponding to *ca.* 1.0, 3.0 and 5.0 M, were selected for the electrochemical tests wherein the galvanostatic profiles were recorded at a current density of 25 mA g^{-1} in the voltage range 0–2 V vs. K^+/K using an MPG-2 (Biologic) potentiostat. In order to evaluate the role of the SEI, two specific experiments were carried out by cycling graphite | K half-cells using 1.0 and 5.0 M one single cycle, after which the SEIs are well-formed. Subsequently, the cells were cycled with "the other" electrolyte at the same current density.

2.2.3. *Operando* X-ray diffraction (XRD)

Operando XRD was carried out using a dedicated *in situ* electrochemical cell [149] equipped with a beryllium window as one of the current collectors onto which graphite powder was put. These experiments used a current density of 10 mA g^{-1} and diffraction patterns were collected on an Empyrean diffractometer (PANalytical) using Co Kα radiation in the 2θ range 15–43° for an acquisition time of 1 hour.

2.2.4. Raman spectroscopy

The Raman spectroscopy was carried out using a Bruker MultiRam FT-Raman spectrometer with a 1064 nm excitation line (Nd:YAG) at a laser power of 250 mW. Raman spectra were recorded between 200 and 1700 cm^{-1} at a resolution of 2 cm^{-1} and averaged over 2000 scans. For the more detailed analyses, the spectral region 680–1045 cm^{-1} was fitted to several Voigt profiles and deconvoluted using PeakFit^{TM}. The R^2 were 0.997 for pure DME and 0.999 for all other cases.

2.2.5. Computational chemistry

Optimized configurations for the five conformations of DME (TGG, TGG', TGT, TTG and TTT) and their complexes with K^+, $[K(DME)_x]^+$ (x = 1-5, depending on the conformer), were all obtained from DFT calculations using the Gaussian 16 software [150] at the M06-2X/6-

311++G(d,p) level of theory [151]. A polarizable continuum model (PCM) [152] using the dielectric constant of DME (ε = 7.2) was employed to implicitly account for solvation effects. The relative energies and entropies (E_r) were calculated using TGT as reference. The populations of DME conformers were considered to follow a Boltzmann distribution (Table 2.1). The binding energies (ΔE_{bind}) for the $[K(DME)_x]^+$ complexes were calculated as:

$$\Delta E_{bind} = E_{K(DME)_x^+} - (E_{K^+} + xE_{DME}) \quad (1)$$

The vibrational frequencies and Raman activities were subsequently computed analytically for the converged geometries as 2nd and 3rd derivatives of the energies, respectively. The vibrational modes were assigned manually using visualization in the Avogadro software [153]. Artificial Raman spectra for both pure DME and a few electrolytes were constructed using GaussSum [154] using a frequency scaling factor of 0.953 [155]and a FWHM of 16 cm^{-1}.

Complementary to the DFT calculations, classical Monte Carlo simulations were performed to investigate the plausible organization of DME and K^+ cations in the interlayer spacing of graphite (KC_x). Geometry optimizations were performed for DME in TGT conformation using DFT and the GGA/PBE functional and partial charges were determined using the Mulliken scheme in $DMol^3$, while the electronegativity equalization method (qEq as implemented in Materials Studio) was used for $K(DME)_xC_y$. For $[K(DME)_x]$ the charge was fixed to 1. For the Monte Carlo simulations, the Universal Force Field (UFF) was used to reproduce the Lennard Jones (LJ) interactions [156] and NVT calculations [157], with a fixed number of cations (required to have a neutral system as a function of the KC_x composition) and molecules (corresponding to the saturation of the interlayer spacing), were performed at 300 K, with 5 million steps for equilibration and 2 million steps for production. The electrostatic interactions were calculated by Ewald summation [157], while the short-range contributions corresponding to LJ parameters were computed using the Lorentz-Berthelot rules. Simulations were conducted using multi-cells, 6 × 3 × 1 unit cells, consistent with a cut-off distance for LJ interactions at 12 Å, and built with the experimentally determined interlayer spacing.

2.3. Results and discussion

The evolution of the storage mechanism as a function of the electrolyte salt concentration and of both galvanostatic and *operando* XRD profiles is introduced first, followed by the investigation of the solvation of K^+ in DME by the combined DFT-Raman spectroscopy approach. Finally, these findings are used to gain insight into the possible influence of cation solvation in the storage mechanism of potassium ions in graphite.

2.3.1. Intercalation mechanism

The galvanostatic profiles and the evolution of the capacity with cycling of K | graphite half-cells using electrolytes with different concentrations are shown in Figure 2.1. The electrochemical profile of the half-cell containing the least concentrated electrolyte, 1.0 M, is typical of co-intercalation, with a high-potential pseudo-plateau at 0.8 V and a relatively low reversible capacity (92 mAh/g). These results thoroughly agree with previous works on the potassiation of graphite using a KPF_6 in DME electrolyte [39,114]. During the second discharge, an irreversible phenomenon occurs between 0.1 and 0 V, which rapidly leads to the complete inactivation of the battery after only a few cycles. The origin of this phenomenon, not observed during the first discharge, is not yet completely understood. Indeed, in the case of Na//graphite systems undergoing co-intercalation, such a behavior was attributed to the decomposition of FSI, whereas significant CO and C_2H_4 gas evolution was observed at low potentials, and H_2 gas evolution in symmetric sodium cells, showing that the salt is unstable towards both graphite during co-intercalation reactions and sodium metal.[158] Previous works using KPF_6-based glyme electrolytes did not produce such a low voltage plateau during potassium co-intercalation in graphite [39] indicating that the choice of salt is crucial for the stability. Nonetheless, the possible degradation path of the FSI anion is unclear, and might involve possible redox shuttle species that are formed only after a full potassiation/depotassiation cycle. Moreover, one cannot exclude that such a low potential process represents potassium plating on the surface of graphite caused by the capture of solvated cation in the growing SEI layer [159], a common issue reported for LIBs [160,161].

Nevertheless, the lack of the typical pattern of K metal in the operando XRD data does not support the formation of such phase along the low potential plateau.

When using the 5.0 M electrolyte, only two low-potential plateaus are observed, with a corresponding reversible capacity of *ca.* 280 mAh/g. Here, the charge/discharge curves for the first and the second cycles are similar to those obtained for the simple intercalation of K^+ in graphite using carbonate-based electrolytes [31,132,162].

The most puzzling charge/discharge profile, however, is that of the 3.0 M electrolyte: a reduced high-potential pseudo-plateau is followed by two additional plateaus at 0.25 and 0.15 V, with a reversible capacity of 270 mAh g^{-1} combined, which is close to the theoretical value for the formation of KC_8 (279 mAh g^{-1}). Interestingly, the shape of the curve is similar to the sequential combination of the processes observed for the 1.0 M and 5.0 M electrolytes. The

first plateaus contribute with ca. 40 mAh g^{-1} to the total capacity of the first discharge, while at the end of the low potential plateau a total capacity of *ca.* 300 mAh g^{-1} is observed.

Such a large capacity exceeds the theoretical one for graphite corresponding to the formation of KC_8, the excess capacity being possibly due to sluggish mass transport of the inserted species exiting the host and irreversible capacity loss caused by the decomposition of the electrolyte. Indeed, a more reasonable reversible capacity of 250 mAh g^{-1} is recovered during the following charge.

The evolution of the capacity upon cycling (Figure 2.1b) is very bad for the cell with the least concentrated electrolyte, whereas an excellent reversibility was observed for the other cells, with a Coulombic efficiency approaching 100 % after a few cycles.

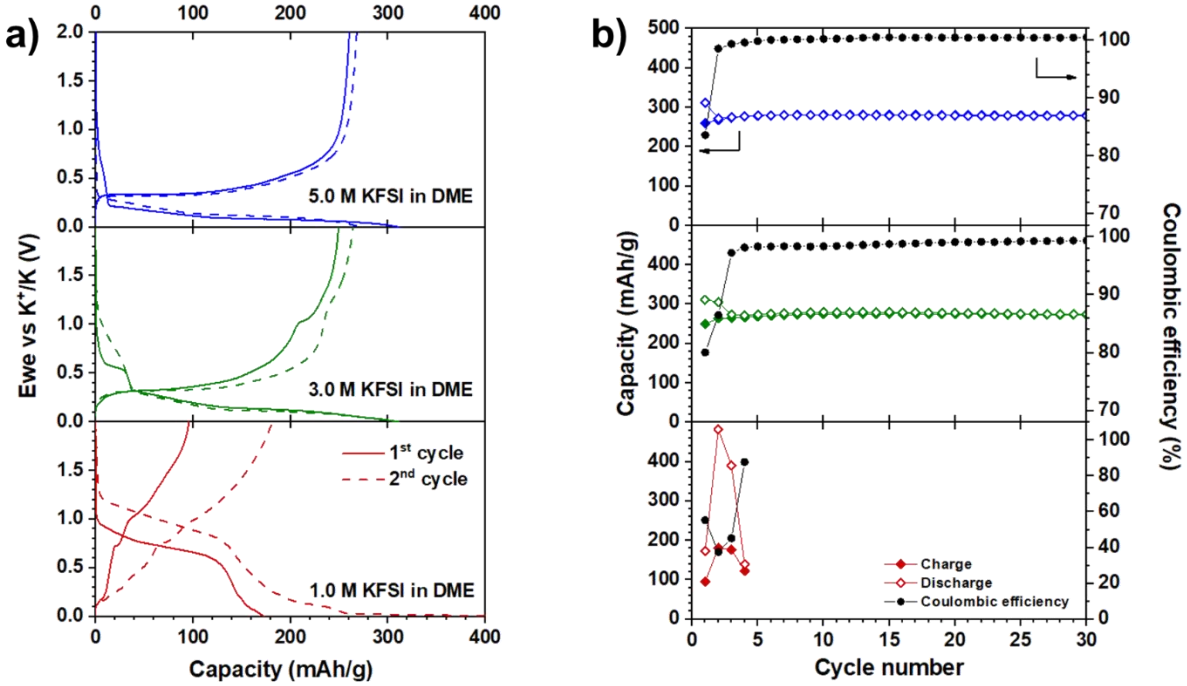

Figure 2.1. (a) Galvanostatic profiles and (b) capacity as function of cycling of K/graphite half-cells using X M KFSI in DME electrolytes (X = 1.0, 3.0, 5.0)

The above changes and differences can be correlated with a change from co-intercalation to intercalation storage mechanism, as shown by *operando* XRD during the first cycle for the K | graphite half-cells (Figure 2.2). For all three cases, the evolution of the diffraction patterns with K^+ insertion show typical features of a staging process: the main graphite peak (002) splits into two new peaks, one at lower and one at higher angles, indexed as (00*l*) and (00*l*+1), respectively (Figure 2.2). No significant changes in the position and intensity of the main graphite peak (002) are observed during the initial part of the discharge (between 1.4 and 1.0 V), implying that in all cases this part of the discharge corresponds to the irreversible decomposition of the electrolyte. At lower potentials, the (002) reflection splits and the (00*l*) and (00*l*+1) peaks shift progressively to lower and higher angles, respectively, indicating the formation of successive graphite intercalation compounds (GICs) through a classical staging process. As the shifts depend on the electrolyte, distinct GICs are formed. The application of Bragg's law allows determining the *l* value (cf. SI) and leading to a small *c* parameter and thus small interlayer spacing between two consecutive graphene sheets for the half-cell with the 5.0 M electrolyte. In contrast, there is a larger c parameter and thus a larger interlayer spacing for the half-cell with the 1.0 M electrolyte. At the end of discharge, we observe characteristic peaks centered at 19.25° (5.0 M) and 17.41° (1.0 M) corresponding to *d* spacings of 5.35 and 12.02 Å, respectively. According to previous works, the former corresponds to the typical interlayer distance of KC_8 [4,122,162], whereas the latter can be explained only assuming the formation of a co-intercalation phase [39,40,137,163].

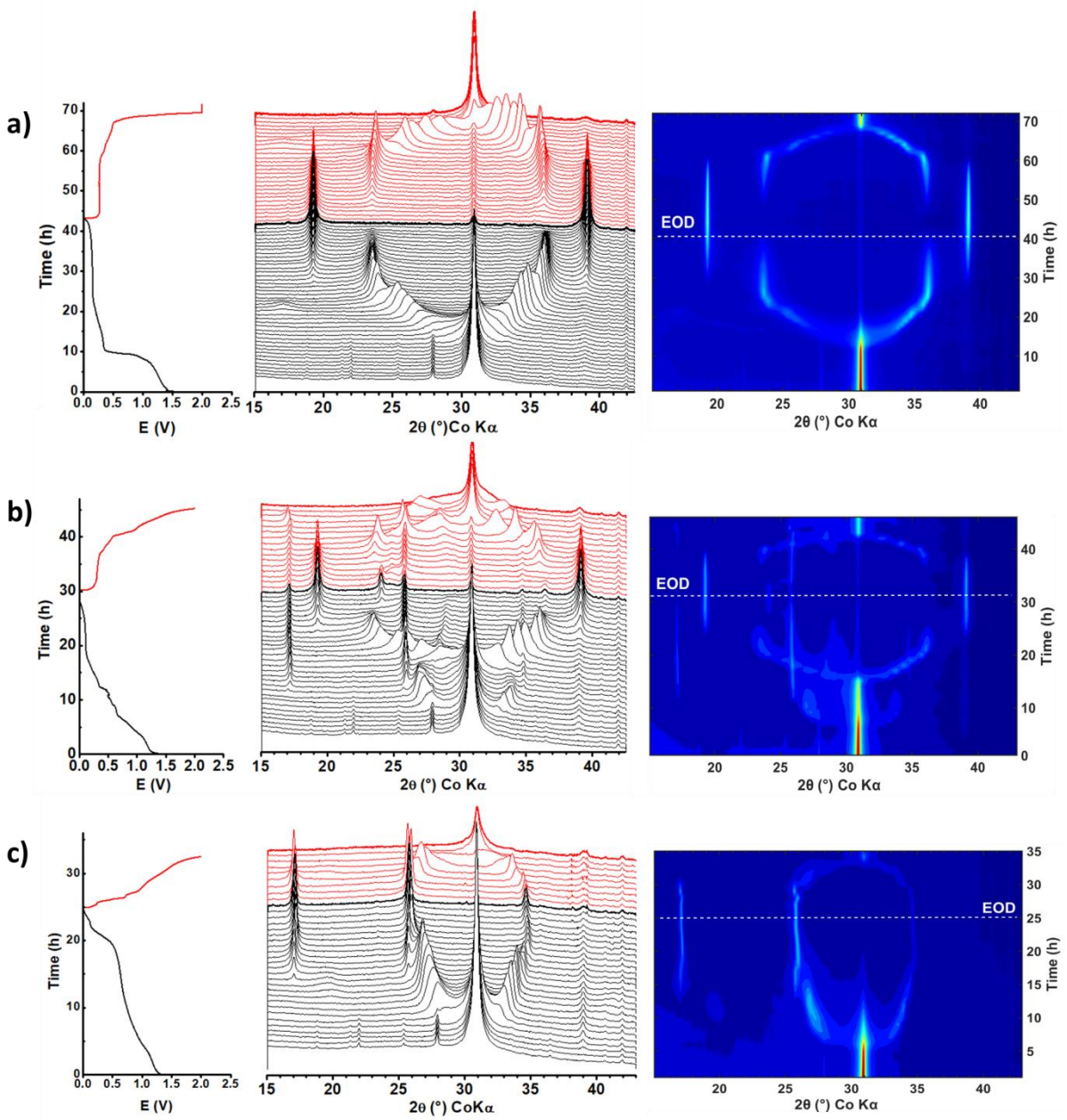

Figure 2.2. Galvanostatic profiles (left), operando XRD diffraction patterns (middle) and contour plots (right) of K/graphite half-cells cycled at 10 mA/g using X M KFSI in DME electrolytes: 5.0 M (a), 3.0 M (b), and 1.0 M (c)

The most interesting case, however, remains that of the intermediate 3.0 M concentrated electrolyte. In this case, (Figure 2.2b) a staging process resembling that of co-intercalation starting from 0.9 V is observed, and the system has almost finished transitioning from a stage III to a stage II compound[163]. The end member of the co-intercalated phase is completely formed at *ca.* 0.6 V and maintains stably also at lower potentials with respect to the pseudo-leveling surface area and the intensity of its characteristic peak at 17.41 ° remains until *ca.* 0.1 V (Figure 2.3b,e). Starting from 0.3 V, the typical features of intercalation appear with the rise of

00l signal (19.25 °) between 0.1 and 0.0 V. Even though the peaks of the co-intercalated species slightly decrease in intensity during the K^+ intercalation, the main peaks of both intercalated and co-intercalated graphite are observed at the end of discharge (EOD).In the charge, the co-intercalated phase retains unchanged up to *ca.* 1 V during which bare K^+ ions exit from the host, with similar plateaus resulting in the galvanostatic profiles as well as a similar decrease of the innate peaks in the XRD patterns as observed for the pure mechanism (Figure 2.3), which confirms the mechanisms being sequential.

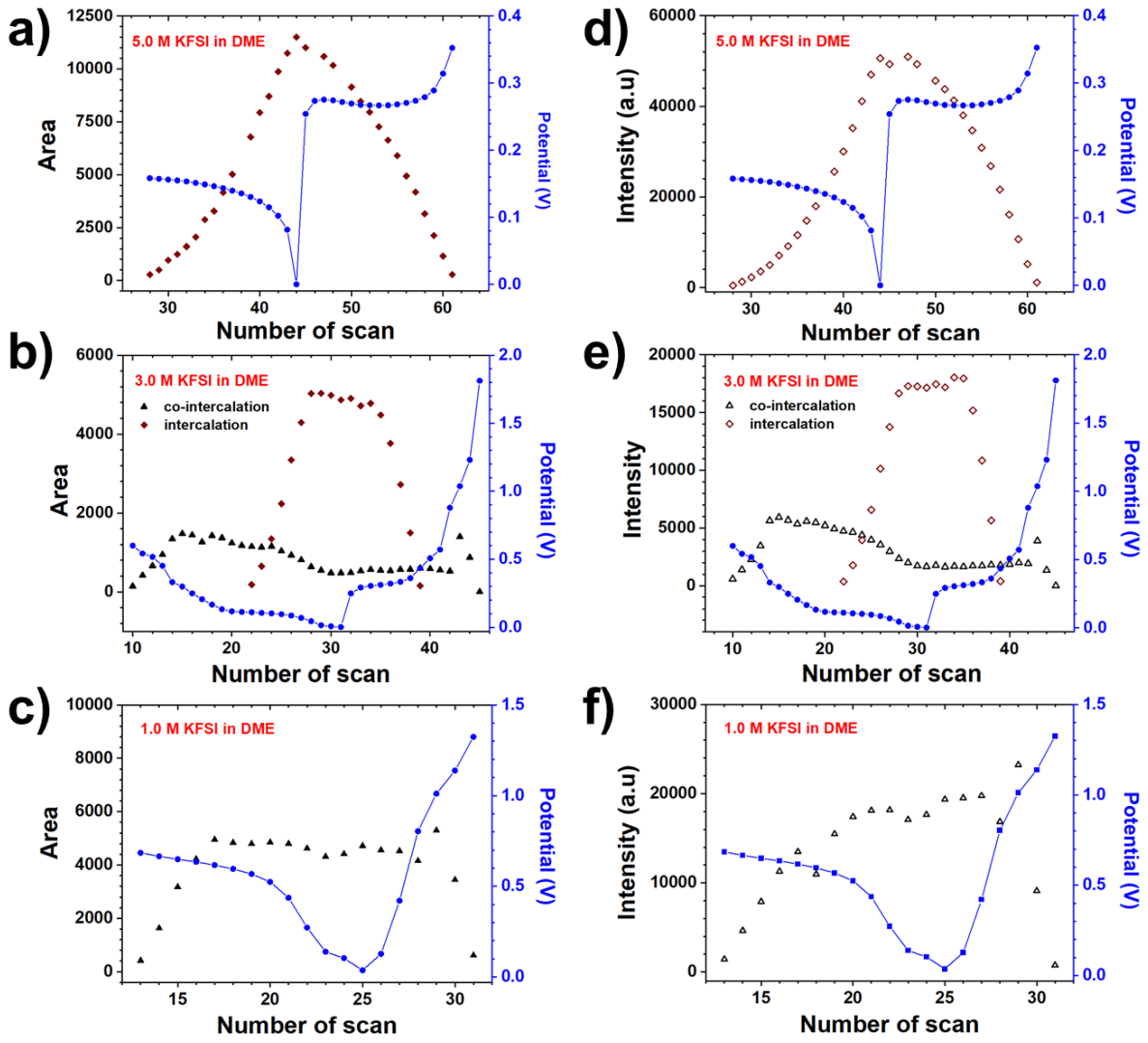

Figure 2.3. Evolutions of the surface areas (a, b, c) and intensities (d, e, f) of the characteristic peaks at 19.25 ° and 17.41 ° corresponding to intercalation and co-intercalation mechanisms, respectively during the first cycle.

An additional peak at about 26°, coupled to a peak of weaker intensity at 36.5°, appears at the end of discharge for the 3.0 M electrolyte. This specific XRD signature, which is not present in the other two systems, might be due to the formation of regularly ordered, alternating, intercalated and co-intercalated layers in a single graphite stack. Indeed, such peaks would

correspond to a calculated *d* spacing of 8.59 Å, very close to the average of the values obtained for the 1.0 and 5.0 M electrolytes. Such an average interlayer distance could thus correspond to the formation of alternated intercalated and co-intercalated layers.

Indeed, considering the value of the capacity reached at the end of the co-intercalation process (about 40 mAh/g), the transition from a stage III to a stage II compound should be just about to complete according to the detailed operando study of Li *et al.*[163] Therefore, as a stage II compound has already formed during the co-intercalation process, when the intercalation begins at 0.25 V the system cannot undergo the same stacking sequence as seen for the 5 M electrolyte, instead the bare K^+ must intercalate into the empty layers stacked between layers filled with co-intercalated species. This result, completely new and unexpected compared to the previously published studies, prompted us to investigate the solvation structure of the distinct electrolytes in order to understand the modification of the mechanism as a function of electrolyte salt concentration.

2.3.2. Cation solvation

Before addressing in detail the cation solvation in the KFSI/DME system, it is necessary to revisit the conformational population in liquid DME. By applying Boltzmann distribution (Eq. 1) to pure DME at 20 °C based on relative electronic energies and entropies (Table 2.1), we find TGT to be the dominant conformation, in agreement with the literature [148,164,165]. Furthermore, the TGT and TGG conformers form the most stable complexes with K^+, likely due to bidentate chelation by two oxygen atoms (Figure 2.4). A slightly smaller ΔE_{bind} of TGG as compared with TGT (1.1 kJ/mol) can be explained by a smaller decrease in the dihedral angle $O_1C_2C_3O_2$ from free to coordinated species (70.8 ° to 60.4 ° for TGT, 58.8 ° to 56.6 ° for TGG). In contrast, the *trans* position of the oxygen atoms in TTG and TTT only allows these conformers to form mono-dentate coordination. Finally, despite the preferred *gauche* position of the oxygen atoms in TGG', the steric effect of *g'*-CH_3 seems to play a significant role in preventing K^+ from being bi-dentately coordinated, why $[K(TGG')]^+$ is the least stable species in this series.

Table 2.1. Relative entropies (S_i), relative energies (E_i), and conformer populations of pure DME, and the binding energies (ΔE_{bind}) of their mono-ligand complexes $[K(DME)]^+$.

Conformer	S_i (J mol^{-1} K^{-1})	E_i (J mol^{-1})	n_i/n_{TGT}	n_i			ΔE_{bind} (kJ mol^{-1})
					(*)	(**)	
TGT	0	0	1	0.448	0.45	0.42	-47.2
TGG	–1.482	3703	0.183	0.082	0.08	0.09	-48.3
TGG’	3.573	3100	0.462	0.207	0.17	0.33	–18.7
TTG	7.715	6600	0.183	0.082	0.09	0.04	-21.6
TTT	–1.933	1652	0.402	0.180	0.18	0.12	-21.2

(*)Molecular dynamics simulations data [165].

(**)Raman spectroscopy data [148].

The evolution of the binding energies of the $[K(TGT)_x]^+$ complexes show that it increases as a function of SN with negligible changes in the average K–O distances for x = 1–4 (Figure 2.5), while for x = 5, the average K–O distances increases drastically with a large spread. It can be deduced that the optimal SN is 4 and the CN = 8. For x > 4 (e.g., 5), some of the TGT DME solvent may move to the 2nd solvation shell (Figure 2.6).

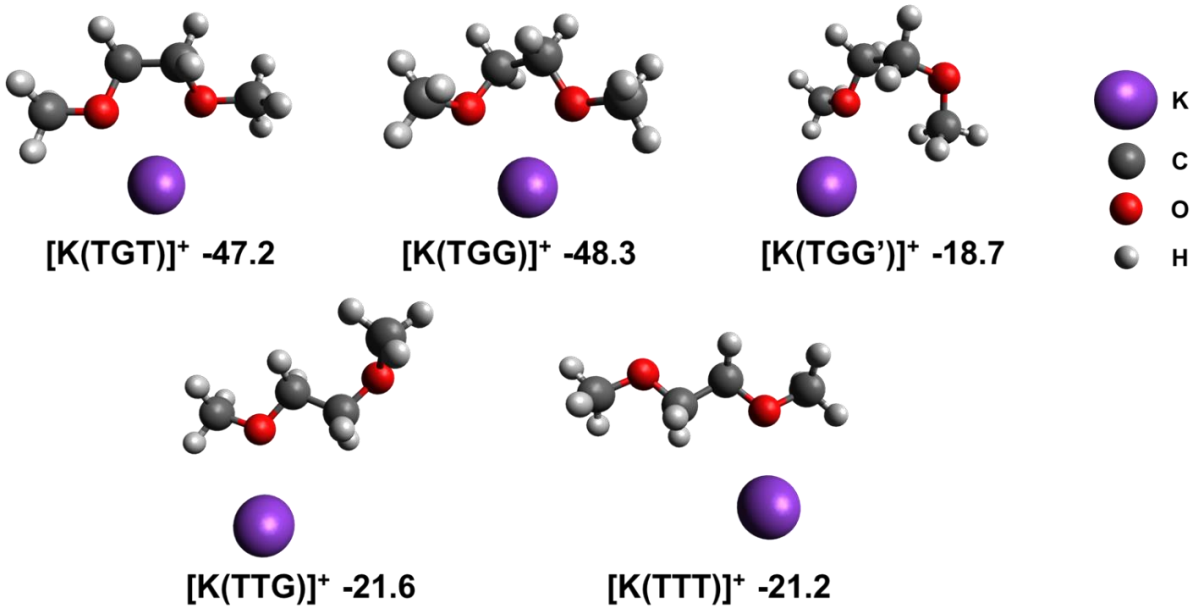

Figure 2.4. Optimized geometries and binding energies for [K(DME)]+ complexes.

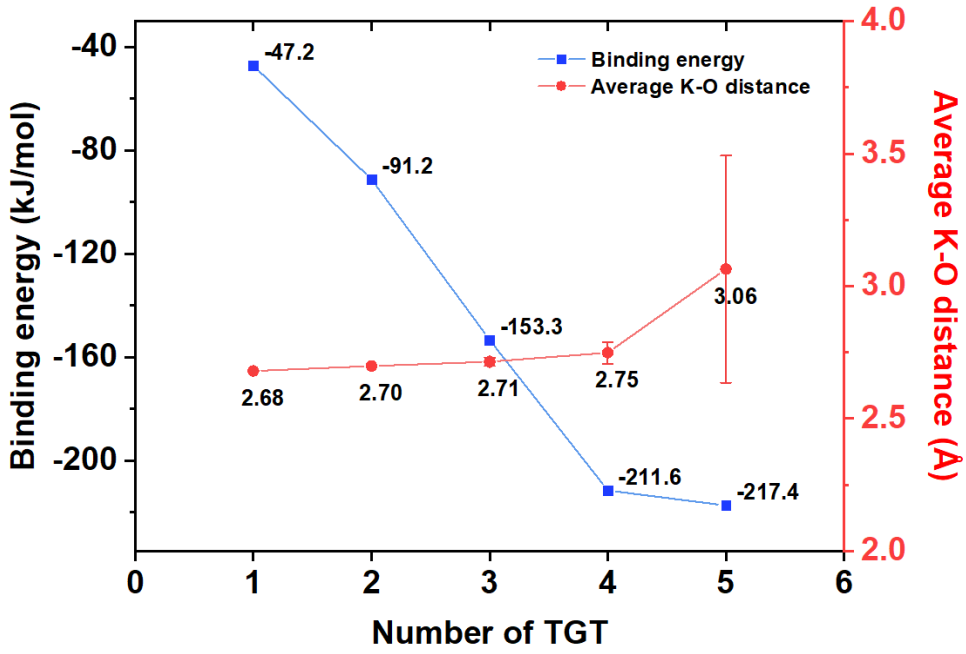

Figure 2.5. Binding energies and average K–O distances as function of K+-coordinated TGT conformer DME solvents.

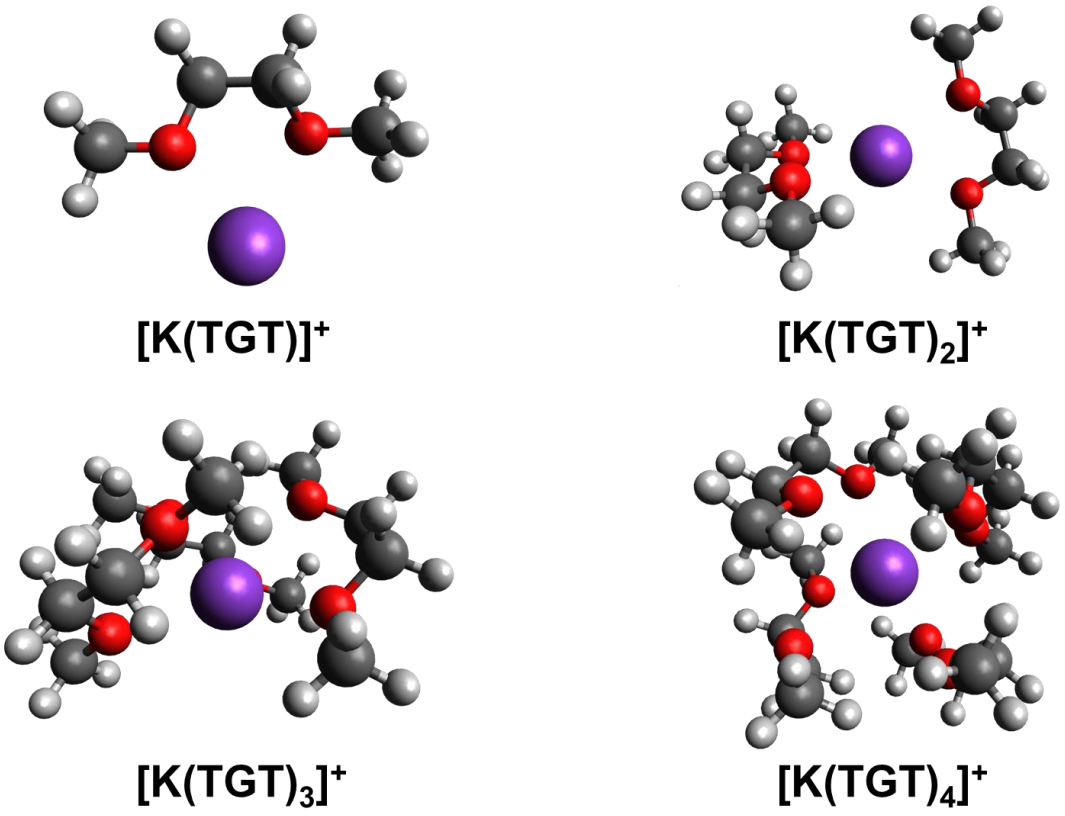

Figure 2.6. Optimized geometries of $[K(TGT)_x]^+$ (x = 1-4).

In the experimental analysis of the solvates by Raman spectroscopy, the region 800–900 cm^{-1} contains the characteristic vibrations of both free and K^+-coordinated DME, ideally also with conformational discrimination, but this region is difficult to analyze due to severe overlaps. By employing the DFT calculations and comparing with deconvoluted spectra, however, the contributions from each conformer to each peak could be unveiled.

First, the deconvoluted Raman spectrum of pure DME (Figure 2.7) exhibits two strong wide bands at 817 cm^{-1} and 845 cm^{-1} corresponding to the CH_2 rocking modes, and some overlapped C–O stretching bands of all conformers [166]. Previous spectroscopic work on DME have ascribed some contribution from TTG and either TTT or TGG'[166,167], but our DFT calculations indicate that only the conformers having their oxygen atoms at *gauche* position (TGG, TGG' and TGT) exhibit strong Raman activities, while TTT and TTG have non or negligibly small activities (Table 2.2). Therefore, the latter conformations are disregarded. On the other hand, each of the three species TGG, TGG' and TGT possesses two strong Raman vibrations in this region: one is the symmetrical CH_2 rocking mode, and the other could be either an asymmetrical CH_2 rocking mode (TGG' and TGT) or the combination of different vibrations (TGG). While these vibrations of TGG and TGG' scatter at two separated excited states, those of TGT seem to have the same Raman shift. Additionally, the minute errors (*ca.* 1%) show a very good agreement between the (scaled) calculated frequencies[168] and experimental data (Table 2.2). From this, the peak at 817 cm^{-1} is assigned to TGG and TGG', and the peak at 845 cm^{-1} to TGG, TGG' and TGT.

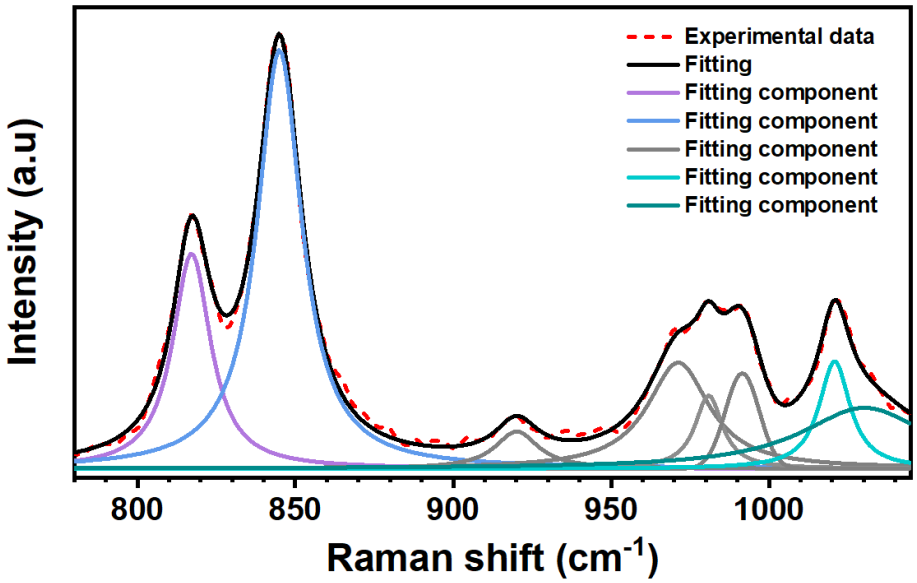

Figure 2.7. Deconvoluted Raman spectrum of pure DME in the region of 780 – 1045 cm^{-1}.

Table 2.2. DFT computed Raman data incl. globally scaled frequencies (× 0.953) and experimental data.

Species	Calculated			Experimental Shift (cm^{-1})
	Shift (cm^{-1})	Activity ($Å^4$)	Scaled shift (cm^{-1})	
TTT	839	0	800	--
TGG	865 (s)	12.6	824	817
	882 (*)	26.9	841	845
TGG’	851 (s)	24.6	811	817
	911 (as)	15.0	868	845
TTG	819 (as)	0.5	780	--
TGT	885 (s)	8.8	843	844
	887 (as)	25.5	845	
$[K(TGT)]^+$	873 (s)	5.5	832	--
	888 (*)	33.9	857	
$[K(TGG)]^+$	857 (s)	10.5	817	--
	888 (*)	33.3	846	

The effect of KFSI in DME can be observed by following Raman spectra of the electrolytes with increasing salt concentration (Figure 2.8). Based on assignments previously set for LiFSI [169] and for glyme-based electrolytes [116,147,170], the deconvoluted KFSI-DME spectra have; contributions at 717, 727 and 737 cm^{-1} that are assigned to free FSI anions (or solvent-separated ion-pairs, SSIPs), CIPs of K-FSI and AGGs, respectively; contributions at 817 and 845 cm^{-1} from free DME; and, finally, contributions at 827 and 855 cm^{-1} from coordinated DME in the TGT conformation (Figure 2.9). The large right-tailing peak at 700–780 cm^{-1} results from the S–N stretching mode of FSI anions [135,169,171–173]. As the salt concentration increases, the peak exhibits a blue shift, indicating the formation of CIPs and/or AGGs. Based on the evolution of fitted peak intensities, we divide *the plot* into two regions: low concentration (LC) region (< 5.0 M, or DME:KFSI > 2), and high concentration (HC) region (≥ 5.0 M). In the LC region, even in the most dilute electrolytes (< 1.0 M) CIPs exists, but free FSI is the dominant anion species. With increasing salt concentration, the proportion of free FSI follows a parabolic function (Figure 2.6), while, the CIPs increase. When

DME:KFSI ≥ 3, the AGGs increase and become dominant in the HC region. A small amount of free FSI anions still exists in the 5.0 M electrolyte, but disappear when more salt is added.

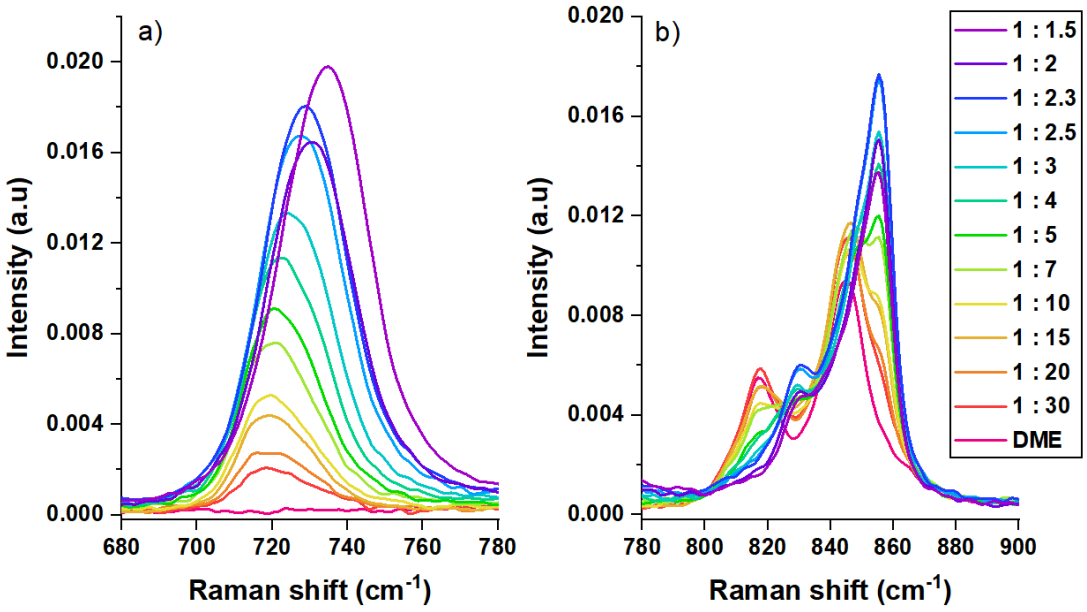

Figure 2.8. Raman spectra of DME and the electrolytes: (a) S–N stretching modes of the FSI anion, and (b) CH_2 rocking modes of the DME solvent.

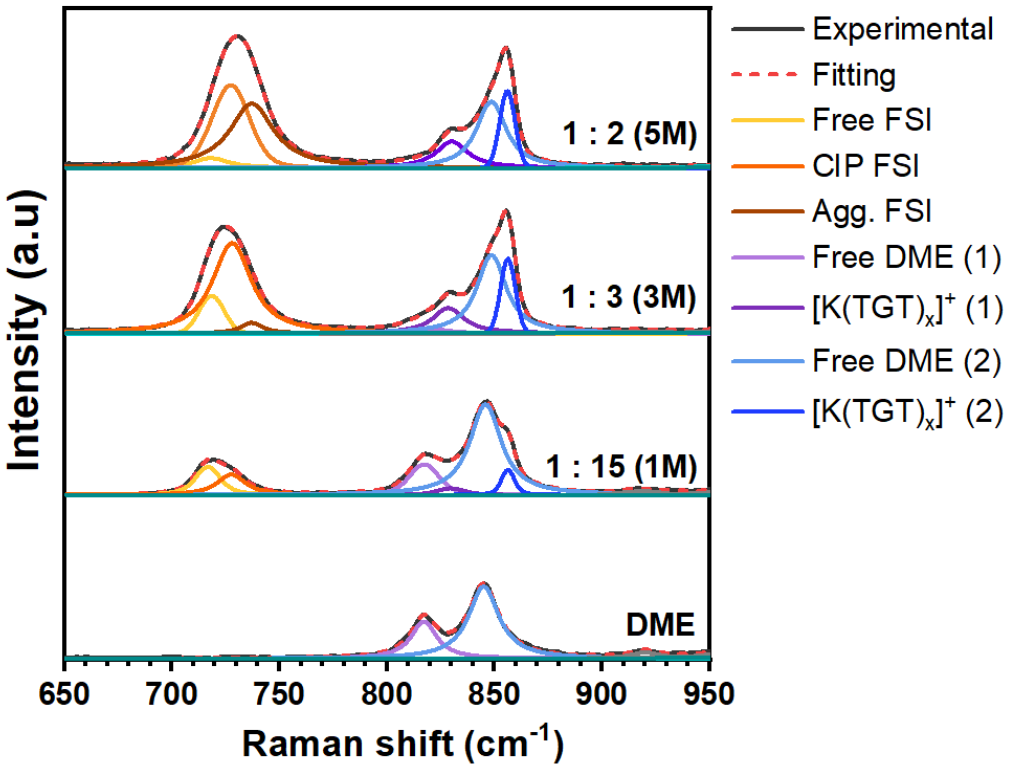

Figure 2.9. Experimental spectra for KFSI in DME electrolytes at different concentrations and pure DME including deconvoluted peaks.

In the DME region, the peak at 817 cm^{-1} decreases and this could be due to less free TGG and TGG', as two new peaks at 827 and 855 cm^{-1} increase as function of salt concentration (Figure 2.7b). Indeed, Hosaka *et al.* [116] concluded the latter comes from coordinated DME and Liu *et al.* [147] assigned them to C–O bonds in DME coordinated to K^+ without any contribution from the CH_2 groups. In contrast, we believe that both CH_2 and C–O groups contribute (Table 2.3) also as the calculated Raman activities (Table 2.2) suggests assignment to CH_2 rocking mode solely or mixed with C–O stretching vibrations of coordinated DME in TGT conformation, respectively. In contrast to the gradual reduction of the peak at 817 cm^{-1}, the peak at 845 cm^{-1} seems to be unchanged in the LC region and then slightly decreases at higher concentrations (Figure 2.10). According to our DFT data, there are two possible solvates, by TGT and TGG, respectively, as their binding energies are very close. The vibrational modes of TGG at 817 and 845 cm^{-1} are not shifted upon coordination (Table 2.2), which makes coordinated TGG hard to discern. The Raman activity of the vibration at 845 cm^{-1} of coordinated TGG is much stronger than that at 817 cm^{-1}, and while the peak at 817 cm^{-1} only has contributions from free and coordinated TGG, the peak at 845 cm^{-1} also has contributions from free TGT and hence the different evolutions of these peaks. However, as the absolute population of TGG is much lower than TGT, we consider $[K(TGT)_x]^+$ to be the major cation solvate species in the system.

Table 2.3. Conformational contributions to the Raman observations in the range of 780 – 1045 cm^{-1} with computed activities. The peaks were assigned based on literature [166] and the scaled shifts.

Shift (cm^{-1})	**Intensity (a.u)**	**Component**	**Scaled shift (cm^{-1})**	**Activity (Å^4)**	**m (*)**
817	4.55E-03	TGG	824	12.6	7.42E-04
		TGG’	811	24.6	
845	9.05E-03	TGG	841	26.9	4.37E-04
		TGG’	868	15.0	
		TGT	843	8.8	
			845	25.5	
920	5.66E-04	TTG	924	30.5	2.26E-04
970	1.70E-03	TGG	974	21.7	3.35E-04
		TTG	976	40	
980	1.59E-03	TGG’		10.5	7.32E-04
991	1.83E-03	TTT	998	52.3	2.53E-04
1019	2.33E-03	TGG	1015	15.1	2.53E-04
		TGT	1020	12.5	
			1021	17.8	
1030	1.32E-03	TGT		4.0	7.37E-04
		TTG	1035	17.0	
	Average *m* value				4.24E-04 ± 2.12E-04

(*) *m* is an adjusted factor calculated from the equation: $I_{peak} = m \times \sum n_i \times a_i$

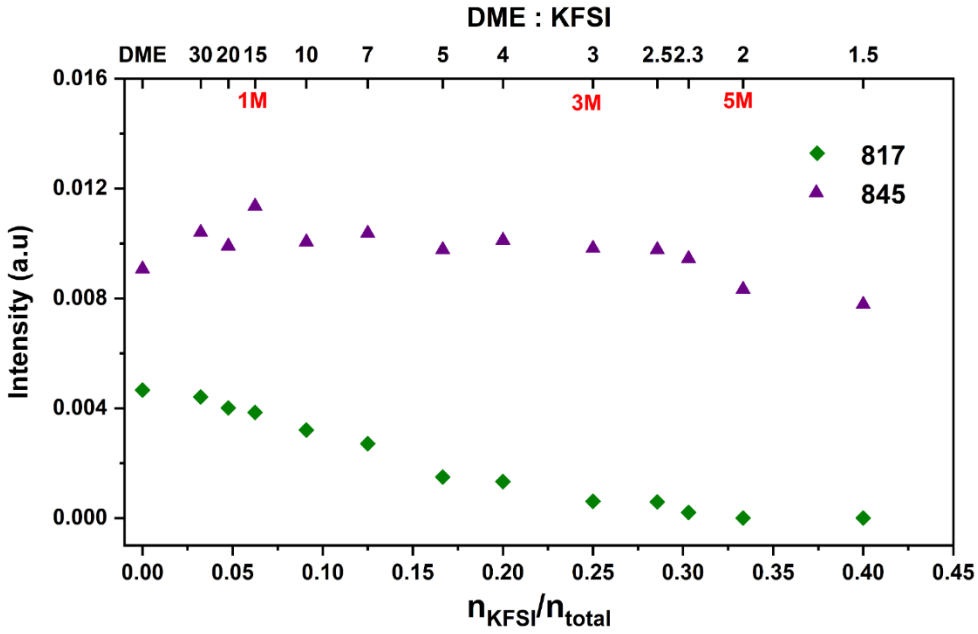

Figure 2.10. Evolution of 817 and 845 cm^{-1} deconvoluted peaks as functions of salt molar fraction/concentration.

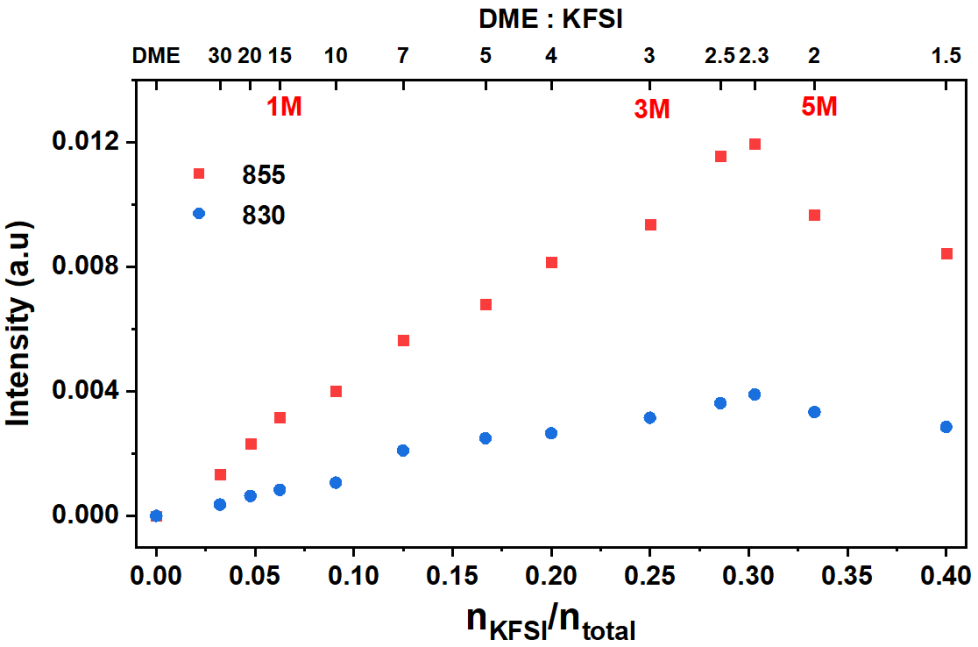

Figure 2.11. Evolution of 830 and 855 cm^{-1} deconvoluted peaks as functions of salt molar fraction/concentration.

The evolution of the peaks assigned as coordinated TGT at 855 and 830 cm^{-1} (Figure 2.11) show the same trend: both increase linearly as function of salt concentration up to a KFSI:DME = 1:2.3 ratio, after which they decrease again. Artificial spectra of $[K(TGT)_x]^+$ complexes show that the peak positions negligibly change and the Raman activities to be linear functions of the number of coordinated DME in TGT conformation (Figure 2.12). We deduce

that these peaks have the same origin, *i.e.*, $[K(TGT)_x]^+$. In the LC region, the peak intensities are linear functions of the molar fraction of KFSI, which means that the average SN is almost constant, but in the HC region the peak intensities decrease, hence reduced SNs.

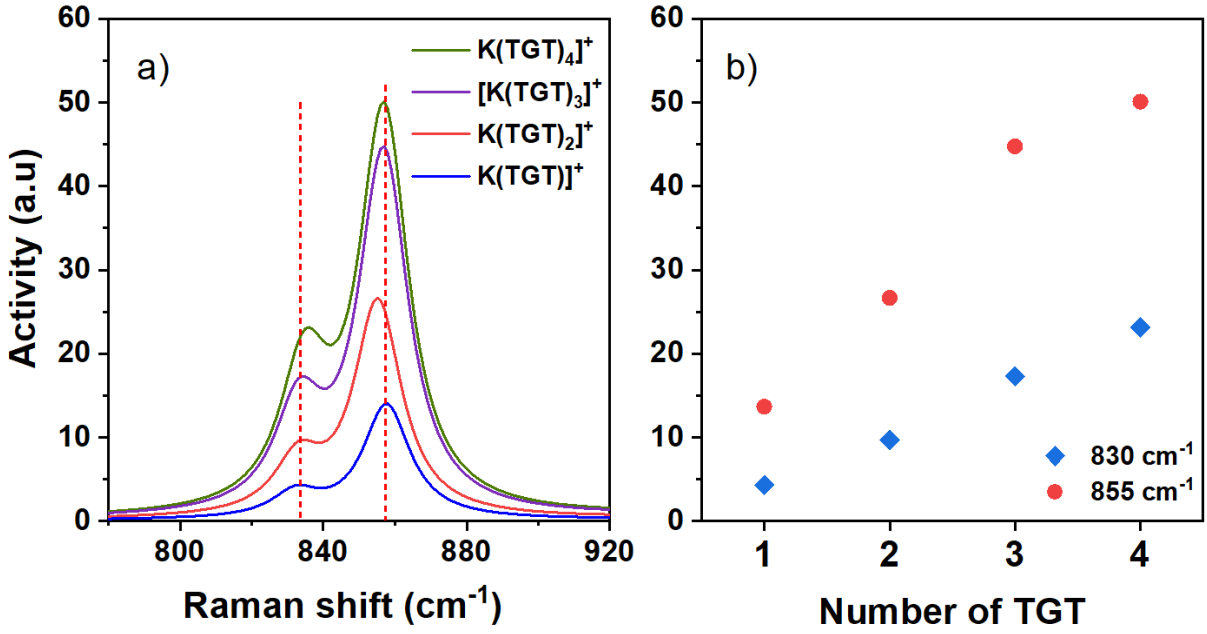

Figure 2.12. (a) Simulated Raman spectra of $[K(TGT)_x]^+$ complexes constructed in GaussSum and (b) activities of the vibrations as function of the number of coordinated DME in TGT conformation.

From the above, a statistical combination of DFT calculated data and experimental spectroscopy data was applied to calculate the SN; the intensity of each peak in the region 780–1045 cm^{-1} was calculated by the equation:

$$I_{peak} = m \times \sum n_i \times a_i \quad (2)$$

where, I_{peak} is the fitted peak intensity, n_i and a_i are the populations and computed Raman activities of conformer *i*, and *m* is an adjusting factor, on average $4.6\ 10^{-4} \pm 2.4\ 10^{-4}$ (cf. Table S3). Since the intensity of the peak at 855 cm^{-1} is a linear function of the salt molar fraction, this can be obtained as:

$$\begin{aligned} I_{855} &= \left(a_{855} \times n_{tgt-b}\right) \times m + k \\ &= \left(a_{855} \times SN_{tgt} \times m\right) \times n_{KFSI} + k \end{aligned} \quad (3)$$

where n_{tgt-b} is the molar fraction of bound TGT, n_{KFSI} is the molar fraction of KFSI; a_{855} is the calculated Raman activity of the $[K(TGT)]^+$ complex, and *k* is the intercept. The SN, deduced from the slope (Figure 2.13) is **2.7**, which is equivalent to the formation of approximately 30% $[K(TGT)_2]^+$ and 70% $[K(TGT)_3]^+$. This agrees very well with the binding

energies, were the addition of the third TGT lowers the energy the most. In the HC region, the SN is strongly reduced; for DME:KFSI = 2 and 1.5 the SNs is 1.9 and 1.4, respectively.

The evolution of the SNs as a function of salt concentration also provides a convincing explanation for the mixed mechanism of graphite using the 3.0 M electrolyte. As this electrolyte stays in the LC region, the K^+ ions are surrounded by 2 or 3 solvent molecules, which leads to the co-intercalation at the beginning of the discharge process. Consequently, the salt-to-solvent molar ratio in the bulk rises, and the concentration of the electrolyte becomes higher. As a result, the SN of K^+ reduces, and the intercalation takes place at low potentials.

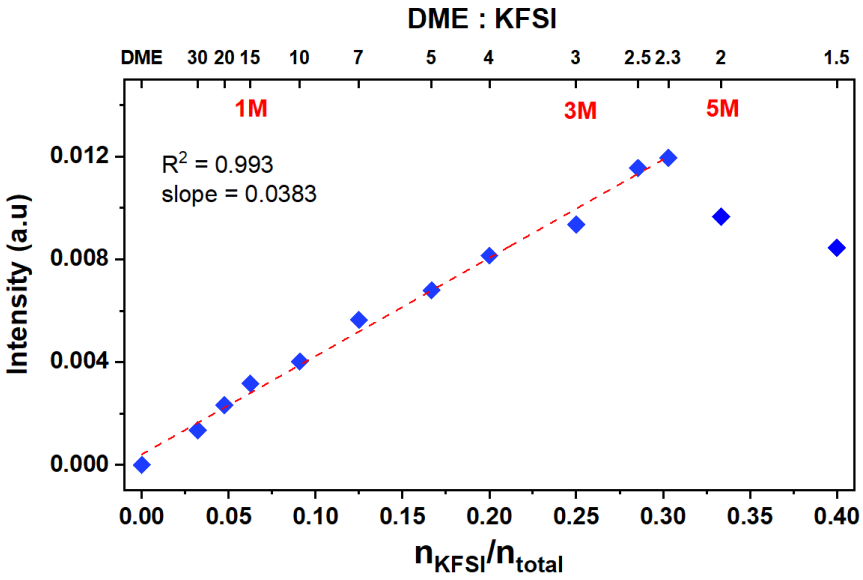

Figure 2.13. Evolution of the 855 cm^{-1} deconvoluted peak as a function of the salt molar fraction.

2.3.3. Origin of (co)intercalation/intercalation and insight into the storage mechanism

From the literature, extremely thin SEI films are expected for glyme-based electrolytes in alkali-metal systems, why co-intercalation of K^+-DME complexes would be expected to be independent of the electrolyte salt concentration. Differences in the storage mechanism, however, from co-intercalation to intercalation with increasing KFSI concentration could depend upon specific properties of the SEI, and a stable and uniform SEI with a high content of inorganic components is expected to be formed in HCEs [174].

To better understand whether the change in storage mechanism depends on the specific nature of the SEI formed or on the properties of the electrolytes themselves, two additional tests were performed: *i)* a graphite electrode underwent a full discharge/charge (pre)cycling *vs.* K with the 5.0 M KFSI in DME electrolyte and then mounted and cycled in a new cell with the 1.0 M KFSI in DME electrolyte, and *ii)* a second cell prepared *vice-versa* (Figure 2.14).

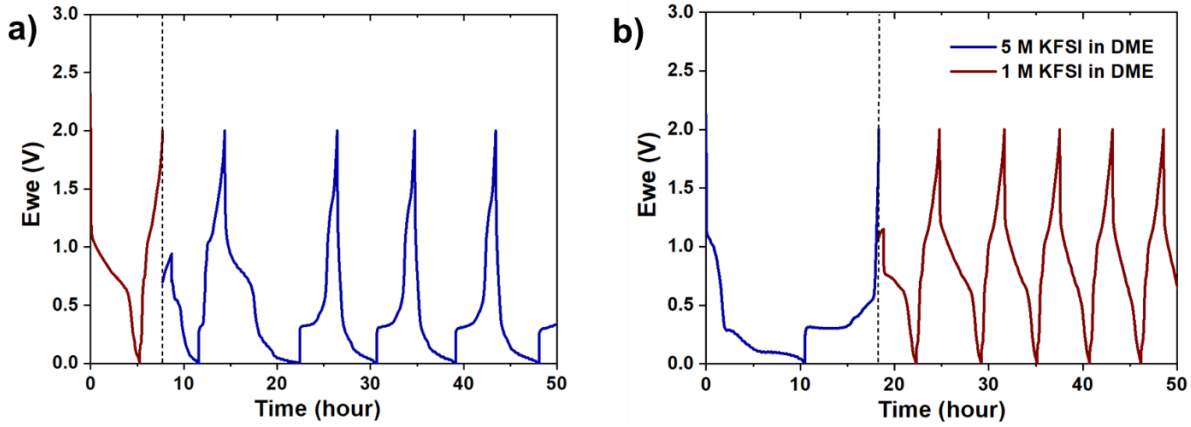

Figure 2.14. Changes in storage mechanism as observed by cycling pre-cycled cells with different KFSI in DME electrolytes: (a) from 1.0 to 5.0 M and (b) from 5.0 to 1.0 M.

For the cell pre-cycled with the 1.0 M electrolyte, there is a gradual disappearance of co-intercalation in favor of intercalation with the fresh 5.0 M electrolyte. Almost the same easy change in mechanism, but in the reverse direction, when moving from the 5.0 to the 1.0 M electrolyte, indicates that the different SEIs most probably are not responsible for the changed mechanism. If a stable SEI were formed in the first experiment, co-intercalation would not be observed immediately, but more intriguing is that in the second cell co-intercalation seems to be retained for one additional cycle. This can be explained by considering that either the SEI formed is more stable, taking some time to dissolve and thereafter form a new SEI, or most probably, some trace of co-intercalation is retained by graphite, possibly involving the SEI formed. Indeed, previous works on Na-based systems [44,175] clearly indicates that even when it has been completely desodiated, graphite still shows some volume expansion as compared to its pristine state, probably due to the presence of some solvent molecules trapped in the interlayer spacing. In the same direction goes the study of Aurbach and co-workers, which showed by NMR spectroscopy that about 25 % of diglyme is retained inside graphite after desodiation.[176] Therefore, even if additional investigations are needed to completely understand both the composition and importance of the SEI on the long-term cycling performance of graphite in these PIBs, the SEI does not seem directly responsible for the observed storage mechanism(s).

This means that we now can turn our eye to the K^+ solvation and speciation, and from the above intercalation/co-intercalation can be described by this general reaction:

$$C_n + K^+ + e^- + v\ DME \rightarrow C_n^-(DME)_vK^+ \quad (4)$$

In a typical PIB full cell working with intercalation in both electrodes, the average concentration of K^+ in the electrolyte is constant. In the case of co-intercalation, however, there will be a net increase in the average K^+ concentration, since the solvent (concentration) outside the electrodes decreases. In a typical coin-cell, with a hundred microliters of electrolyte and a few milligrams of graphite electrode, this solvent depletion becomes significant, especially for HCEs. This would result in a further decrease in the SN and is a reasonable explanation for the changed storage mechanism.

A support for this proposal is the mixed mechanism observed for the intermediate 3.0 M electrolyte; being at the border between the LC and HC regions, the co-intercalation observed initially leads to reduced DME available in the electrolyte, and the mechanism is converted to intercalation.

From a thermodynamic point-of-view, the potential differences between intercalation and co-intercalation processes can be studied. As the K^+ first solvation shell is either completely removed or not before the very entering into graphite, the energy difference should be related to the desolvation energy of the intercalated $[K(TGT)_x]^+$ complex. Based on the *operando* XRD patterns (Figure 2), the starting potentials are 0.33 and 0.86 V, respectively, *i.e.*, $\Delta E = 0.53$ V, and the corresponding difference in Gibbs free energy (ΔG) estimated from:

$$\Delta G = nF\Delta E \qquad (5)$$

where n is the number of electrons transferred. The ΔG obtained is of the order of 50 kJ/mol, which indeed is of the order of the binding energy of one TGT to K^+. This means that a reduction of the SN of K^+ in DME by ca. one unit, occurring in the case of co-intercalation, could be disfavoured, in terms of energy, with respect to a change in the storage mechanism to intercalation.

To probe further the interactions and provide plausible configurations inside the interlayer spacing, MC simulations were performed starting from a composition of $K(DME)_xC_{11}$, as extrapolated from the 1M-to-5M discharge capacity ratio of graphite in the second cycle (Fig 1a). The density of DME and K^+ inside the interlayer spacing and the distances show saturation for a ratio DME:K^+ of 1.35:1 (Figure 2.15). The K^+ cations seem to be strongly interacting with the graphene layers and the presence of DME does not change this, as previously observed for Na^+-saturated graphite in interaction with DME [144] as well as for other alkali cations [32]. All distances are between 2.5 and 2.7 Å, in agreement with the DFT results.

The impact of confinement on the DME molecules in the interlayer spacing was studied by the adsorption enthalpy. K^+ in the presence of 1 DME molecule, without any graphene

layers, results in 76 kJ.mol^{-1}, in general agreement with previous DFT calculations for Na^+ [177], but slightly higher as no solvent is taken into account here. In contrast, the adsorption enthalpy is 110 kJ.mol^{-1} showing the strong effect of the confinement.

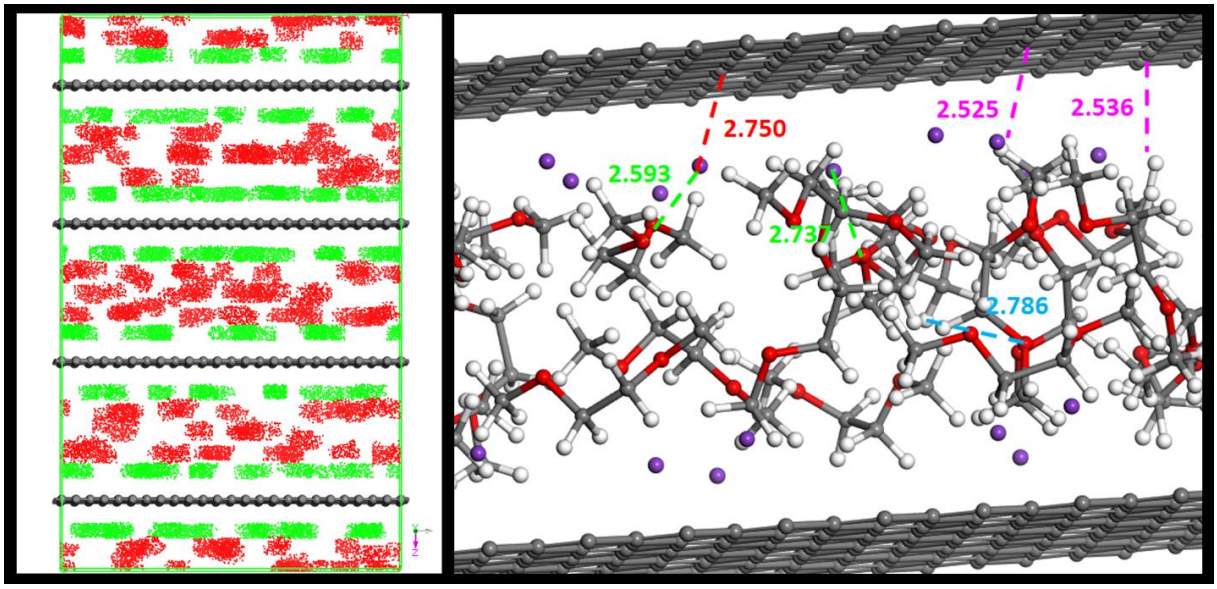

Figure 2.15. Density of presence (red points correspond to DME and green points to K^+ respectively) (a) and snapshots of the main distances in the $K(DME)_xC_{11}$ structure in presence of DME at saturation obtained from Monte Carlo simulations. The distances reported in red, green, cyan and pink correspond to the distances between cations and layers, DME and cations, DME molecules, and DME and layers respectively.

2.4. Summary

The electrochemical storage mechanisms of K^+ in graphite using KFSI:DME electrolytes of high and low salt concentrations have been unambiguously distinguished by using *operando* XRD. The cation solvation was identified to be the key factor determining the storage mechanism, as the SEIs formed were found to be unable to block co-intercalation regardless of the electrolyte salt concentration. The binding energies of $[K(DME)_x]^+$ complexes revealed the selectivity in conformational solvation as well as confirmed that the highest SN by DME is 4, corresponding to a maximum CN = 8. Yet, SNs of 2 and 3 by DME are dominant for the less concentrated electrolytes, leading to difficult desolvation, where co-intercalation occurs. At higher salt concentrations, with SNs ≤ 2, intercalation becomes energetically favored and this renders the HCEs the superior alternative, both in terms of thermodynamics and kinetics, for graphite-based anodes in PIBs. The strong influence of the electrolyte salt concentration on the charge storage mechanism of K^+ in graphite paves the way for better design of electrolytes for the emerging field of PIBs.

Supplementary information

Operando XRD

The application of Bragg's law using eqs. (S1) and (S2) allows us to determine *l* from eq. (S3):

$$n\,\lambda = 2d\,\sin\theta \qquad \text{(S1)}$$

$$d_{(00l)} = \frac{c}{l} \quad \text{and} \quad d_{(00l+1)} = \frac{c}{l+1} \qquad \text{(S2)}$$

$$l = \frac{1}{\frac{\sin\theta_{(00l+1)}}{\sin\theta_{(00l)}} - 1} \qquad \text{(S3)}$$

where d_{00l} and d_{00l+1} are the *d* spacings of the (00*l*) and (00l+1) planes, respectively, and *c* is the lattice parameter.

The staging process can thus be followed using *operando* XRD by monitoring the evolution of the (00*l*) and (00l+1) spacing, which, for pure intercalation and pure co-intercalation (1 M KFSI in DME electrolyte), evolve in the following way:

- *Intercalation (5 M KFSI in DME electrolyte)*

  A first plateau is found at high potential, where the (002) reflection of graphite remains unchanged and corresponds to decomposition of the electrolyte and formation of a solid electrolyte interphase (SEI). At a potential below 0.25 V, the intensity of the (002) peak starts to decrease, and two new features appear at both its sides and gradually move to lower and higher angles, respectively, corresponding to the formation of a dilute staging phase. Three sequential biphasic staging regimes occur starting from potentials below 0.2 V, with the formation of stages III, II and I ($d_{(00l+1)}$ = 4.01, 4.34 and 5.34 Å, respectively), which can be attributed, in agreement with the literature,[39,40] to the following staging sequence:

  KC_{36} (*Stage* III) → KC_{24} (*Stage* II) → KC_8 (*Stage* I)

  The staging sequence is reversed during the subsequent charge.

- *Co-intercalation (1 M KFSI in DME electrolyte)*

After the very first part of the discharge, where the XRD pattern of graphite does not change and thus is attributed to the SEI-formation, the (002) reflection decreases in intensity and two additional peaks appear on its sides and progressively shift away from it, corresponding to a dilute staging process. These peaks reach their maximum intensities at 26.79° and 33.97° at a potential of 0.7 V and can be indexed as (004) and (005) reflections of Stage II co-intercalated graphite. This is followed by a biphasic staging process with 3 new peaks at 17.06°,

25.72° and 34.11°, corresponding to $l = 2$. These peaks move slightly to higher angles during the potassiation and eventually return to their initial positions at the end of the discharge, testifying a rearrangement of the co-intercalated K^+-DME species within the interlayer spacing. This sequence, which is completely reversed during the subsequent charge, fully agrees with the literature.[39,40,137,163]

CHAPTER 3.
ELECTROCHEMICAL MECHANISMS OF PRUSSIAN BLUE ANALOGUES IN POTASSIUM-ION BATTERIES

Given their outstanding cycling performance, PBAs whose chemistries are based on Fe and Mn as redox active centres have been intensively studied as cathodes for SIBs and PIBs.[94–97,178–182] Their electrochemical properties are strongly correlated with the compositions and structural evolution during cycling. During K^+ extraction/insertion, PBAs in general undergo multiple phase transitions with concomitant volume expansion/contraction, phenomena which are commonly more severe for MnFe-based PBA owing to the onset of the Jahn-Teller effect when Mn^{3+} is formed during charge.[95,183] Therefore, one possible way to mitigate this is by partial replacement for Mn by Fe.[98]

In this work, a PBA with chemical formula $K_{1.7}Mn_{2/3}Fe_{1/3}[Fe(CN)_6]$ (MF21) is employed as cathode for PIBs using 5.0 M KTFSI in DME as the electrolyte. In PIB half-cells, MF21 exhibits a similar galvanostatic profiles as those reported by Jiang *et al.*[98] and offers a high initial discharge capacity of 134 $mAh \cdot g^{-1}$ with a CE of 93 %. However, gradual capacity degradation and moderate rate capability raise questions about the relation between the intrinsic chemistry and the electrochemical behaviour of MF21.

The electrochemical mechanism of MF21 is therefore studied by complementary *operando* techniques and *ex situ* Mössbauer spectroscopy. Mössbauer spectroscopy serves to identify the redox reactions of the Fe species. From this, the redox reactions during the potassiation are deduced to happen in the order LS Fe^{3+}/LS Fe^{2+} > HS Mn^{3+}/HS Mn^{2+} > HS Fe^{3+}/HS Fe^{2+}. Furthermore, chemometric analysis of the *operando* data allows us to follow the physico-chemical and structural evolution during electrochemical cycling, to provide a deeper understanding. *Operando* XRD shows a reversible transformation from a monoclinic phase to a cubic phase, followed by a volume expansion of the cubic phase during the depotassiation, and *vice versa*. *Operando* XAS recorded during the first depotassiation shows simultaneous oxidation of Mn^{2+} and LS Fe^{2+}. EXAFS analysis reveals the modification of the local geometry around both Fe and Mn and confirms that the Jahn-Teller effect causes the distortion of the local structure of Mn, which is associated with the lattice expansion in all dimensions happening during the depotassiation. These results will pave the way to optimize the chemical compositions of PBAs in order to alleviate severe structural modifications which might cause battery failure.

The synthesis, the electrochemical tests, the characterizations of the pristine material, the *ex situ* Mössbauer spectroscopy, and the *operando* XRD were all conducted at ICGM, while the *operando* XAS was performed at the XAFS beamline at Elettra Synchrotron in Trieste, Italy with the technical help of Dr. Giuliana Aquilanti.

Prussian Blue Analogues for Potassium-ion Batteries: Insights on the Electrochemical Mechanisms

Phuong Nam Le Pham[1,2], Romain Wernert[1,3,4], Maelle Cahu[1], Moulay Tahar Sougrati[1,2,4], Giuliana Aquilanti[5], Patrik Johansson[2,6], Laure Monconduit[1,2,4], Lorenzo Stievano[1,2,4]

1- ICGM, Univ. Montpellier, CNRS, Montpellier, France

2- Alistore-ERI, CNRS, Amiens, France

3- ICMCB, Bordeaux, CNRS, Bordeaux, France

4- RS2E, CNRS, Amiens, France

5- Elettra-Sincrotrone Trieste, Trieste, Italy

6- Department of Physics, Chalmers University of Technology, Göteborg, Sweden

(Submitted on Journal of Materials Chemistry A)

Abstract

A comprehensive description of the electrochemical mechanisms of the Prussian blue analogue (PBA) $K_{1.67}Mn_{0.65}Fe_{0.35}[Fe(CN)_6]_{0.92}\cdot 0.45H_2O$ is obtained by combining several complementary *ex situ* and *operando* physico-chemical characterisation techniques. This particular PBA, which shows very good electrochemical performance as a cathode material in potassium-ion batteries (PIBs), undergoes three successive redox reactions during the (de-)potassiation that are hereby identified by *ex situ* ^{57}Fe Mössbauer spectroscopy and *operando* Mn and Fe K-edge X-ray absorption spectroscopy. These reactions come along with notable modifications of the crystal structure, which are followed in real time by *operando* X-ray diffraction. The correlation of these results, interpreted with the support of chemometric methods, also reveals the weaknesses of this PBA, probably related to the deactivation of the Mn undergoing extensive reversible Jahn-Teller distortion during cycling as well as possible dissolution in the electrolyte. Combined this underlines that optimisation of the chemical composition of PBAs is a crucial step towards the preparation of reliable and stable PBA-based cathodes for PIBs

3.1. Introduction

Rechargeable batteries represent one of energy storage systems of choice in the on-going energy transition. Lithium-ion batteries (LIBs) have been playing an important role in supplying power to different systems, from portable devices to electric vehicles.[184] Their dependence on non-eco-friendly elements such as Ni or Co, however, and the inadequacy of Li resources may limit their penetration in the energy market for some applications.[185] In the last decade, research on new battery technologies has increased rapidly, in order to find suitable alternatives to LIBs. Amongst the next-generation batteries (NGBs) technologies proposed up to now, potassium-ion batteries (PIBs) are considered as promising candidates for large-scale energy storage. Beside the widespread availability of the raw materials, PIBs possess attractive merits such as fast ionic diffusion kinetics of K^+ ions in the electrolyte, comparable energy density to LIBs, and a large choice of potential electrode materials.[186]

As compared to other cathode materials for PIBs, Prussian blue analogues (PBAs) have gained great interests due to their cost effectiveness, facile synthesis and excellent electrochemical properties.[187–193] PBAs have a general chemical formula of $A_xM1[M2(CN)_6]_y$ ($x \leq 2$), in which A is an alkali cation, M1 and M2 are high spin (HS) and low spin (LS) transition metals (TMs), respectively. The TMs located in $M1N_6$ or $M2C_6$ octahedra are linked via the cyanides, forming a three-dimensional cage-like structure with open channels, which facilitates the insertion of various guest cations.[194] Among them, K^+ is known to have a relatively high affinity to the PBA framework.[195–198] The redox mechanism of PBAs resides in the redox couples of both TMs, and it is strongly dependent on the composition as well as on the battery chemistry.[199,200] In some cases, only one of the two metals is redox active, which negatively affects the overall capacity of the material. To this regard, manganese (Mn) and iron (Fe) are commonly chosen TMs for PBAs, because they are both low-cost non-toxic elements and, are redox active, thereby leading to high practical capacities, close to 150 mAh g^{-1}.[201–203] The promising electrochemical properties of Mn and Fe based PBAs have been reported for both aqueous and organic sodium-ion batteries (SIBs)[199,200,204–209] and PIBs[190,210–215]. Nevertheless, the order of the redox reactions at the two Mn and Fe sites is still a matter of debate: on the one hand, by comparing the signals of the TMs in the cyclic voltammetry (CV) signatures of different PBA compositions, the redox potentials of the TMs were found in the order of HS Fe^{3+}/HS Fe^{2+} < LS Fe^{3+}/LS Fe^{2+} < HS Mn^{3+}/HS Mn^{2+}.[214–217] On the other hand, from soft X-ray absorption spectroscopy (sXAS), Pasta and co-workers proposed that the oxidation of LS Fe^{2+} and HS Mn^{2+} occurs simultaneously, yet the LS Fe^{3+}/LS Fe^{2+} couple was

assigned at lower potential.[218] The sXAS spectra at the Mn L-edge showed insignificant modifications during the anodic scan, which made the assessment difficult and ambiguous. In addition to these uncertainties, the structural evolution of these materials needs to be studied more thoroughly. In fact, *operando* X-ray diffraction (XRD) showed that such PBAs undergo several reversible phase transitions and volume expansion/shrinkage during the K^+ (de)insertion, which is mainly related to the Jahn-Teller (JT) effect at the Mn^{3+} centres.[214] Such structural evolution, however, might be triggered by both, the variation of oxidation states of the TMs (and in particular for Mn) as well as by the simultaneous (de)insertion of the cations within the cage structure, both phenomena contributing to the modification of electronic properties and local structures. As the electrochemical properties of electrode materials have a strong correlation with their structural evolution, which affects their battery performance in terms of reversibility and cyclability, it is necessary to have a clearer view of these phenomena in manganese hexacyanoferrate PBAs.

In this work, we investigate the electrochemical mechanism of a PBA with the chemical formula $K_{1.67}Mn_{0.65}Fe_{0.35}[Fe(CN)_6]_{0.92}\cdot 0.45H_2O$ as a cathode material for PIBs using complementary *ex situ* and *operando* characterization approaches. *Ex situ* ^{57}Fe Mössbauer spectroscopy provides information about the local environment of Fe centres, while *operando* X-ray diffraction (XRD) allow us to follow the evolution of the global structure of the PBA. These approaches are complemented by *operando* X-ray absorption spectroscopy (XAS), a powerful synchrotron technique that helps acquiring local information of electrode materials containing TMs. While X-ray absorption near-edge structure (XANES) provides information about the oxidation states and coordination of the TMs, the analysis of extended X-ray absorption fine structure (EXAFS) portion gives details about short-range distances of the metals.[219,220] This has already been shown to be efficient in studies of the electrochemical mechanisms of PBAs.[221–224] The analysis of the *operando* datasets was performed using a chemometric approach including principal component analysis (PCA) and multivariate curve resolution-alternating least squares (MCR-ALS) methods, allowing detailed descriptions of the structural evolution and local environment of the TMs.[225] These complementary findings are combined to understand in detail the influence of structural modification on the electrochemical behavior of the investigated PBA.

3.2. Experimental section

3.2.1. Synthesis of the PBA

$K_{1.67}Mn_{0.65}Fe_{0.35}[Fe(CN)_6]_{0.92}\cdot 0.45H_2O$ (MF21) was synthesized by a simple co-precipitation method. Two solutions A and B were prepared at 60 °C. Solution A was obtained by dissolving 8 mmol of $K_4[Fe(CN)_6]\cdot 3H_2O$ in 100 mL of saturated KCl solution; solution B was a mixture of 5.2 mmol and 2.8 mmol of, respectively, $MnSO_4\cdot H_2O$ and $FeSO_4\cdot 7H_2O$ in 80 mL of saturated KCl solution. Solution B was poured rapidly into solution A under intense stirring. The temperature was kept at 60 °C for 24 hours of agitation. The obtained suspension was washed five times with deionized water and then two times with ethanol, and centrifuged at 20000 rpm before being dried under vacuum. An additional drying step at 100 °C overnight was applied before the characterizations and electrode formulation to ensure that the interstitial water was removed completely. The choice of drying temperature was decided based on thermogravimetric analysis results and is explained *vide infra*.

3.2.2. Materials characterization and data analysis

Powder XRD patterns of the synthetized materials were collected on a Bruker Advance D8 diffractometer with a Cu Kα radiation source (λ = 1.5418 Å) and a step size of 0.02 ° in the range of 10-100 °. Lattice parameters were obtained from profile matching method using Fullprof package.[226]

Transmission ^{57}Fe Mössbauer spectra were collected at room temperature with a triangular velocity waveform. A gas-filled counter was used for the detection of γ-rays. A 0.5 GBq ^{57}Co:Rh source, kept at room temperature, was the substrate. Velocity calibration was performed with an α-Fe foil at room temperature. Absorbers containing 5 to 25 mg cm^{-2} were protected from air using thermally sealed coffee-bags. The Mössbauer spectra were fitted by using the PC-Mos II computer program with appropriate superpositions of Lorentzian lines. In this way, hyperfine parameters such as the isomer shift (δ), the electric quadrupole splitting (Δ), the full line width at half maximum (Γ) and the relative resonance areas (Area) of the different components of the absorption patterns were determined.

Thermogravimetric analysis (TGA) was performed to determine the amount of interstitial water of MF21. The measurement was carried out on a thermic simultaneous analyzer model STA 449 F1 Jupiter® (NETZSCH) from room temperature to 450 °C under argon atmosphere with a thermal step of 5 °C/min. The amount of interstitial water was calculated based on the mass loss at 100 °C.

Transmission electron microscopy (TEM) images of the as-prepared MF21 were taken at the "Microscopie Électronique et Analytique" platform of University of Montpellier. The observations were carried out at 100 kV (LaB_6 JEOL 1400 Plus – 120 kV). Sample preparation was performed by depositing a drop of a suspension of the studied material in ultra-pure water on a copper grid. The drop was dried under air, covered from external contaminations.

Chemical composition analysis of the as-prepared MF21 was performed on a scanning electron microscope (SEM) FEI Quanta 200 Hitachi S-2600N equipped with a silicon drift detector for Energy Dispersive X-ray (EDX) analysis (Oxford Instruments X-Max 50 mm^2). The MF21 powder was deposited onto a carbon-based adhesive tape followed by an air blow to remove the excess powder. The measurement was carried out under vacuum; the quantification was performed via the INCA software with a 3 s dwell time and an acquisition time of 30 s.

X-ray absorption spectroscopy (XAS) experiments were carried out at ELETTRA Sincrotrone Trieste, Basovizza (Italy), at the XAFS beamline.[227] The storage ring was operated at 2.0 GeV in top-up mode with a typical current of 300 mA. Data were recorded at Mn and Fe K edges in transmission mode using ionization chambers filled with a mixture of Ar, N_2, and He to have 10, 70, and 95 % of absorption in the I_0, I_1, and I_2 chambers, respectively. An internal reference of Mn and Fe foils located between the I_1 and I_2 chambers was used for energy calibration at each scan. This allowed a continuous monitoring of the energy during consecutive scans. Spectra were collected with a constant k-step of 0.03 $Å^{-1}$ from 6300 to 8000 eV gathering both Mn and Fe. The energies were calibrated by assigning the first inflection point of the spectra of the Mn and Fe metal to 6539 and 7112 eV, respectively. The white beam was monochromated using a fixed exit monochromator equipped with a pair of Si(111) crystals. Harmonics were rejected by using the cut-off of the reflectivity of the platinum mirror placed at 3 mrad with respect to the beam upstream the monochromator and by detuning the second crystal of the monochromator by 30 % of the maximum. XAS spectra were analysed using the Artemis software.[228] Fourier transforms (FT) of the EXAFS data were performed in the 3–10.5 $Å^{-1}$ k range, and the fitting was done in the R-space up to 5 Å.

For the ordinary electrochemical tests, electrode films were prepared by tape-casting on aluminium foil (18 μm, GoodFellow), a slurry obtained by mixing MF21 with Super P carbon (Alfa Aesar) and poly(vinylidene fluoride) (PVdF, Solef® 5130) as conductive additive and binder, respectively, with a mass ratio of 60/30/10 in N-methyl-2-pyrrolidone (NMP, Sigma Aldrich) in a planetary ball mill. The casted film was dried in air before punching out round-

shape electrodes with the diameter of 1.27 cm, which were then further dried under vacuum at 80 ℃ overnight. Coin cells (CR2032) of MF21 and K metal were assembled in an Ar-filled glovebox (O_2 < 0.5 ppm, H_2O < 0.5 ppm) using 5 M KTFSI in DME as the electrolyte, a Whatman glass fibre and a tri-layer polypropylene polyethylene membrane (Celgard 2325) as separators.

Galvanostatic cycling was carried out at the current density of 25 mA g^{-1} for normal cycling tests, and from 15 to 500 mA g^{-1} for the rate capability test. The galvanostatic intermittent titration technique (GITT) was applied using a current rate of 5 mA g^{-1} with an acquisition time of 30 minutes, followed by a 3-hour relaxation, with dE_{WE}/dt = 0.1 mV h^{-1}. The diffusion coefficient at each *x* value (*x*: the amount of inserted K^+ at each pulse) was calculated as:

$$D = \frac{4}{\pi\tau}\left(\frac{n_m V_m}{S}\right)^2\left(\frac{\Delta E_s}{\Delta E_t}\right)^2 \quad (cm^2\ s^{-1})$$

Here, τ (s) is the duration of the current pulse; n_m (*mol*) is the number of moles; V_m ($cm^3\ mol^{-1}$) is the molar volume of MF21; *S* (cm^2) is the electrode area (1.27 cm^2); ΔE_s (*V*) is the steady-state voltage change, due to the current pulse, and ΔE_t (*V*) is the voltage change during the constant current pulse, eliminating the *iR* drop.

For the *ex situ* and *operando* analyses, the electrodes were prepared by thoroughly mixing MF21 with Super P carbon and PTFE (poly(tetrafluoroethylene)) at a weight ratio of 60/30/10 to form a homogeneous film. The film was cut into round electrodes with the diameter of 11 mm (*operando* XRD and XAS) or 14 mm (*ex situ* Mössbauer spectroscopy). *Operando* XRD and XAS experiments were carried out using a special electrochemical cell equipped with a Be window.[229] A thin Al foil (thickness = 2 μm) was put between the working electrode and the Be window and used as the positive current collector. The mass loading of the electrodes used for the *ex situ* Mössbauer spectroscopy was *ca.* 25 mg cm^{-2}, whereas it was ≤ 10 mg cm^{-2} for the *operando* XRD and *operando* XAS measurements. A common chemometric approach based on principal component analysis (PCA) and multivariate curve resolution-alternating least squares (MCR-ALS) analysis, described in detail elsewhere,[225] was applied to analyse the full *operando* XRD patterns and XAS spectra datasets. In short, PCA is used here to determine the number of independent components contributing to the whole series of collected patterns/spectra during electrochemical cycling. The number of principal components determined in this way is the used as the basis for MCR-ALS analysis, which allows the stepwise reconstruction of the "pure" spectral components which are necessary for interpreting

the whole multiset of *operando* spectra. The MCR- ALS analysis was performed with the following constraints: (i) non-negativity of the intensity of the components, (ii) unimodality for the evolution of all components along a single process and (iii) closure (the sum of all components always equal to 100 of the intensity). The pure XRD and XAS components obtained from MCR-ALS analysis are then analyzed as normal XRD patterns and XAS spectra, respectively.

3.3. Results and discussion

3.3.1. Structure, composition, and morphology of the as-prepared MF21

The XRD pattern of dried MF21 and the corresponding profile matching are shown in Figure 3.1a. The unit cell can be indexed as monoclinic structure (space group $P2_1/n$) with *a*, *b*, *c*, and β equal to 10.009(2) Å, 7.228(1) Å, 6.921(1) Å, and 90.38(1) °, respectively. The crystal lattice of the MF21 is slightly smaller and more tilted than other reported isostructural PBAs containing Mn and/ or Fe as HS TMs,[214,230,231] probably due to the formation, during the synthesis and/or the drying processes, of small portions of oxidized Mn^{3+} or Fe^{3+} at the M1 site. The TEM image in the inset of Figure 1a shows that MF21 consists of nanoparticles with sizes between 30 and 50 nm with a uniform cubic morphology. EDX and TGA analyses allow establishing the chemical formula $K_{1.67}Mn_{0.65}Fe_{0.35}[Fe(CN)_6]_{0.92}\cdot 0.45H_2O$ for the dried MF21 (Figure 3.2 and Table 3.2) by considering only divalent M1 sites. Besides, as observed in the TGA curve of MF21 (Figure 3.2b), when increasing the temperature, the mass of MF21 keeps being lost until 200 °C. However, it was reported that drying PBA at 200 °C for a long duration can cause structural damage.[232] In order to choose an appropriate drying temperature, we compared the color and the crystallinity of MF21 after the vacuum drying at 100 °C and 200 °C (Figure 3.3). When drying at 100 °C, MF21 maintained its deep green color and monoclinic structure. In contrast, after one night being dried at 200 °C, the material turned black and the main peaks corresponding to the monoclinic phase diminished, indicating a severe loss in the crystallinity. Therefore, we decided to dry MF21 at 100 °C, which is enough to remove the interstitial water as well as to retain the material structure.

The room temperature ^{57}Fe Mössbauer spectrum of dried MF21 (Figure 3.1b) can be fitted with a singlet and two quadrupole split doublets. The corresponding hyperfine parameters (Table 3.1) provide information about oxidation states, compositions, and local geometries of the Fe centers: the isomer shift (δ = -0.10 mm s^{-1}) of the singlet, counting for 70 % of the global spectral area, can be attributed to LS Fe^{2+}. The lack of quadrupole splitting (Δ = 0.00 mm s^{-1})

indicates that the Fe^{2+} centers are surrounded by a centrosymmetric electron distribution, as expected for a LS d^6 electron configuration and a symmetric octahedral coordination.[233] The doublet with the highest isomer shift (δ = 1.02 mm s^{-1}) can be attributed to HS Fe^{2+}. The larger values of quadrupoles splitting (Δ = 1.50 mm s^{-1}) for this component compared to other Na-based pure-Fe PBAs [209] ($\Delta \sim 1.1$ mm s^{-1}) suggests a more regular octahedral coordination between HS Fe^{2+} and N atoms. The third component with intermediate isomer shift (δ = 0.28 mm s^{-1}) can be attributed to HS Fe^{3+}, indicating that about half of the HS Fe^{2+} was oxidized during the synthesis. This oxidation seems to occur during the synthesis, since the spectra of MF21 before and after vacuum drying are virtually identical (Figure 3.4 and Table 3.3), implying that no oxidation happened during drying. The surface area of the LS Fe^{2+} is ¾ of the total spectral area, as expected from the stoichiometric ratio used for the synthesis. Balancing the oxidation of half of divalent iron ions would only requires a slight increase (about 0.04) of the hexacyanoferrate moieties with respect to the previously established formula. Thus, we will still use the $K_{1.67}Mn_{0.65}Fe_{0.35}[Fe(CN)_6]_{0.92}\cdot 0.45H_2O$ formula.

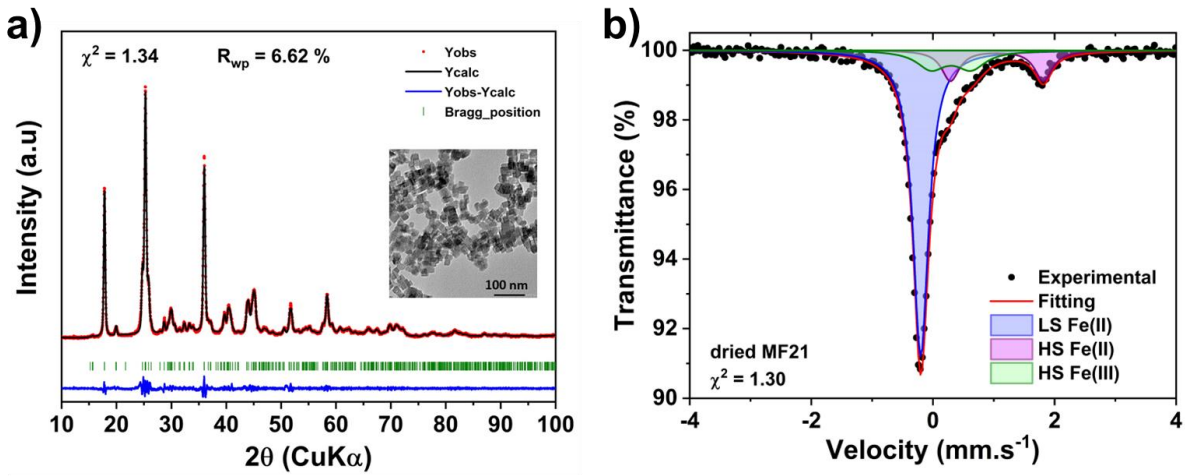

Figure 3.1. (a) XRD pattern of dried MF21 with Rietveld refinement and TEM image (inset) and (b) Mössbauer spectrum of dried MF21.

Table 3.1. Refined Room-Temperature ^{57}Fe Mössbauer Hyperfine Parameters for dried MF21, (Δ is the quadrupole splitting, δ the Isomer shift with respect to α-Fe, Γ the Lorentzian linewidth).

Δ (mm s^{-1})	**δ (mm s^{-1})**	**Γ (mm s^{-1})**	**Area (%)**	**Site**
0.00	–0.10(0)	0.31(-)	70(2)	LS Fe^{2+}
1.50(2)	1.13(1)	0.34(2)	15(1)	HS Fe^{2+}
0.64(7)	0.39(5)	0.46(8)	15(2)	HS Fe^{3+}

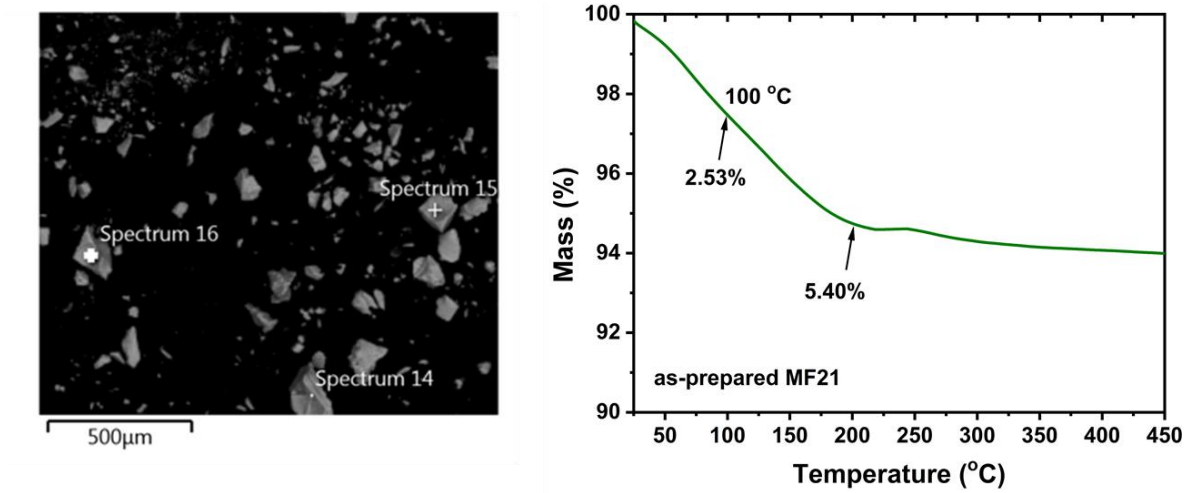

Figure 3.2. SEM-EDX image (left) and TGA curve (right) of the as-prepared MF21. The amount of removed water from the vacuum drying step is calculated from the mass loss at 100 °C.

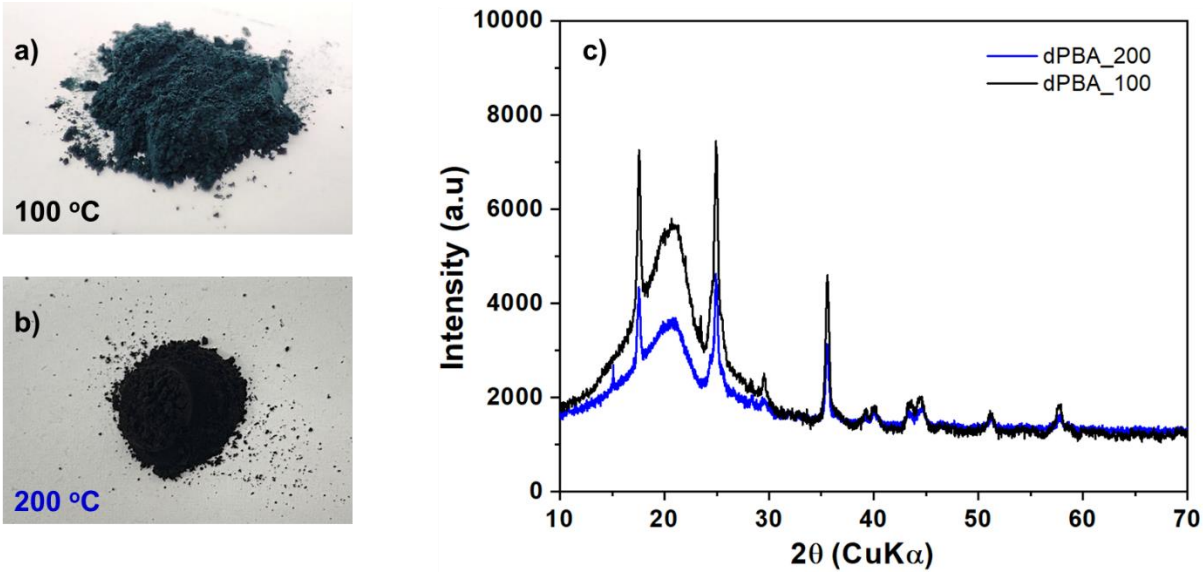

Figure 3.3. PBA powders after the vacuum drying at 100 °C (a) and 200 °C (b) and their X-ray diffractograms (c).

Table 3.2. Elemental analysis of K, Mn, and Fe obtained from SEM-EDX.

Element	K	Mn	Fe
Atomic percentage (%)	46.60	18.24	35.16

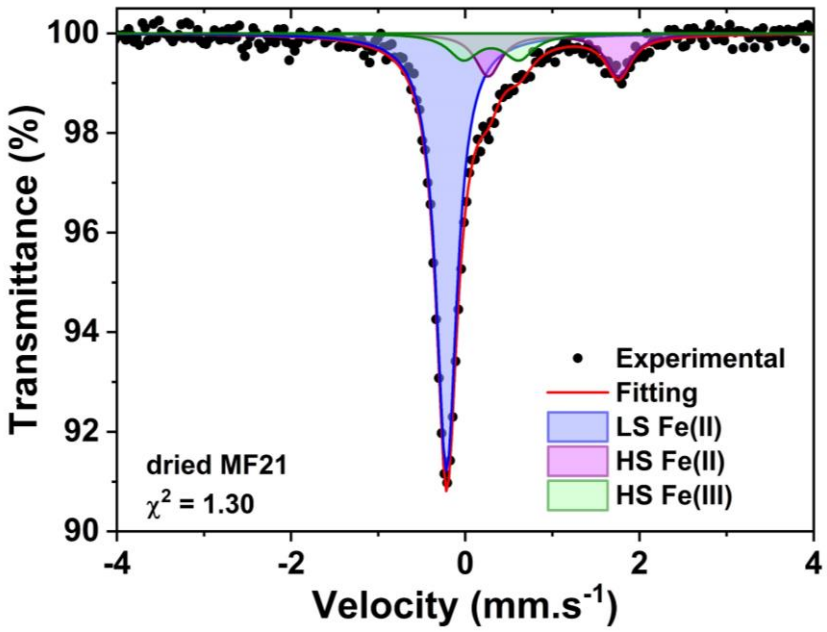

Figure 3.4. Room-temperature Mössbauer spectrum of pristine MF21.

Table 3.3. Refined Room-Temperature ^{57}Fe Mössbauer Hyperfine Parameters for pristine MF21.

Δ (mm s^{-1})	δ (mm s^{-1})	Γ (mm s^{-1})	Area (%)	Site
0.00(-)	-0.10(0)	0.29(-)	71(-)	LS Fe^{2+}
1.49(2)	1.01(1)	0.36(2)	17(1)	HS Fe^{2+}
0.64(6)	0.30(5)	0.41(8)	12(2)	HS Fe^{3+}

3.3.2. Electrochemical performance of MF21 in PIB half-cells

The electrochemical performance of MF21 in PIB half-cells in long-term galvanostatic cycling at various current densities is shown in Figure 3.5. The galvanostatic profile of MF21 half-cell contains at least two plateaus in each charge/discharge process (Figure 3.5a, c). During discharge, two medium-length plateaus at *ca*. 3.8 – 4.1 V, and a short one at *ca*. 3.6 V are observed, which well correspond to the reduction of three transition-metals in the material. The short plateau remains during charge with similar capacity contribution as in the discharge, while at high potential only one plateau is observed at *ca*. 4 V. The initial discharge capacity of MF21 obtained at I = 25 mA g^{-1} is 134 mAh g^{-1} which is equivalent to the insertion of 1.7 K^+ ions with a high Coulombic efficiency (CE) of 93 % (Figure 3.5a). Despite the good performance in the first cycle, a gradual capacity degradation, with CE < 99 %, is observed during long-term cycling (Figure 3.5b). Although the 5.0 M KTFSI/DME electrolyte was reported to be stable towards K metal at high voltage[113], this electrolyte might be decomposed on the cathode to

form a cathode-electrolyte interphase, leading to poor cycling retention. As shown in Figure 3.5c-d, MF21 can deliver 104 mAh g^{-1} at the current density of 100 mA g^{-1}. While the discharge capacity decreases when increasing the current density, the CE approaches 99 %, implying less electrolyte decomposition at high potentials. Moreover, large polarizations are observed in the cycling profile at high current rates. This phenomenon as well as the capacity loss at E < 3.9 V probably result from sluggish mass transfer and deactivation of some TM sites. Since the electrochemical performance of MF21 derives from its electronic and structural properties, it is important to dwell in-depth into the mechanism and the evolution of those properties.

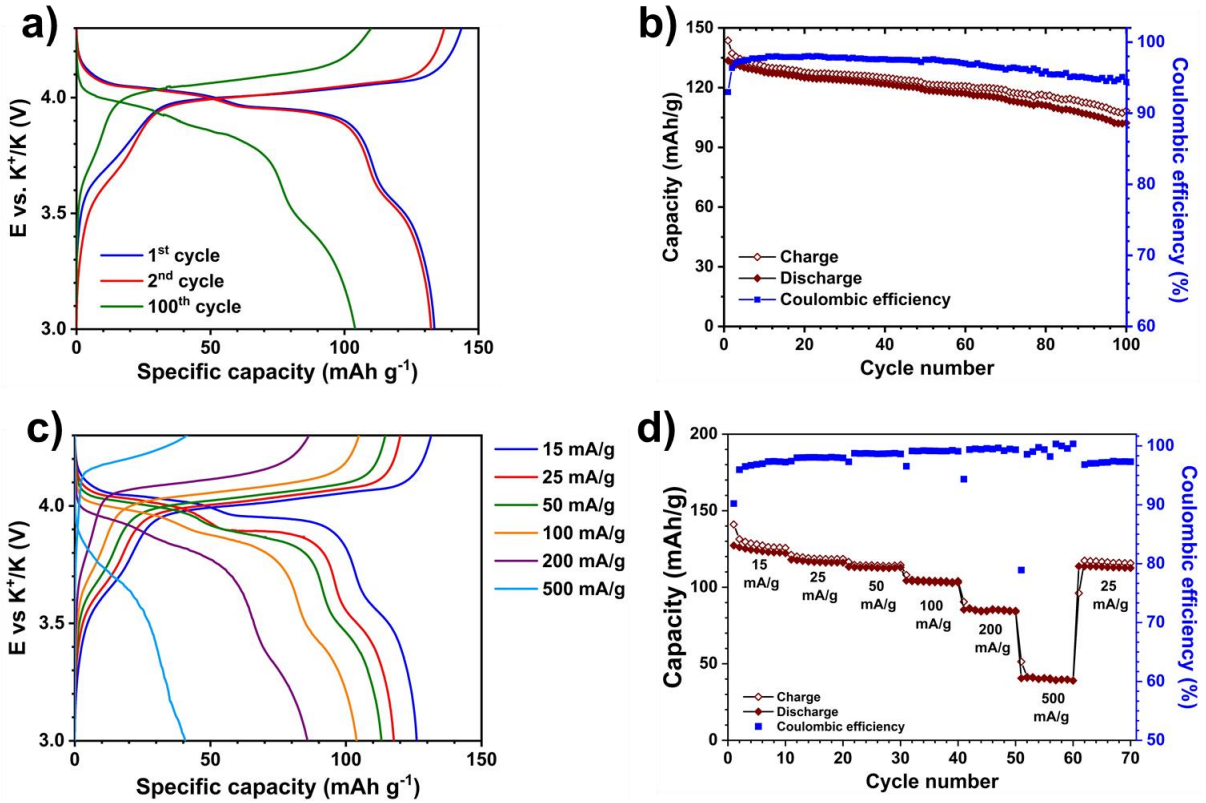

Figure 3.5. (a, b) Galvanostatic profile and cyclability of MF21 at a constant current of 25 mA g^{-1}, respectively; (c) cycling profiles and (d) rate capability of MF21 at the current varying from 15 to 500 mA g^{-1}.

3.3.3. Electrochemical mechanism of MF21

a) Ex situ ^{57}Fe Mössbauer spectroscopy

Ex situ ^{57}Fe Mössbauer spectroscopy measurements measurements were carried out at different states of charge (SOC) to determine the involvement of the Fe centres in the redox reaction(s) of MF21 occurring at each plateau (Table 3.4 and Figure 3.6). The SOC at which the Mössbauer spectra were recorded are detailed in Figure S1. At end of charge (EOC, Figure 3.6a), no contribution from HS Fe^{2+} is observed in the Mössbauer spectrum. Instead, the

percentage of the HS Fe^{3+} increases up to 31 %. The best fit for this spectrum requires an additional quadrupole doublet characterised by an isomer shift in the typical range of octahedral LS Fe^{3+} and LS Fe^{2+}. The non-zero value of the quadrupole splitting for this doublet (Δ = 0.75 mm s^{-1}), however, indicates a deviation from a centrosymmetric electron distribution, as expected for the LS d^5 electron configuration of LS Fe^{3+}. Such large values of Δ were already reported for LS Fe^{3+} in $Cu^{II}Fe^{III}$ PBAs.[234,235] Relatively large linewidths are observed for all spectral components, indicating a certain distribution of similar coordination environment for all Fe species. About 11 % of the total resonance area corresponds to LS Fe^{2+}, which accounts for 16 % of the amount of LS Fe species (70 %) according to the Mössbauer spectrum of dried MF21 (Figure 3.1b). Assuming that all the Mn^{2+} are oxidized to Mn^{3+} at the end of charge, which is equivalent to the extraction of 0.65 K^+; and based on the amount of reacted Fe^{2+} that can be calculated from the EOC Mössbauer spectrum (0.18 HS Fe^{2+} and 0.77 LS Fe^{2+}), the amount of extracted K^+ can be estimated at ~1.6 per unit formula, in good agreement with the observed capacity in oxidation.

As mentioned in the introduction (*vide supra*), the assignments in the literature of the plateaus observed in the electrochemical curves to the specific reactions of LS Fe^{3+}/LS Fe^{2+} and HS Mn^{3+}/HS Mn^{2+} were based on the comparison of CV peaks of the PBAs containing different M1 TM cations.[214–217] In particular, the first reduction (higher potential) was assigned to the reaction of Mn^{3+}/Mn^{2+}, and the second one was attributed to the redox couple LS Fe^{3+}/Fe^{2+}. However, the results of *ex situ* Mössbauer spectroscopy indicate that the opposite occurs. The spectra recorded at the end of the two high-potential plateaus in the discharge, corresponding to the cut-off voltages of 3.90 V and 3.65 V, respectively (Figure 3.6b-c) show the same compositions of LS Fe^{2+} and HS Fe^{3+}, with their area ratio is around 70/30. Therefore, the redox reactions at the two plateaus at 4.1 and 3.9 V can be assigned to the redox reaction LS $Fe^{3+} \rightarrow$ LS Fe^{2+} and $Mn^{3+} \rightarrow Mn^{2+}$, respectively. In addition to the identical area ratio of the iron species, the resolved spectra at these states of charge have a small different in the quadrupole splitting of the LS Fe^{2+}. After the second plateau, the simultaneous presence of the unequally charged Mn^{2+} and HS Fe^{3+} at the M1 sites would lead to a distortion of the local structure, resulting in a slightly distorted octahedral coordination of the LS Fe^{2+} sites, which results in small but observable quadrupole splitting (Δ = 0.14 mm s^{-1}, Table 3.4). This spectrum is identical to that obtained after the short plateau in the charge (3.80 V, Figure 3.6e), indicating that this process is well reversible and can be attribute to the redox reaction of the couple HS Fe^{3+}/Fe^{2+}. At the end of discharge (Figure 3.6d), the HS Fe^{2+} appears again in the Mössbauer

spectrum, with almost identical hyperfine parameters as the pristine material. The HS Fe^{3+} is still present in the resolved spectrum with a similar amount as before cycling, indicating that the HS Fe^{3+} formed in the synthesis is electrochemically inactive.

Table 3.4. Refined Room-Temperature ^{57}Fe Mössbauer Hyperfine Parameters for MF21 at different potentials.

Potential	**Δ (mm s^{-1})**	**δ (mm s^{-1})**	**Γ (mm s^{-1})**	**Area (%)**	**Site**
4.3 V (EOC)	0.00	-0.09	0.44(*0.13*)	11	LS Fe^{2+}
	0.35(*0.03*)	0.35	0.58(*0.05*)	31(*2*)	HS Fe^{3+}
	0.75(*0.02*)	-0.17	0.49(*0.02*)	58(*5*)	LS Fe^{3+}
3.9 V (discharge)	0.00	-0.11(*0.00*)	0.43(*0.01*)	72	LS Fe^{2+}
	0.28(*0.02*)	0.36(*0.01*)	0.43(*0.03*)	28(*1*)	HS Fe^{3+}
3.65 V (discharge)	0.14(0.00)	-0.11(0.00)	0.27(0.00)	70	LS Fe^{2+}
	0.28(0.02)	0.46(0.01)	0.55(0.03)	30(1)	HS Fe^{3+}
3 V (EOD)	0.00	-0.09(*0.00*)	0.32(*0.00*)	68	LS Fe^{2+}
	1.50(*0.04*)	1.13(*0.02*)	0.40(*0.04*)	19(*2*)	HS Fe^{2+}
	0.69(*0.07*)	0.40(*0.05*)	0.46(*0.08*)	13(*3*)	HS Fe^{3+}
3.8 V (charge)	0.12(*0.00*)	-0.10(*0.00*)	0.25(*0.01*)	72	LS Fe^{2+}
	0.26(*0.05*)	0.43(*0.02*)	0.59(*0.08*)	28(*2*)	HS Fe^{3+}

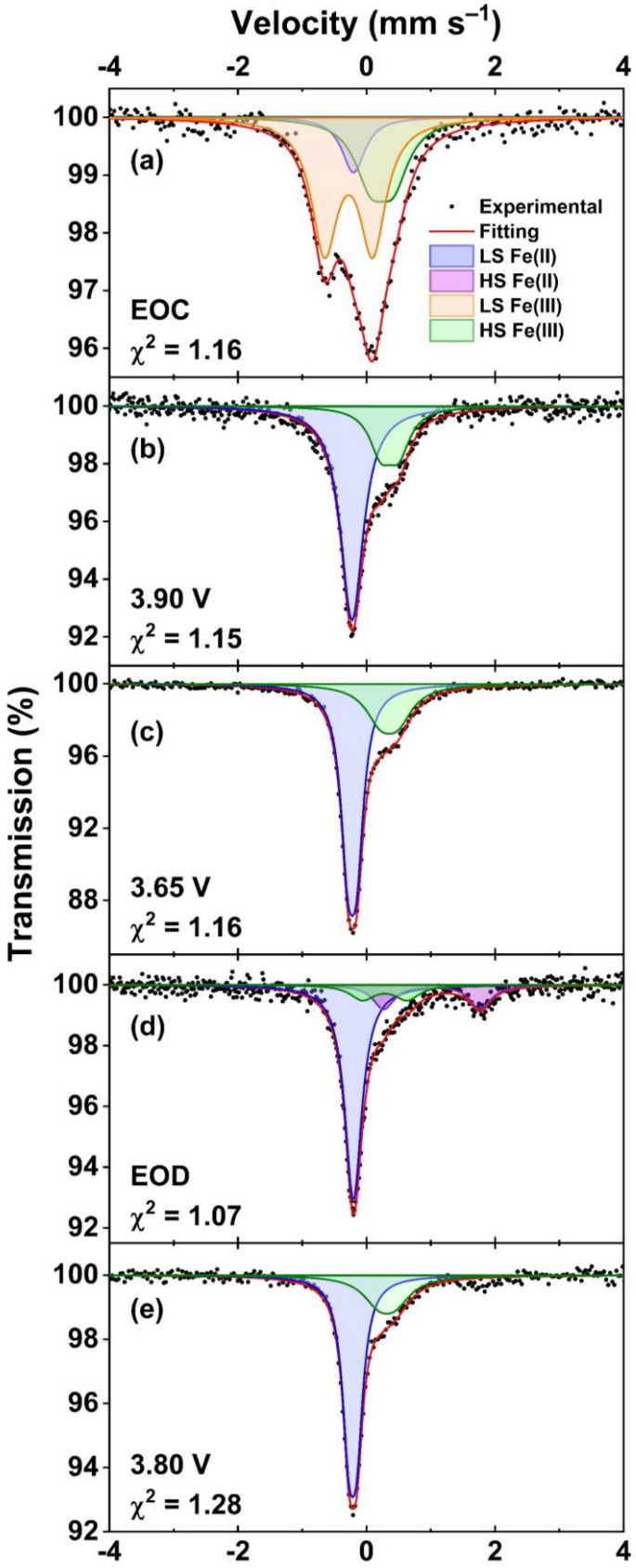

Figure 3.6. Ex situ Mössbauer spectra of MF21 recorded at different states: (a) 4.3 V – end of charge (EOC), (b) 3.90 V (end of plateau 1 in the discharge), (c) 3.65 V (end of plateau 2 in the discharge), (d) 3.0 V – end of discharge (EOD), and (e) 3.80 V (end of plateau 3 in the charge).

b) Operando XRD

The relation between the structural transformation and the redox reactions at the transition metals of MF21 can be revealed by *operando* XRD combined with chemometric analysis. The evolution of the main peaks of the diffraction patterns (Figure 3.7) show a reversible structural transformation during the first K extraction-insertion. All of them shift to lower angles during oxidation, when K^+ ions are deinserted from the host, and then return to the pristine position in the opposite process. A profile matching refinement of the *ex situ* XRD pattern of charged MF21 (Figure 3.8) shows that the oxidised PBA has a cubic structure (SG: Fm-3m) with a = 10.35179 Å.

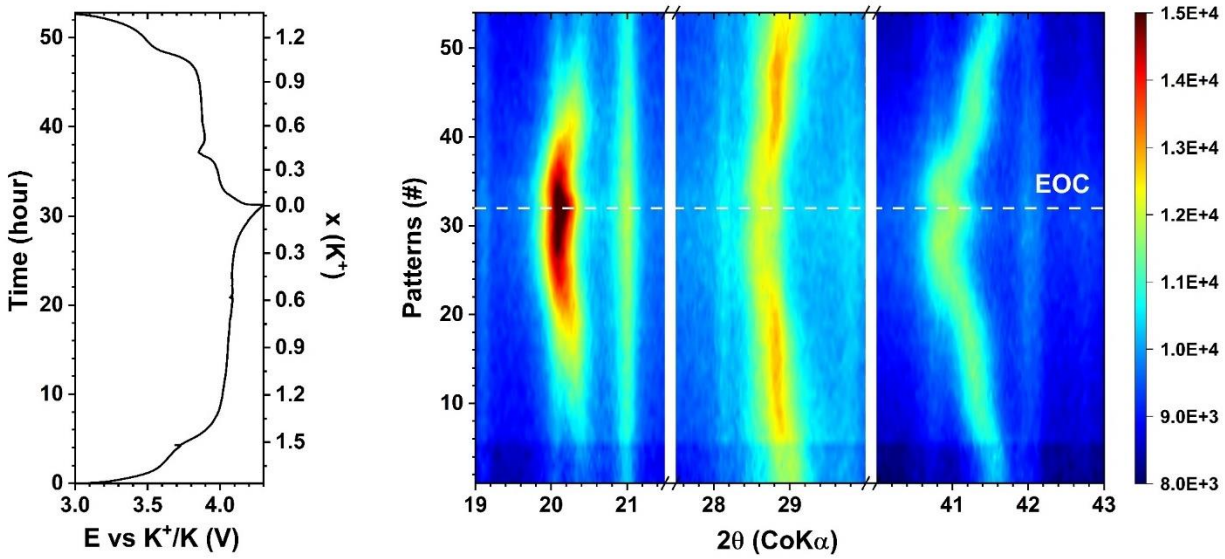

Figure 3.7. Operando XRD contour map for three selected 2θ regions of MF21 recorded at the current density of 5 mA g^{-1}, in the voltage range of 3 – 4.3 V (vs. K^+/K), and using the 5 M KTFSI in DME electrolyte.

PCA applied on the *operando* XRD data (Figure S3) shows that at least three independent components are necessary to describe the whole dataset. Therefore, MCR-ALS was employed separately on each process with the constraint of unimodality for all components. This chemometric approach allows us to follow the evolution of the three components (Figure 3.9), and concurrently, reconstructs the patterns corresponding to the three "pure" reference components (Figure 3.10), which show a shift to lower angles on going from Component 1 to 3, in line with the evolution of the *operando* data (Figure 3.7). During the (de-)potassiations, there are at least two components co-existing in the patterns (Figure 3.9). Since these components correspond to different crystal structures (*vide infra*), it implies that the electrochemical mechanism of MF21 can be described with two consecutive steps, from Component 1 to Component 2, and then from Component 2 to Component 3. Component 1

represents the pristine monoclinic phase, being the only component at the beginning of the reaction, while Component 3 corresponds to the final cubic phase, and reaches its maximum concentration at the end of charge. The intermediate Component 2 reaches its maximum at x ~ 1 (x: moles of K^+ per mole of MF21), and totally disappears at the end of charge. In the following discharge, Component 2 reappears and is maintained during the second plateau, corresponding to the reduction of Mn^{3+}, then decreases but remains at *ca.* 10 % at the end of the potassiation.

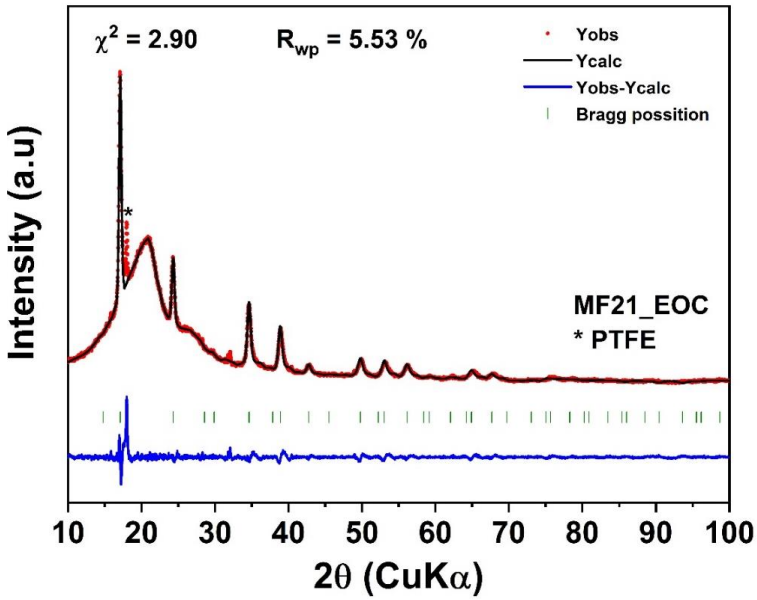

Figure 3.8. Ex situ XRD with Le Bail refinement of MF21 at the end of charge.

The profile matching refinement of the patterns of the three components (Figure 3.11) provides their space groups and lattice parameters, which are gathered in Table 3.5. Component 1 has lattice parameters virtually identical to those of the pristine phase, while those of the cubic component 3 is slightly smaller than those obtained from *ex situ* XRD. Component 2 is also cubic (SG: Fm-3m) as well, but is characterized by a smaller lattice size than that of component 3. By combining the concentration evolution of the components and their lattice parameters, the mechanism can be straightforwardly described with two processes occurring sequentially. First, a bi-phasic transformation from monoclinic MF21 to cubic $K_{1.0}$MF21 occurs during the oxidation of the HS Fe^{2+} and the beginning of the long plateau. At lower K^+ contents, the cubic phase expands until all the cations are extracted. The whole mechanism is reversible: in the discharge, the bi-phasic process occurs in the plateau corresponding to the reduction of $Mn^{3+} \rightarrow Mn^{2+}$. However, the mechanism of the depotassiation is not yet clear, hence more details about the redox evolution and local structure of the TMs are essential.

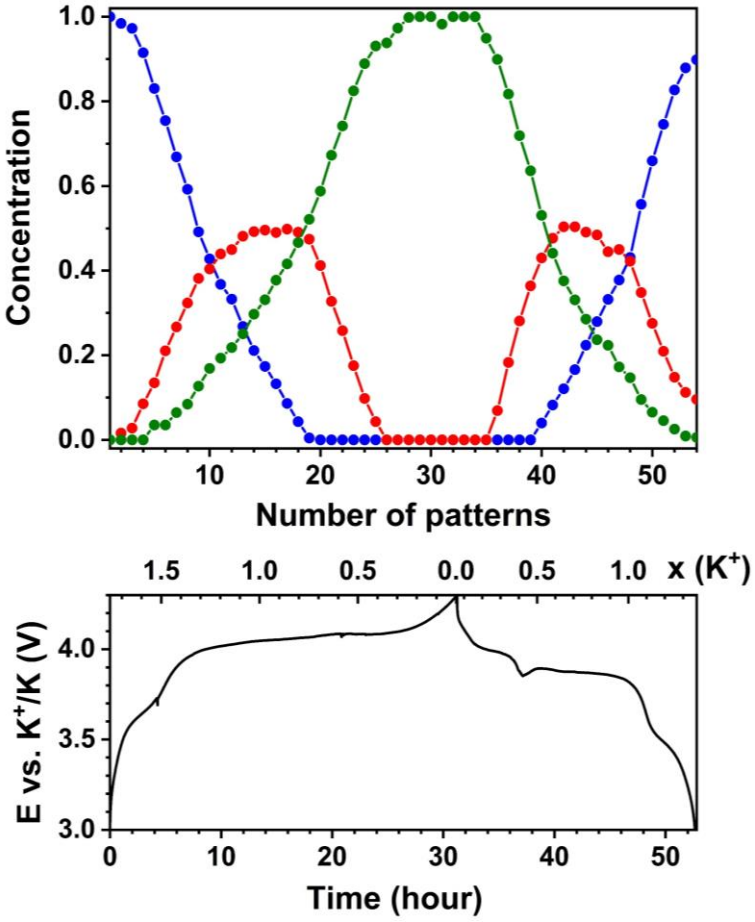

Figure 3.9. Evolution of the relative contributions of the three pure components (component 1: blue, component 2: red, component 3: green) obtained from the PCA and MCR-ALS treatment of the operando XRD in the first cycle (top) and the corresponded cycling profile at 5 mA g^{-1} (bottom).

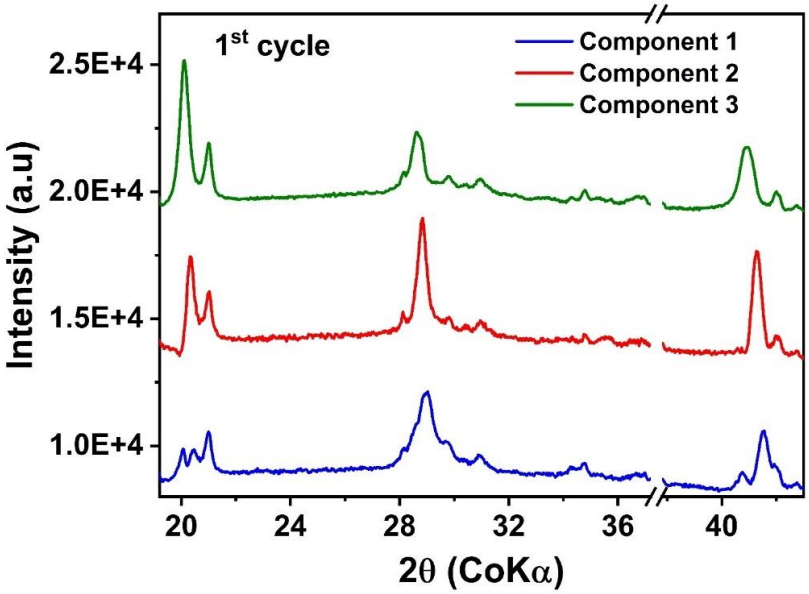

Figure 3.10. Computed XRD patterns of the three MCR-ALS components.

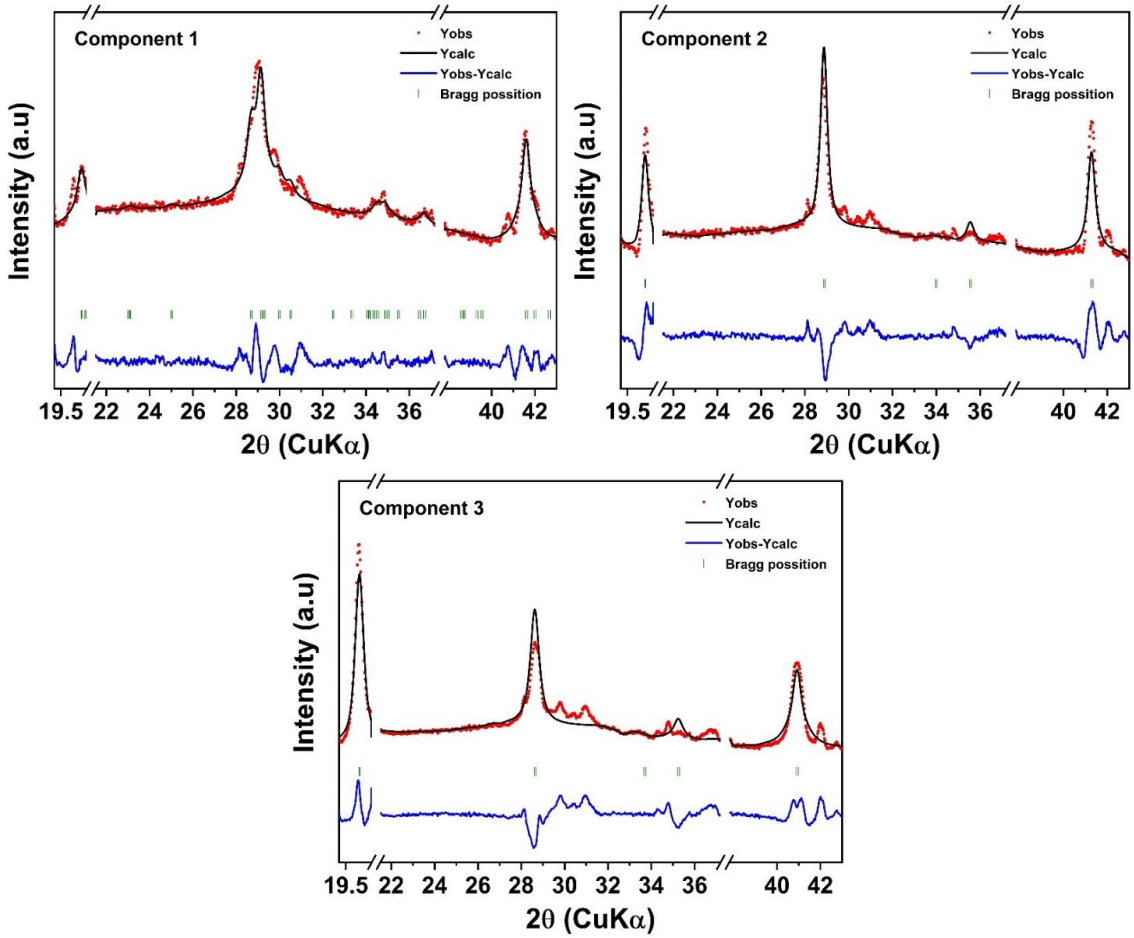

Figure 3.11. Profile matching refinement of three principal components of operando XRD dataset.

Table 3.5. Lattice parameters of three MCR-ALS pure components obtained from Le Bail refinement.

Comp.	SG	a (Å)	b (Å)	c (Å)	β (°)	V/Z (Å^3)
1	$P2_1/n$	10.087(1)	7.184(2)	6.967(6)	90.40(7)	252.4
	(*)	10.007	10.007	10.087	90	252.5
2	$Fm\bar{3}m$	10.159(1)	10.159(1)	10.159(1)	90	262.1
3	$Fm\bar{3}m$	10.244(1)	10.244(1)	10.244(1)	90	268.8

(*) Normalized parameters in a pseudo-cubic lattice based on the calculation in Ref. [95]

c) Operando XAS

Details about the local geometry of the TMs were acquired by *operando* XAS. The Fe and Mn K-edge XANES spectra (Figure 3.12) recorded during the first charge show a clear shift towards higher energies, in line with the expected increases in the oxidation states of the two TMs. In a previous studies of iron hexacyanocobaltate (FeHCCo) by Mullaliu *et al.*[221], a large modification in the Fe K-edge was observed, whereas the Co K-edge varied only very

slightly. In this case, indeed, the iron is the HS state, coordinated to six cyanides via the nitrogen atom, whereas the Co is in the LS state, coordinated to the carbon ends. Similarly, in the case of copper hexacyanoferrate (CuHCFe) [224], only the edge of the metal in the HS state coordinated through the nitrogen varies substantially, whereas that of the LS TM, e.g., Fe in this case, shows a negligible shift during charge/discharge. In both cases, however, the LS TM was supposedly not participating to the redox mechanism. In the specific case of LS Fe^{2+} and Fe^{3+}, however, previous studies on $K_4[Fe(CN)_6]$ and $K_3[Fe(CN)_6]$ show the occurring of only a slight edge shift between the two oxidation states the largest modification being observed in the shape of the pre-edge peaks [222]. The small differences between the spectra of cyanide-coordinated LS Fe^{2+} and Fe^{3+} can be attributed to the intense π-acceptor properties of cyanide ligands, which buffer the change in the positive charge, maintaining the local environment of the Fe virtually unchanged, resulting in stable Fe-C bond lengths [222]. In this case of the HS Fe coordinated to the nitrogen ends of the cyanides, however, π back-donation is much weaker,[236,237] and hence the change in the oxidation state has a stronger influence on the local environment, leading to large shifts on the K-edge XAS spectra.

Now, considering that MF21 contains 72 % of LS Fe and 28 % of HS Fe, and as some HS Fe^{3+} is present already in the pristine material, the slight but significant observed shift of the absorption edge (Figure 3.12a) during the charge process can be attributed principally to the oxidation of the remainder HS Fe^{2+}. For the Mn K-edge spectrum, on the contrary, a large modification of the absorption edge is observed during the depotassiation, corresponding to the oxidation of Mn^{2+} to Mn^{3+}. Such a modification, however, does not occur during the whole charge process, but only starting from the beginning of the second plateau at ~4.0 V. Noticeably, during the oxidation, the intensity of the main edge peak decreases, a new one rises simultaneously at higher energies. The gradual modification of the spectrum lets one identify two isosbestic points at about 5655 and 5685 eV, suggesting that two species are probably sufficient to explain the evolution of the XANES spectra.

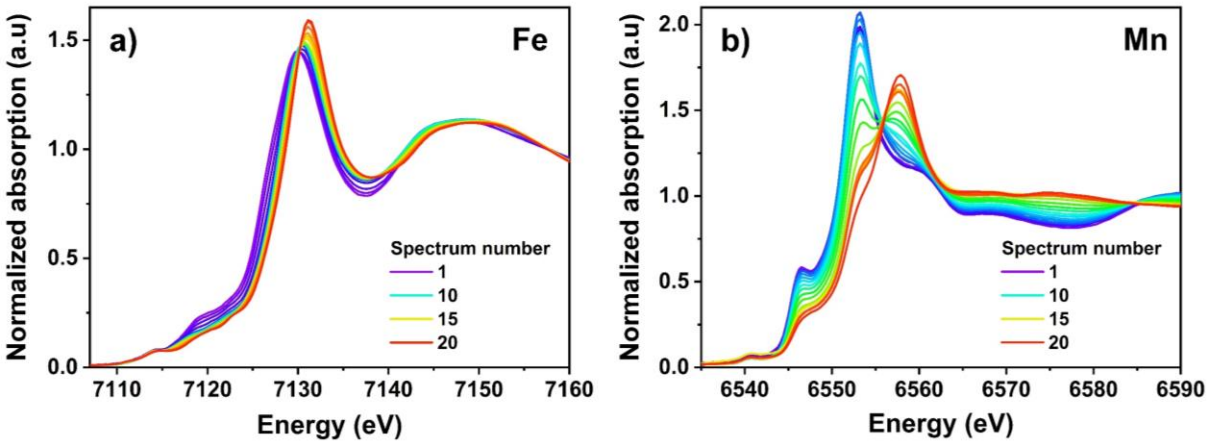

Figure 3.12. Operando XANES at the Fe (a) and Mn (b) K edges in the MF21|K PIB in situ half-cells during the first charge (depotassiation).

The evolution of the FT of the EXAFS spectra (Figure 3.13) shows interesting modification in the coordination spheres of both Fe and Mn centres. The first part of the FT of the Fe spectra (R < 2 Å) corresponds to the first coordination shell of Fe, consisting of a weighed combination of the contributions of Fe-C and Fe-N bonds. In the FT of the first spectrum (Figure 3.13a), the main peak at ~1.4 Å corresponds to the contribution of Fe-C. This peak exhibit a less intense shoulder at higher R, which might account for the contribution of Fe-N, given the molar ratio of these Fe species. When the depotassiation starts, the shoulder decreases in intensity, while the position of the first peak remains almost unchanged during the whole charge. When the reaction approaches the end of charge, the intensity of this main peak strongly decreases. These observations correlate with (i) a decrease in the bond length of Fe-N, due to the oxidation of HS Fe^{2+} to Fe^{3+}, and (ii) the local coordination of LS Fe, which does not change with the oxidation states of the iron, in a good agreement with the XANES results discussed above. The decrease of the peak intensity might be related to a sudden increase of the Debye-Waller factor, related to the presence of several iron sites with slightly different bond lengths leading to a destructive interference of their EXAFS contributions. The second peak of Fe spectra (2 Å < R < 3.2 Å), corresponding mainly to Fe-C≡N and Fe-N≡C shells, shows almost no significant modification in the peak position, but a large decrease in intensity at the end of the process, possibly due to the same reason as that observed in the first peak. The region between 3 and 5 Å mainly corresponds to the Fe-K, Fe-M (M=Fe, Mn) shells, starts modifying after a certain number of spectra particularly in the intensity, indicating a significant change in the coordination sphere of the Fe centres due to the loss of K^+ ions and the oxidation of the TMs.

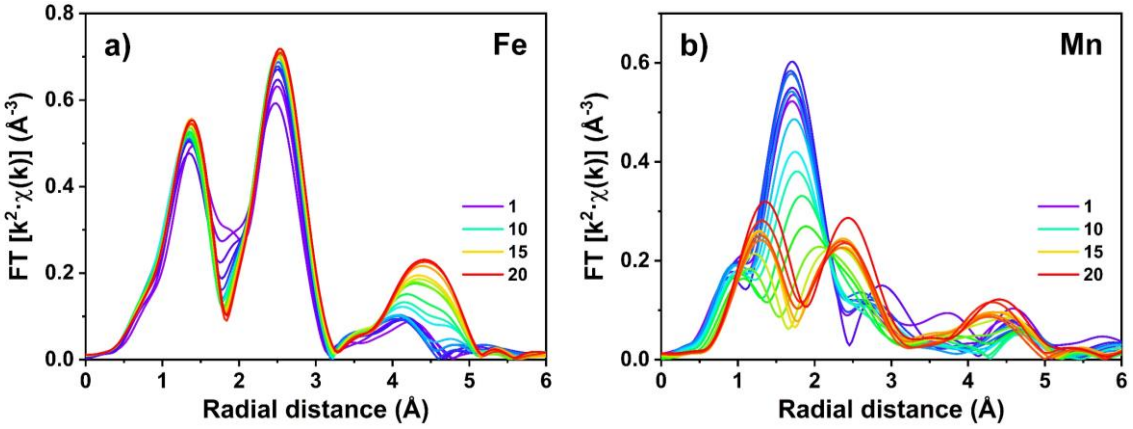

Figure 3.13. Evolution of the FT of the EXAFS of Fe (a) and Mn (b) during the first charge (depotassiation) of MF21.

The *operando* Mn K-edge EXAFS spectra illustrate the oxidation of HS Mn^{2+} to Mn^{3+}. The same redox couple was previously investigated in olivine-based cathode materials [238] as well as in PBAs [239], where the occurring of a JT distortion of the Mn centres could be followed during oxidation. A similar evolution of the first coordination shell of Mn is observed also in the FT of the spectra of MF21 during oxidation (Figure 3.13b): an intensive peak splitting into two distinct peaks of lower intensity highlights once again the distortion of the regular octahedral coordination of Mn with six homogenous bond lengths into two groups of short and long bond lengths, as expected when the JT effect sets in (*vide infra*).

In order to simultaneously follow both the redox reactions at the Fe and Mn sites, and to establish a clear correlation between the different reaction steps with specific redox couples, the two Mn and Fe K-edge XAS datasets were analysed independently. PCA was first applied to determine the number of principal components that can express the variance contained in each series of spectra. The results of such analysis showed that the Fe dataset can be described using three principal components (Figure S3), while two components are necessary for Mn series of spectra (Figure S4). MCR-ALS analysis was then carried out for each dataset with the number of principal components obtained from PCA, and unimodality was applied for all components for the charge process. The graphical results of two MCR-ALS analyses are combined in Figure 3.14.

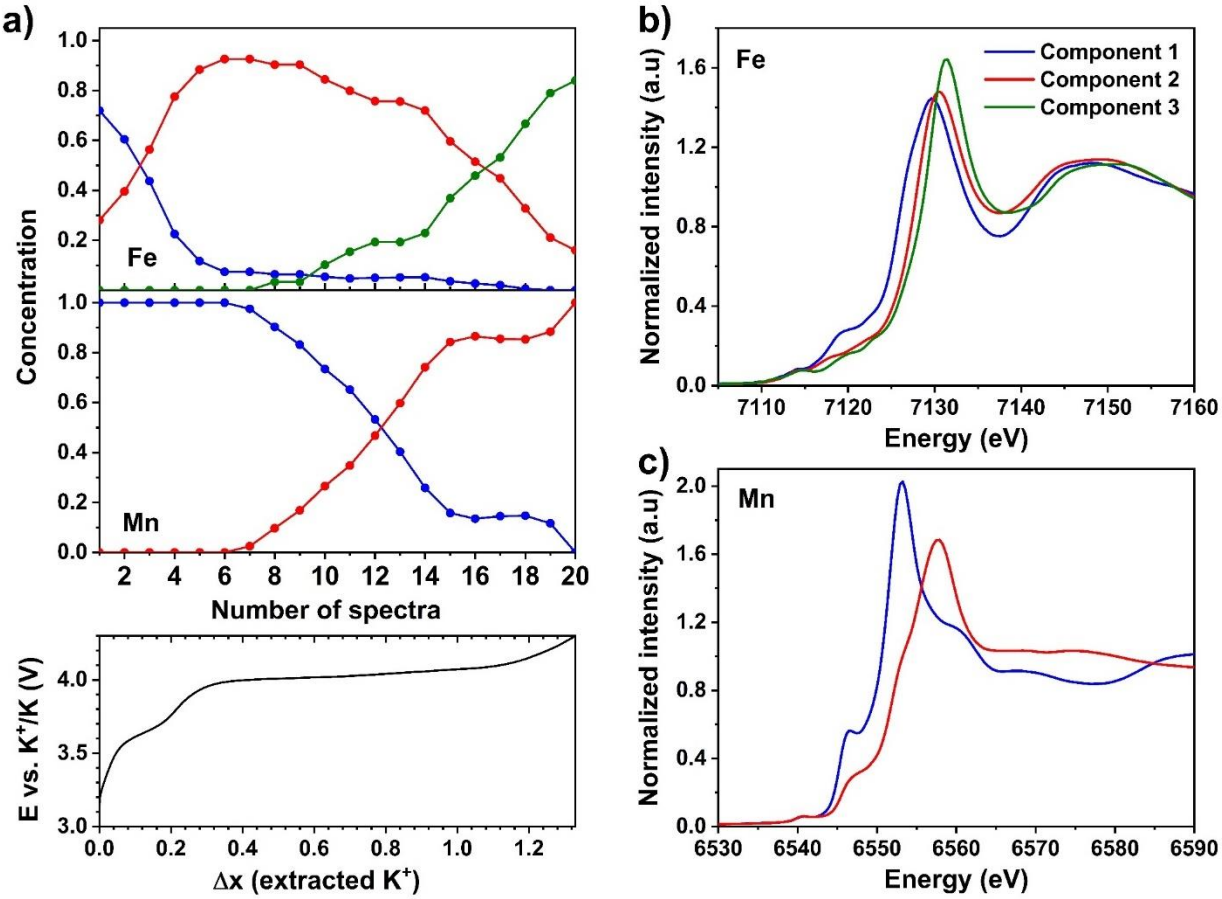

Figure 3.14. (a) Computed concentration profiles obtained from MCR-ALS data treatment of the operando XAS at the K-edge of Fe (top) and Mn (middle) and the corresponding charge profile recorded at 7.5 mA g^{-1}, (b) and (c) are respectively reconstructed spectra of Fe and Mn components.

The concentration profiles of the Fe K-edge XAS spectra (Figure 3.14a) shows the simultaneous presence, at the beginning of the reaction, of a non-negligible fraction of Component 2 together with the dominant Component 1. The concentration of Component 1 decreases rapidly during the first oxidation plateau at ~3.6 V up to an extraction of 0.3 K^+, and almost disappears at the beginning of the second plateau at ~4.0 V, when Component 2 becomes dominant. During the first half of this second plateau, the concentration of Component 2 decreases only slightly, leaving the place to Component 3. The latter increases steadily in concentration only in the second half of the plateau at ~4.0 V, starting from about 0.9 K^+ extracted. Concerning the Mn K-edge XAS spectra, Component 1 corresponds to the pristine MF21 and remains almost unchanged in concentration up to ~0.4 extracted K^+, corresponding to the beginning of the second plateau. Component 2 is then rapidly replaced by Component 1 during the first half of the second plateau up to about 0.9 extracted K^+, when the reaction at the Mn site stops, and is completed only at the very end of the charge.

The pure Fe K-edge components reconstructed by MCR-ALS show a clear edge shift from Component 1 to 2, while the edge of Component 3 is only slightly shifted to higher energies compared to that of Component 2 (Figure 3.14b). Considering also the Mössbauer spectroscopy results (*vide supra*), Component 1 can be safely attributed to the combined signals of LS and HS Fe^{2+}. Component 2 then represents the signals of LS Fe^{2+} and HS Fe^{3+}, and finally Component 3 can be explained by the combination of LS and HS Fe^{3+}. Since components 1 and 3 display the signals of either pure Fe^{2+} or pure Fe^{3+}, their edges are slightly different from those of the first and the last spectra of Fe dataset, which contain a mixture of Fe at both oxidation states and spin states (Figure 3.15a). Spectrum #1, representing the pristine phase containing a small amount of HS Fe^{3+}, the edge of which lies at a slightly higher energy than that of Component 1. The XANES parts of component 3 and spectrum #20 (corresponding to the EOC phase) are almost identical due to insignificant edge shift when LS Fe^{2+} is oxidized (*vice supra*), despite the presence of this species at the EOC state. For the Mn K-edge spectra, instead, the two components 1 and 2, which perfectly match the first and the last spectra of Mn dataset (Figure 3.15b), represent HS Mn^{2+} and Mn^{3+}, respectively (Figure 3.14c).

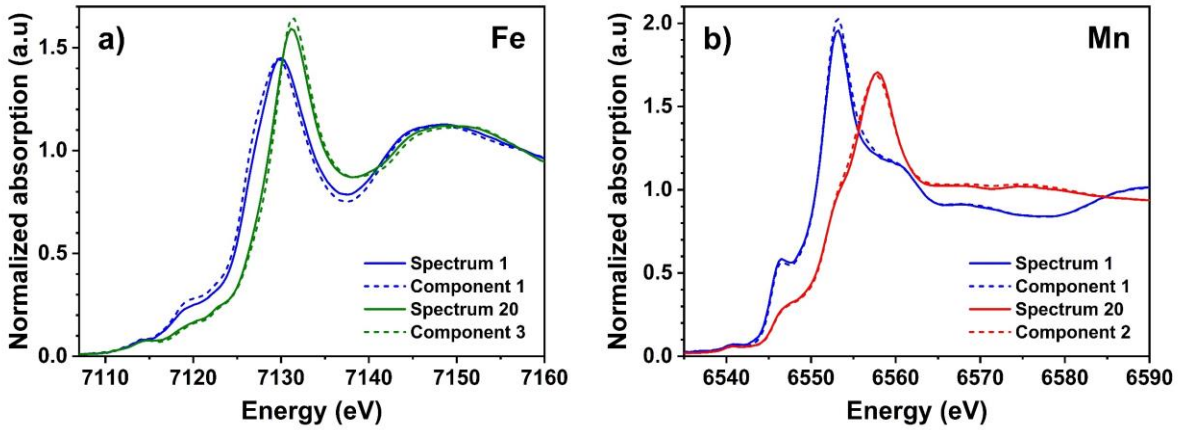

Figure 3.15. Comparison of the XANES part of Fe (a) and Mn (b) K edge of experimental spectra (solid lines) corresponding to the pristine and fully depotassiated phases with the first and last pure components (dash lines) constructed from MCR-ALS analysis.

It is possible to compare the evolution of the concentration of the final components of Fe and Mn, *i.e.*, Component 3 for the Fe K-edge XAS dataset and Component 2 for the Mn K-edge XAS dataset, by representing the smoothed derivative of their concentration vs. potential (Figure 3.16). From this graph, it is possible to appreciate that the oxidation of Mn^{2+} is centred at a lower average potential than that of LS Fe^{2+}. The oxidation of Mn^{2+} therefore starts slightly earlier than that of LS Fe^{2+} and, apart from a small fraction of Mn that oxidises only in the final part of the reaction, is more rapid and is terminated at a lower potential. In the middle of the

plateau, however, both reactions occur simultaneously given the slight difference in voltage between the HS Mn^{3+}/Mn^{2+} and LS Fe^{3+}/Fe^{2+} redox couples in K-containing PBAs.[215]

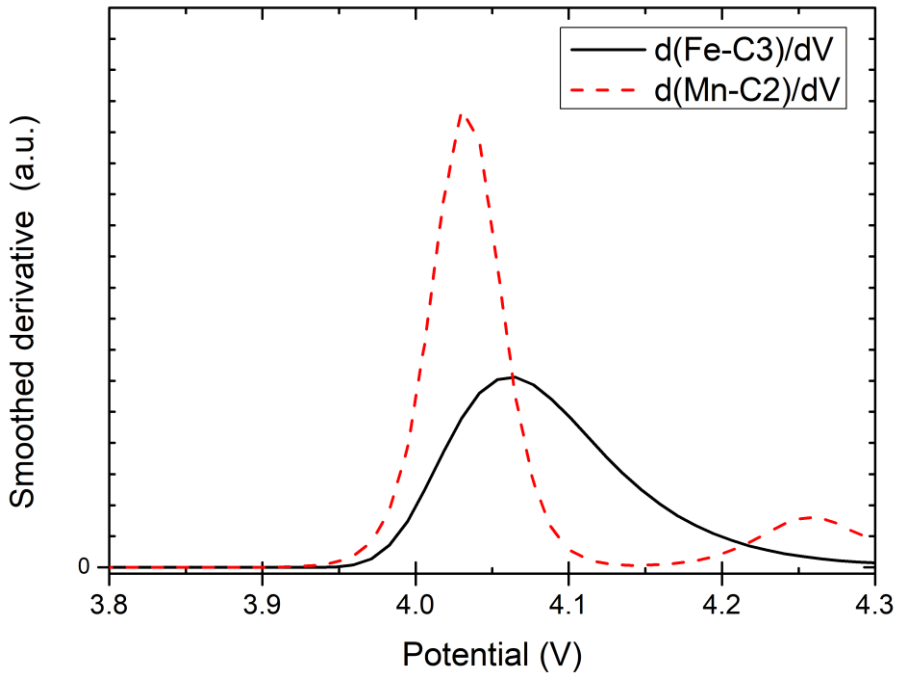

Figure 3.16. Smoothed derivatives of the concentration of the MCR-ALS pure Component 3 of the Fe K-edge dataset and of Component 3 of the Fe K-edge dataset (cf.Figure 3.14).

The results of fit in the *R* space and *k* space of the MCR-ALS pure components of Fe and Mn K-edge EXAFS spectra are shown in Figure 12, and the corresponding fitting parameters gathered in Table 3.6 and Table 3.7. In the case of the three Fe K-edge components, the Fe-C bond length is almost identical in Components 1 and 2, while the Fe-N bond is shortened by 0.15 Å in Component 2 with respect to Component 1. This reduction in the Fe-N bond length confirms the oxidation of the HS Fe site. Only a very slight increase in the Fe-C length is observed, in the case of Component 3, as expected given the strong π-acceptor properties of C-coordinated cyanide ligands which act as a "bonding buffer" making Fe-C bonds covalent in nature and maintain the same bond length in spite of the oxidation state of the Fe. However, as one electron is removed from the LS Fe, there is slightly less electron backdonation from this Fe and that might weaken the π donation from the CN to the HS Fe^{3+},[240] resulting in a small increase in HS Fe–N bond length (Table 3.6). Since the lengths of Fe-N bonds in Components 2 and 3 are very similar to those of Fe-C bonds, a single peak is visible in the FT of the EXAFS signal. Relatively large Debye-Waller factors were obtained for Component 1 at the long-distance shells, *e.g.*, Fe-K and Fe-C≡N-M, indicating a certain disordering in the structure of the PBA. In Component 2, higher Debye-Waller factors were obtained for the Fe-C≡N-M paths,

which might result from the monoclinic → cubic transformation. When the formation of the cubic phase is complete, the structure becomes more ordered, as evidenced by a decrease of the small Debye-Waller factors in Component 3. The length of C-N bonds in all components varies between 1.11 Å to 1.20 Å and remains almost unchanged despite the oxidation of the metal sites.

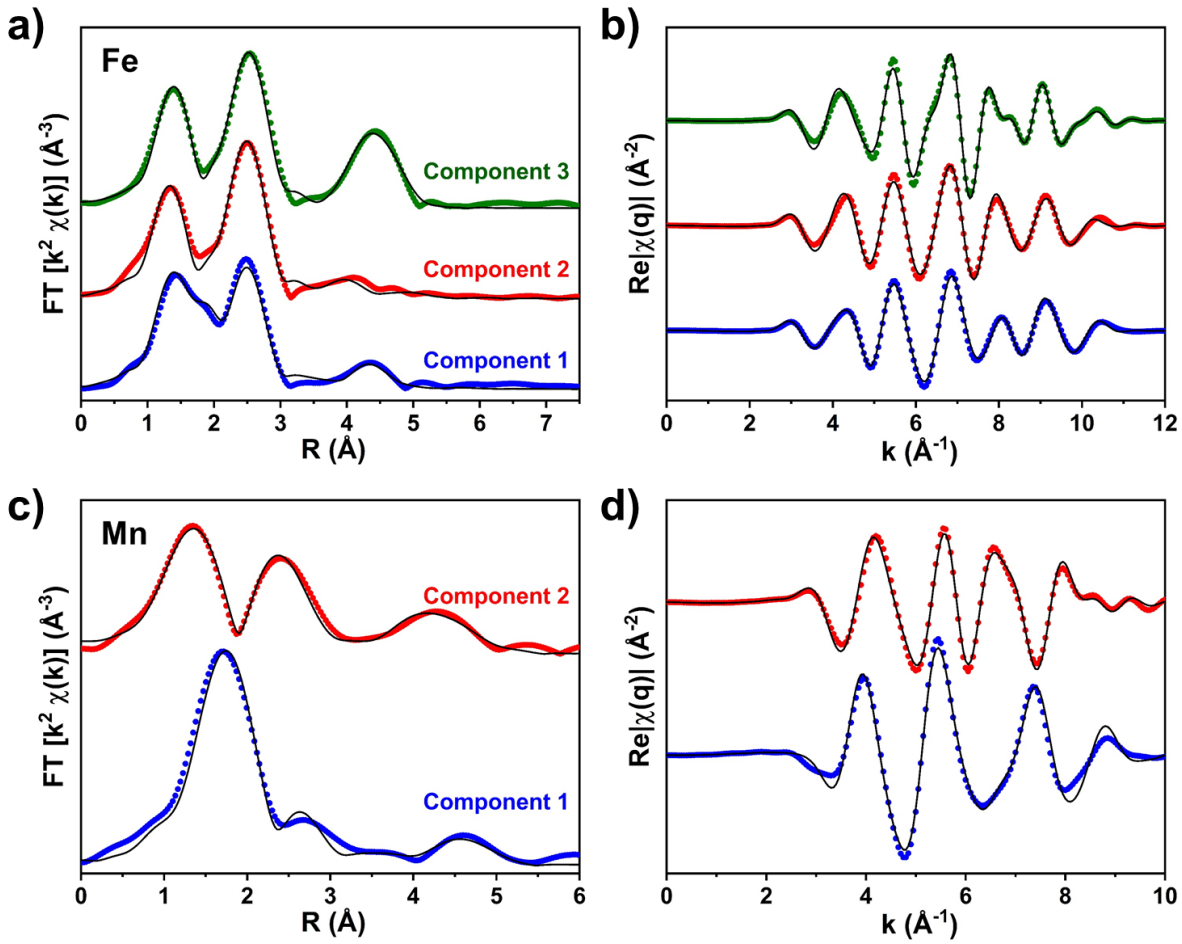

Figure 3.17. Fit of the real part of χ(q) of k^2-weighted Iron (a) and Manganese (c) K-edge EXAFS spectrum FT (k-range: 3 – 11.5 $Å^{-1}$ and 3 – 9.855 $Å^{-1}$, respectively; sine window) in the R space (R-range: 1.0 – 5.5 Å, dR = 0, sine window) for the principal components determined by MCR-ALS. (b) and (d) are the corresponding fits of the real part of χ(q) corresponding to the backward FT by considering only the R-range of 1.0 – 5.5 Å with dR = 0 Å. The circles represent the experimental data, and the solid lines represent the fits.

Concerning the two Fe K-edge components, the Mn-N coordination shells are very different between them, in line with the expected JT distortion around Mn^{3+}. For the pristine material, represented by Component 1, a single Mn-N bond length of 2.24 Å is observed, very similar to the HS Fe-N one (2.21 Å). In Component 2, however, the first coordination shell contains 2 different bond lengths, a short one regrouping 4 ligands at 1.93 Å, and a longer one concerning a second group of 2 ligands at 2.4 Å. The local symmetry of Mn changes from O_h

to D_{4h}, which apparently somehow influences the order of the local structure, as reflected by the very large Debye-Waller factors in Mn Component 2 (Table 3.7).

Table 3.6. Fitting parameters of the pure components related to the Fe K edge spectra of MF21 during the depotassiation. The degenerations were multiplied with the percentage of each correspondent metal sites.

Component	Shell	N	R_{theo} (Å)	R_{fit} (Å)	σ^2
1	Fe-C	4.32	1.84	1.88(1)	0.006(1)
	Fe-N	1.68	2.25	2.21(1)	0.005(2)
	Fe-C≡N	8.64	2.97	3.07(2)	0.006(1)
	Fe-N≡C	3.36	3.21	3.12(6)	0.005(2)
	Fe-C≡N-M	6	5.01	4.96(2)	0.011(3)
	Fe-K (*)	4.9	4.33	4.37(3)	0.015(5)
	Fe-K (**)	1.9	4.58	4.55(4)	0.004(5)
2	Fe-C	4.32	1.93	1.88(1)	0.004(1)
	Fe-N	1.68	1.93	2.03(2)	0.004(1)
	Fe-C≡N	8.64	3.15	3.08(1)	0.004(1)
	Fe-N≡C	3.36	3.15	3.22(1)	0.004(1)
	Fe-C≡N-Fe	6.4	5.08	5.15(3)	0.005(4)
	Fe-C≡N-Mn	5.6	5.08	5.31(6)	0.005(4)
	Fe-K	2	4.33	4.50(5)	0.013(8)
	Fe-C≡N-M-N (***)	13.4	5.53	5.5(2)	0.005(4)
	Fe-N≡C-Fe-C (***)	34.6	5.53	5.39(3)	0.005(4)
3	Fe-C	4.32	1.95	1.93(1)	0.003(1)
	Fe-N	1.68	1.95	2.06(2)	0.003(1)
	Fe-C≡N	4.32	3.18	3.11(1)	0.004(1)
	Fe-N≡C	1.68	3.18	3.25(1)	0.004(1)
	Fe-C≡N-Fe	6.38	5.19	5.21(3)	0.006(1)
	Fe-C≡N-Mn (s)	3.75	5.12	4.81(2)	0.006(1)
	Fe-C≡N-Mn (l)	1.87	5.12	5.4(1)	0.006(1)

(*) single scattering from LS Fe to K^+ neighbors

(**) single scattering from HS Fe to K^+ neighbors

(***) obtuse triangle

(s): short Mn–N bonding

(l): long Mn–N bonding

Table 3.7. Parameters resulting from the fit of the pure components related to the Mn K edge spectra of MF21 during the depotassiation.

Component	Shell	N	R_{theo} (Å)	R_{fit} (Å)	σ^2
1	Mn-N	6	2.12	2.24(1)	0.008(1)
	Mn-N≡C	6	3.18	3.42(2)	0.013(3)
	Mn-N≡C-Fe	6	5.01	5.11(3)	0.017(4)
	Mn-K	6.8	4.33	4.58(5)	0.029(1)
2	Mn-N (1)	4	1.95	1.93(1)	0.014(1)
	Mn-N (2)	2	1.95	2.42(3)	0.014(1)
	Mn-N≡C (1)	8	3.18	3.03(2)	0.012(1)
	Mn-N≡C (2)	4	3.18	3.54(3)	0.012(1)
	Mn-N≡C-Fe (1)	8	5.12	4.99(2)	0.015(2)
	Mn-N≡C-Fe (2)	4	5.12	5.31(5)	0.015(2)

3.3.4. Phase transition and K^+ migration

The correlation between redox reactions, structural transformation, and bonding information of the TMs is illustrated in Figure 3.18. The pristine structure, almost fully K^+ occupied cavities, contains the LS Fe^{2+}, HS Mn^{2+}, HS Fe^{2+} and HS Fe^{3+} with their ratio obtained from Mössbauer spectroscopy and XAS MCR analysis. The average M–N bond length equals to the value of HS Fe^{2+}–N and is not very far from Mn^{2+}–N one, indicating that the amount Fe^{3+} at this site has minor influence on the M–N bonding. The distances between the neighbouring TMs are diminished due to octahedral tilts herein probably caused by a large internal pressure from K^+ ions onto the cyanide groups.[241,242] The extraction of the 0.7 K^+ ion together with the consecutive oxidation of HS Fe and HS Mn causing two modifications: de-tilting the framework and reducing the M–N average bond length. As the content of K^+ ions in the PBA decreases, the transformation from monoclinic to cubic occurs. This phase transition comes along with a lattice increase despite the shorter M–N bonds. As expected, the oxidation of HS Fe^{2+} shortens the Fe–N bond length (Table 3.6). Besides, this cubic phase grows and reaches its maximum during the oxidation of Mn^{2+} (Figure 3.9), thus, Mn^{3+} exists herein, and indeed, its local geometry alters due to the JT effect. Since its axial bonds become longer, and the equatorial ones are shorter (Table 3.7), the average Mn–N bond length is 2.09 Å. Apparently, the oxidation of both HS Fe and Mn reduces the average length of M–N. However, as these reactions happen simultaneously with the depotassiation, which reduces the K^+ content in the structure, hence, to some extent decreases the internal pressure from the alkali onto the cyanide bridges and de-tilts

the framework (Figure 3.18). At the end of depotassiation, most of the TMs stay at +3 oxidation state, and since the bond lengths of LS Fe–C and HS Fe–N slightly increase, the unit cell expands.

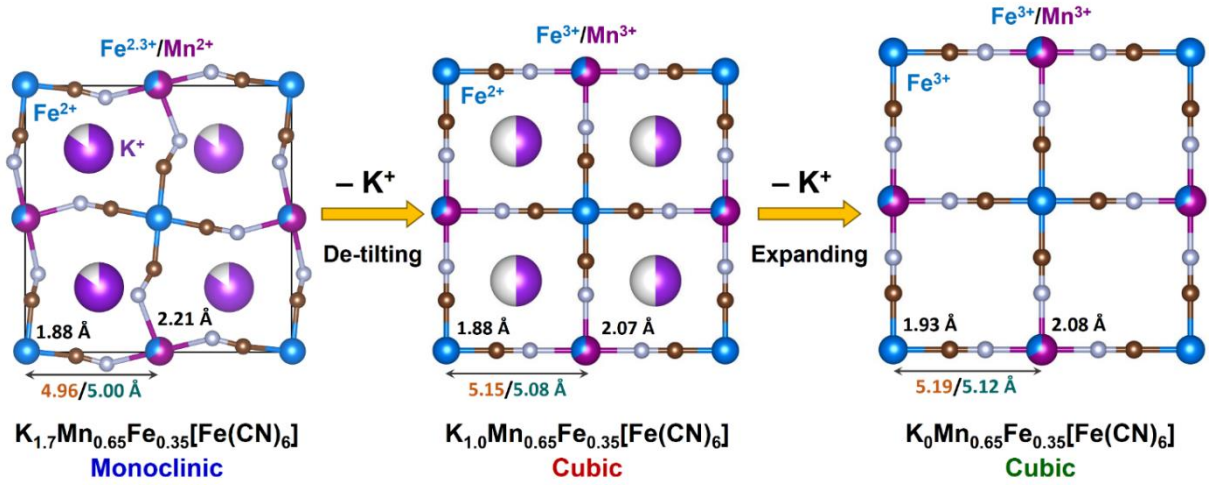

Figure 3.18. Schematic phase transition occurring in the depotassiation by combining operando XRD and XAS analysis. The M–N (M= Fe, Mn) bond lengths are the mean values calculated from EXAFS fits of pure components. The Fe–C–N–M distances are deduced from mean values of EXAFS fit data (orange) and lattice parameters of XRD pure components (dark teal).

Comparing with other reports on the JT effect at the Mn^{3+} observed at the EOC of other battery materials, this effect appears stronger than those in the literature[243,244]. The two long axial Mn-N bonds (2.42 Å) can be weaken during the continuous lattice expansion/compression, possibly inducing the creation of inactive Mn sites by the dissolution of Mn ions in the electrolyte. This observation might explain the modification of the mechanism and thus of the performance of MF21 during cycling, which becomes evident by looking at the derivative of the capacity of MF21 in half-cell after 1, 2, and 50 cycles (Figure 3.19). In the first cycle, all the three processes are reversible with very similar capacity contribution from HS Mn and LS Fe. However, in the second charge, the contribution of HS Mn decreases, and after 50 cycles, most of the capacity fading can be attributed to the decline of the Mn^{3+}/Mn^{2+} reaction.

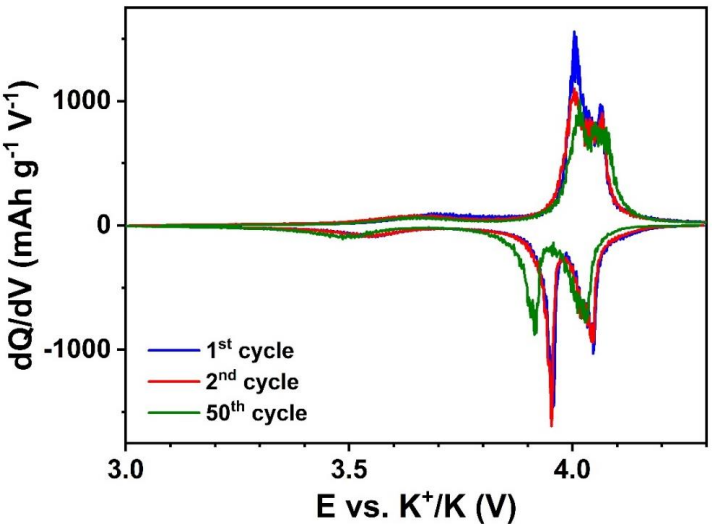

Figure 3.19. Derivative capacity of MF21 after 1, 2, and 50 cycles constructed from galvanostatic profiles in Figure 3.5.

To better understand how the structural transformation may affect the K^+ migration, GITT was conducted for the first discharge (Figure 3.20). In general, the open framework of MF21 facilitates the migration of K^+ ions, which is deduced from the high diffusion coefficients (10^{-11} – 10^{-10} cm^2/s) calculated from the GITT signal, which is comparable with the transport kinetics of Na^+ into the PB hosts.[243,244] However, a slightly decreased diffusion coefficient is observed in the plateau corresponding to the reduction of HS Mn^{3+}. In this process, two long axial bonds of Mn^{3+} shorten, leading to the shrinkage of the lattice observed in the *operando* XRD. This structural rearrangement could influence the insertion and re-ordering of K^+.

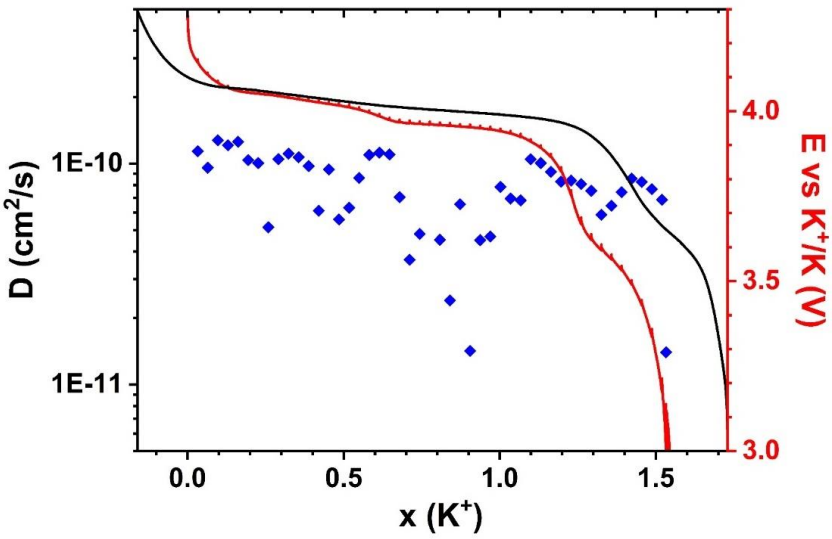

Figure 3.20. Evolution of diffusion coefficients of K^+ in the first discharge (blue diamonds) with the first charge (black line) and GITT curve (red line) of the discharge.

3.4. Conclusions

Complementary electrochemical and material characterizations give us a comprehensive view on the mechanisms of the PBA $K_{1.67}Mn_{0.65}Fe_{0.35}[Fe(CN)_6]_{0.92}\cdot 0.45H_2O$, which shows a good electrochemical performance with three redox reactions that can be well distinguished by combining ^{57}Fe Mössbauer and X-ray absorption spectroscopy. The local geometry on Fe and Mn sites provides valuable information on the structural evolution of the PBA, with the oxidation of Mn^{2+} taking place before that of LS Fe^{2+} with the involvement of a coordination distortion due to Jahn-Teller effect, which results in monoclinic-to-cubic crystal structure modification. This phase transition slows down the insertion of K^+, and the continuous bond breathing of Mn can lead to an unrecoverable structure and deactivated Mn sites. Although PBAs are a promising family of cathode materials for PIBs, it is essential to optimize the chemical composition in order to minimize the battery failure due to significant structural global and local modification.

Supplementary information

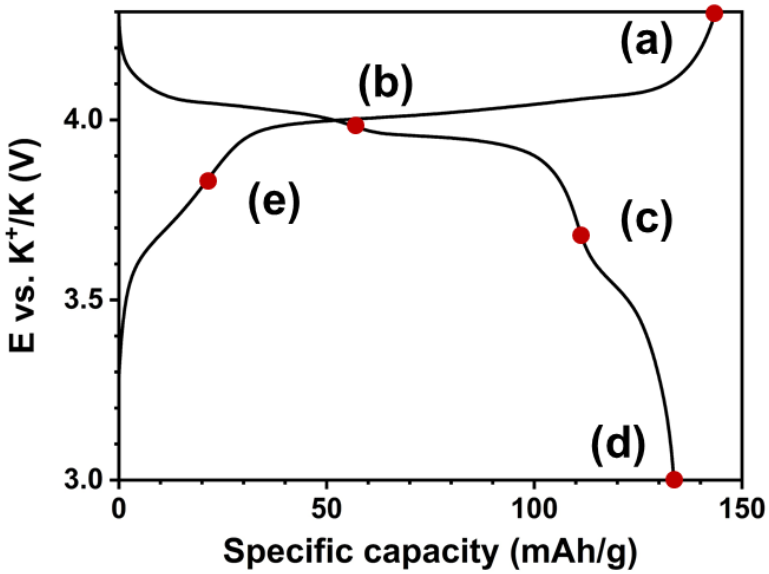

Figure S1. Galvanostatic curve of MF21 | K half-cell at the current density of 5 mA g^{-1} with 5 selected states (red dots) at which ex situ Mössbauer spectra were recorded.

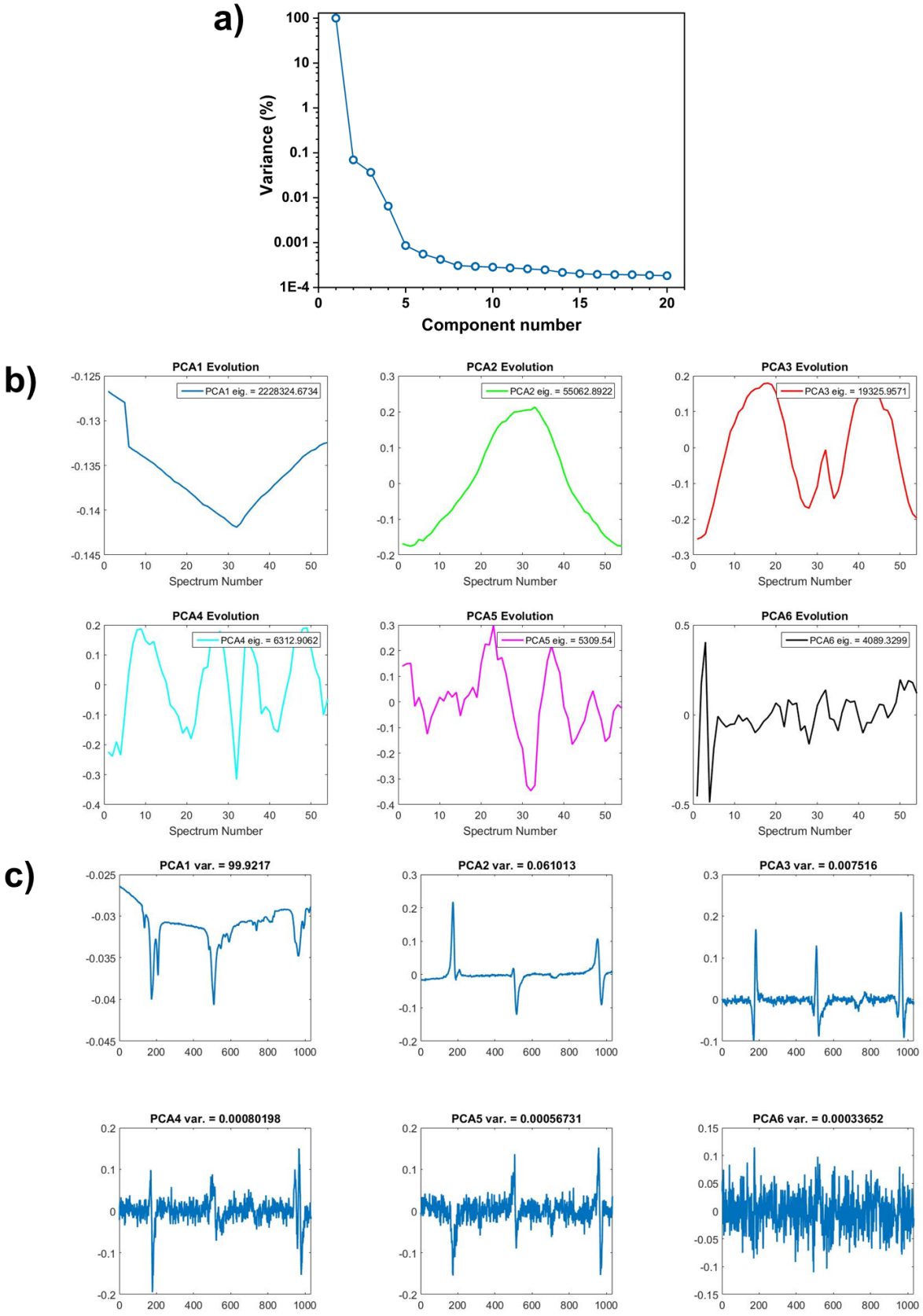

Figure S2. (a) Variance plot, (b) the evolution and (c) the patterns of principle components of the operando XRD dataset in the first K^+ extraction-insertion cycle of MF21.

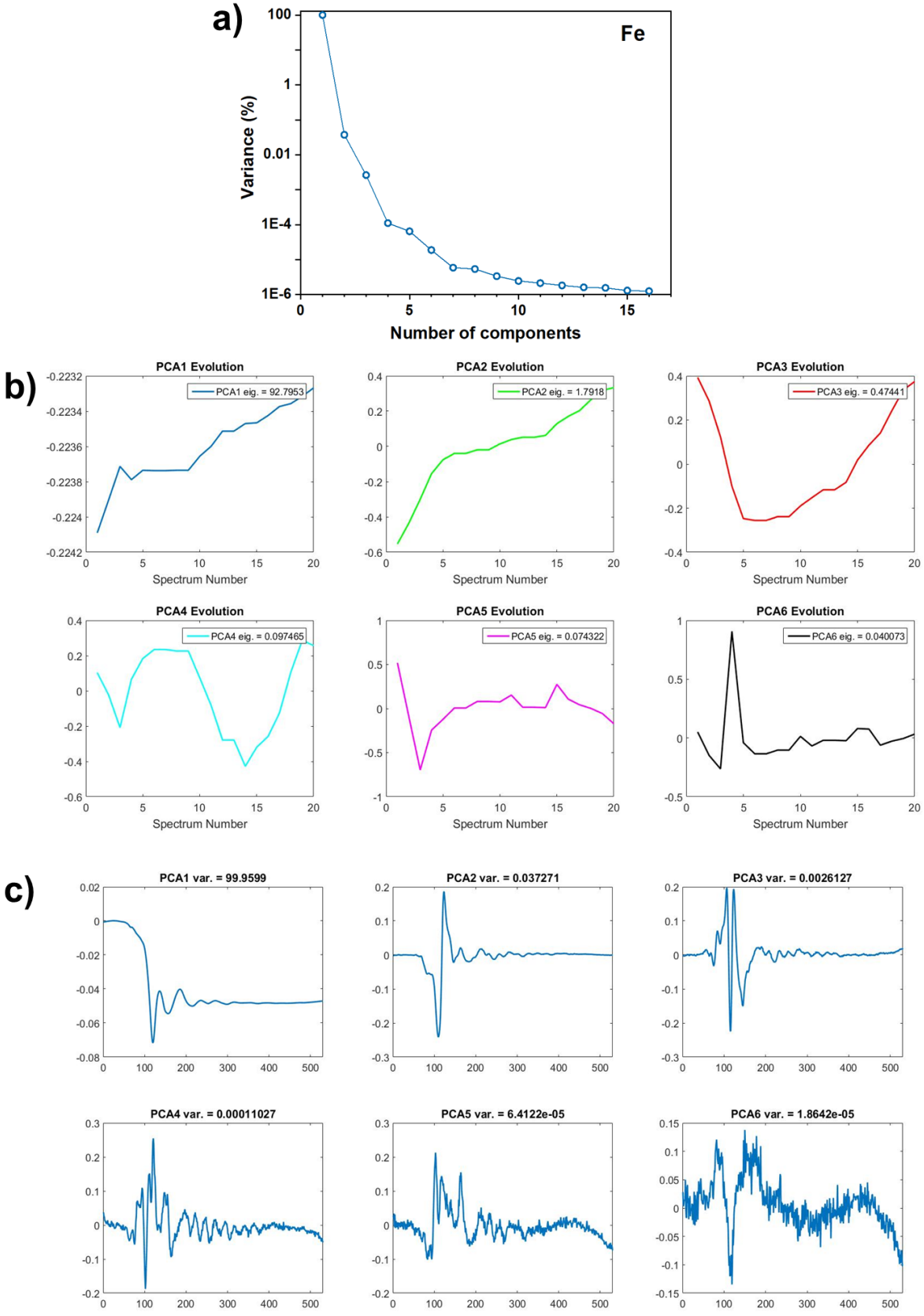

Figure S3. (a) Variance plot, (b) the evolution and (c) the patterns of principle components of the operando XAS dataset at Fe K edge in the first K^+ depotassiation of MF21.

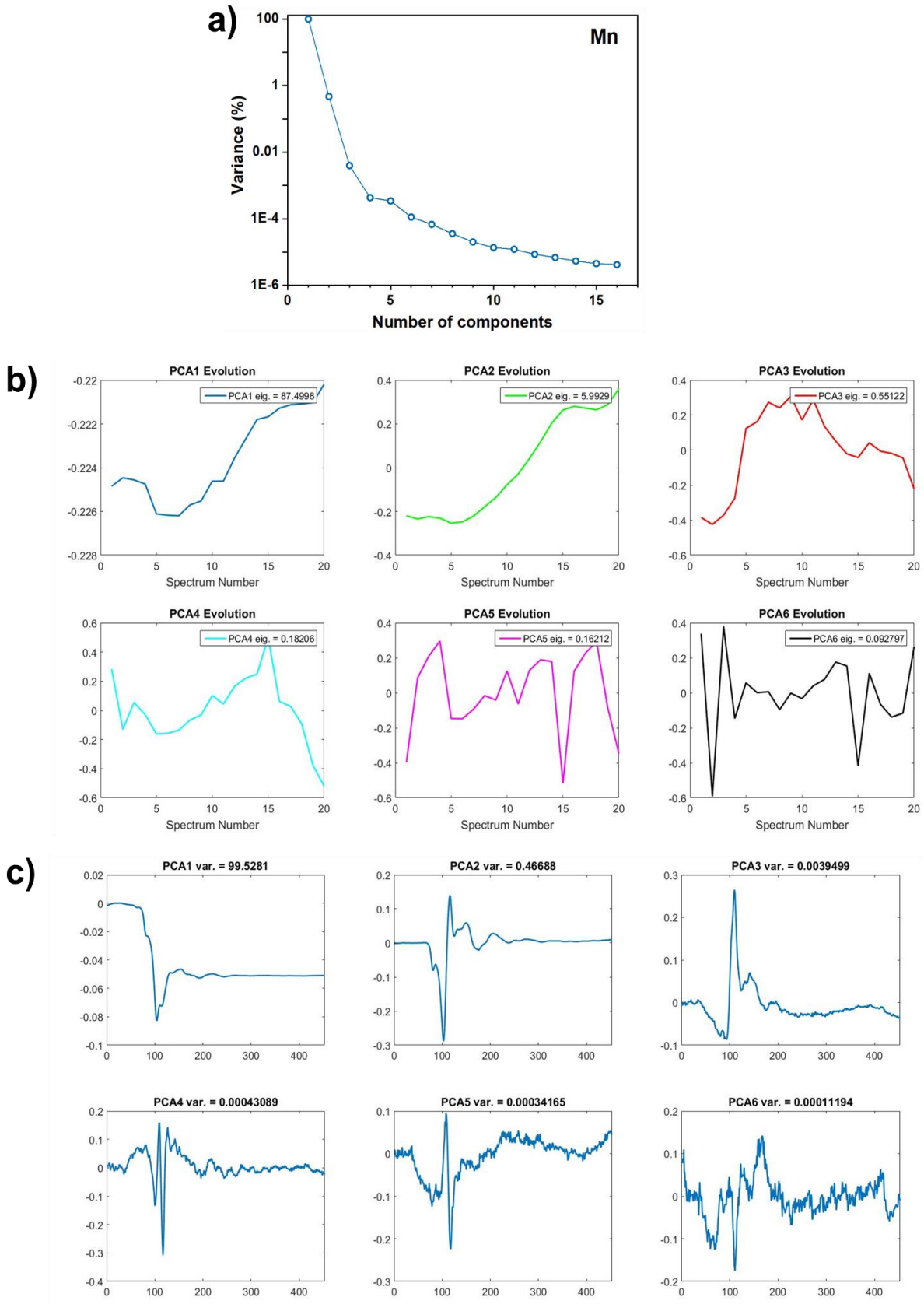

Figure S4. (a) Variance plot, (b) the evolution and (c) the patterns of principle components of the operando XAS dataset at Mn K edge in the first K^+ depotassiation of MF21.

CHAPTER 4.
DEVELOPMENT OF A POTASSIUM-ION FULL CELL BASED ON PRUSSIAN BLUE ANALOGUES AND GRAPHITE

The cycling performance of graphite and MF21 with DME-based HCEs have shown that they are excellent candidates to become electrodes for PIBs. Together they can make a PIB with an average operating potential at *ca.* 3.5-3.8 V with a theoretical capacity of 130-140 mAh g^{-1}. These promises enable PIBs to compete with some current SIBs[245,246].

Two determinants should be considered to obtain a practical PIB: (i) finding an appropriate capacity balancing and (ii) understanding the behaviors of electrode materials in the cell. From half-cell results, the positive-to-negative (P/N) mass ratio was found to be 2.0, equivalent to a capacity balancing of $Q_{cathode} : Q_{anode} = 1$. Swagelok three-electrode set-ups with K metal as the reference were used to understand the potential responses of the electrodes *versus* K^+/K as well as each other. Slight excesses of MF21 (P/N = 2.1 and 2.2) were employed with the expectation to mitigate the capacity contribution from the SEI formation on graphite. When the voltage limit is applied on one electrode, overcharging is observed on the other. The cell response in both Swagelok and coin-cell configurations demonstrate low initial discharge capacity and poor cyclability, which is accounted for significant contribution from SEI formation on graphite in the first charge. Therefore, precycled graphite electrodes are employed in full cells to evaluate the influence of capacity balancing. In a wide range of P/N ratios (1.6 – 2.6), the full cell at P/N = 1.8 exhibit the best performance with capacity of 113 mAh g^{-1} and a CE of 85 % in the first cycle. After 70 cycles, the capacity remains 66 % of the initial value. The results are quite modest comparing with those reported for graphite//$K_2MnFe(CN)_6$ systems with or without electrode or electrolyte pretreatment in the literature, nevertheless, all these pioneer studies suggest further modification/optimization of electrodes and electrolytes to create a practical PIB.

The synthesis of MF21, the electrode formulation and the half-cell measurements were carried out at ICGM. Full cell electrochemical experiments were conducted at both ICGM and Chalmers University of Technology.

4.1. Introduction

In the last decades, an enormous number of electrode materials and electrolytes has been evaluated in PIBs. On the cathode side, Prussian blue analogues (PBAs) are considered as one of the best performing materials. PBA with Mn and Fe as redox active elements, *i.e.*, $K_2MnFe(CN)_6$, can offer a reversible capacity up to 130 mAh g^{-1} with the average working potential of 3.8-4.0 V vs. K metal.[94–96,247] On the anode side, graphite is one of the leading negative materials for PIBs, due to its commercial availability, low cost, high capacity, and superb reversibility despite the large volume expansion caused by K^+ intercalation.[37,63] In half-cell, the intercalation of K^+ into graphite occurs at 0.2-0.3 V. Therefore, PBAs and graphite make a perfect match for practical 4-volt PIBs.

To create PIBs of PBA and graphite as electrodes, it is imperative to find a suitable electrolyte. Carbonate-based electrolytes were found to demonstrate poor cycling stability towards both electrodes.[95,100,248] FEC (fluoroethylene carbonate) additive can improve the reversibility of PBA[95], yet it downgrades the performance of graphite[120]. In contrast, glyme-based highly-concentrated electrolytes (HCEs) using KFSI (potassium bis(fluorosulfonyl)-imide) as salt are quite compatible with graphite[40], but unstable towards PBA, while when KFSI is replaced by KTFSI (potassium bis(trifluoromethanesulfonyl)imide) better performance is obtained[113].

To date, there is a limited number of publications in the literature on electrochemical characterization of graphite//PBA full cells with different electrolytes, such as KPF_6/EC-DEC[95], KFSI/TEP (triethyl phosphate) HCE[94,100,247], and ionic liquids[249], yet none of them mentions how to define the capacity balancing, nor the response of electrode materials in full cells, which are crucial to optimize the cell configuration. Herein, the performance of a full cell based on $K_{1.67}Mn_{0.65}Fe_{0.35}[Fe(CN)_6]$ and graphite with 5 M KTFSI in DME is evaluated in both coin cell and three-electrode systems. The influence of the balance of the two electrode materials on long-term cycling of the full cell using precycled graphite as anode to eliminate the contribution of SEI formation is investigated in the range of positive-to-negative (P/N) ratios from 1.6 to 2.6., which helps determine the ideal electrode balance for further optimizations.

4.2. Experimental

4.2.1. Material preparation

Graphite (SLP30, TIMCAL^{TM}) was used as received. Prussian Blue Analogue $K_{1.73}Mn_{2/3}Fe_{1/3}[Fe(CN)_6]\cdot xH_2O$ (MF21) was synthesized via precipitation method. One aqueous solution of $K_4Fe(CN)_6$, and a second one of $MnSO_4\cdot H_2O$ and $FeSO_4\cdot 7H_2O$, were prepared by dissolving the corresponding salts in saturated KCl. The latter solution was slowly added to the former one at 60 ℃, and the final mixture was stirred for 24 hours. The product was washed with deionized water, then with ethanol, centrifuged and finally dried under vacuum. An extra drying step (100 ℃, overnight) was applied to remove the residual physiosorbed water. The final material was stored in an Argon-filled glovebox and just taken out for electrode formulation.

4.2.2. Electrochemical characterization

a) Electrode formulation

Graphite was mixed with polyvinylidene fluoride (PVdF, Solef® 5130) with a mass ratio of 90/10 in N-Methyl-2-pyrrolidone (NMP) by planetary ball milling for one hour. The slurry was casted on copper foil with a thickness of 100 μm to obtain the mass loading of active material of 2.0 mg cm^{-2}. The film was dried in air, then punched into round-shape electrodes with the diameter of 1.27 cm, and further dried at 80 ℃ under vacuum for 24 hours before use.

PBA electrodes were prepared by thoroughly mixing the pristine powder with Super P and polytetrafluoroethylene (PTFE) at the mass ratio of 60/30/10. The mixture was ground in a mortar, rolled, pressed into a thin film, which was then cut into round pieces at 1.0 cm diameter. The mass loading of the electrodes varies from 4.1 to 6.6 mg cm^{-2}, equivalent to the positive-to-negative mass ratios (denoted as P/N ratios) varying from 1.6 to 2.6.

b) Electrochemical examination

Galvanostatic tests were conducted at 25 ℃ on a MPG-2 Biologic potentiostat with 5 M KTFSI in DME as the electrolyte, Whatman GF/D glass fiber and Celgard 2325 as separators either in CR2032 coin cells or Swagelok three-electrode cells. The cells were assembled in Ar-filled glovebox (O_2 < 0.5 ppm, H_2O < 0.5 ppm). The cycling performance of graphite and MF21 in half cells vs. K metal was evaluated at the current density of 25 mA g^{-1} in the voltage range of 0-2.0 V for graphite and 3.0-4.3 V for MF21. 3-electrode Swagelok configuration with K metal as the reference electrode was used to evaluate the performance of graphite//MF21 full cell at P/N = 2.1 and 2.2. In each cell, either anode or cathode respectively was chosen as the

working electrode, of which the operation voltage was controlled in the same range as in half-cells, and the potential responses of the other electrode versus K metal and versus the working electrode were recorded with no constraint. The SEI on graphite was pre-formed by cycling the half-cells of the electrodes at 25 mA g^{-1} (graphite) for one cycle. Full cell tests of MF21 and graphite as cathode and anode, respectively, were carried out at 10 mA g^{-1} in both Swagelok and coin-cell set-ups. The current rate and specific capacity of all full cells were calculated based on the mass of MF21.

4.3. Results and discussion

4.3.1. Cycling performance of graphite and MF21 in K-ion half-cells

Before the full cell studies, the cycling performance of MF21 and graphite was examined in half-cells separately (Figure 4.1). MF21 delivers a high initial discharge capacity of 124 mAh g^{-1} with a Coulombic efficiency of 93 % (Figure 4.1a,b). After five cycles, the CE reaches a stable 98.7 %, but a slight capacity fading of 15 % in the long-term cycling, probably due to the irreversible structural expansion/contraction addressed in Chapter 3. In contrast to high initial Coulombic efficiency (CE) of MF21, graphite experiences a large capacity loss (~35 %) in the first cycle due to the SEI formation (~16 %) and probably parasitic reactions between K metal and the electrolyte (~19%). Even though, graphite demonstrates a sterling performance with a stable discharge capacity of 244 mAh g^{-1} after five cycles until the end of the experiment and in this period the average CE is 99 % (Figure 4.1c,d).

According to the half-cell results, after five cycles, the CE of each electrode reaches maximum, why the discharge capacities of the materials in the 5th cycle are used to calculate the P/N ratio. The balancing calculation was described elsewhere[250] and the P/N ratio can be obtained from the following equation:

$$P/N = \frac{m_{MF21}}{m_{graphite}} = \frac{Q_{graphite}}{Q_{MF21}}$$

in which, Q is the specific discharge capacity (mAh g^{-1}) of either MF21 or graphite. To balance the actual capacities of the materials ($Q_{MF21} = Q_{graphite}$), the P/N ratio is 2.0. The full cells of MF21 and graphite are initially assembled with P/N close to 2.0 and afterwards with a wide range of P/N ratios, from overbalanced anodes (excess graphite, P/N < 2.0) to overbalanced cathodes (less graphite, P/N > 2.0).

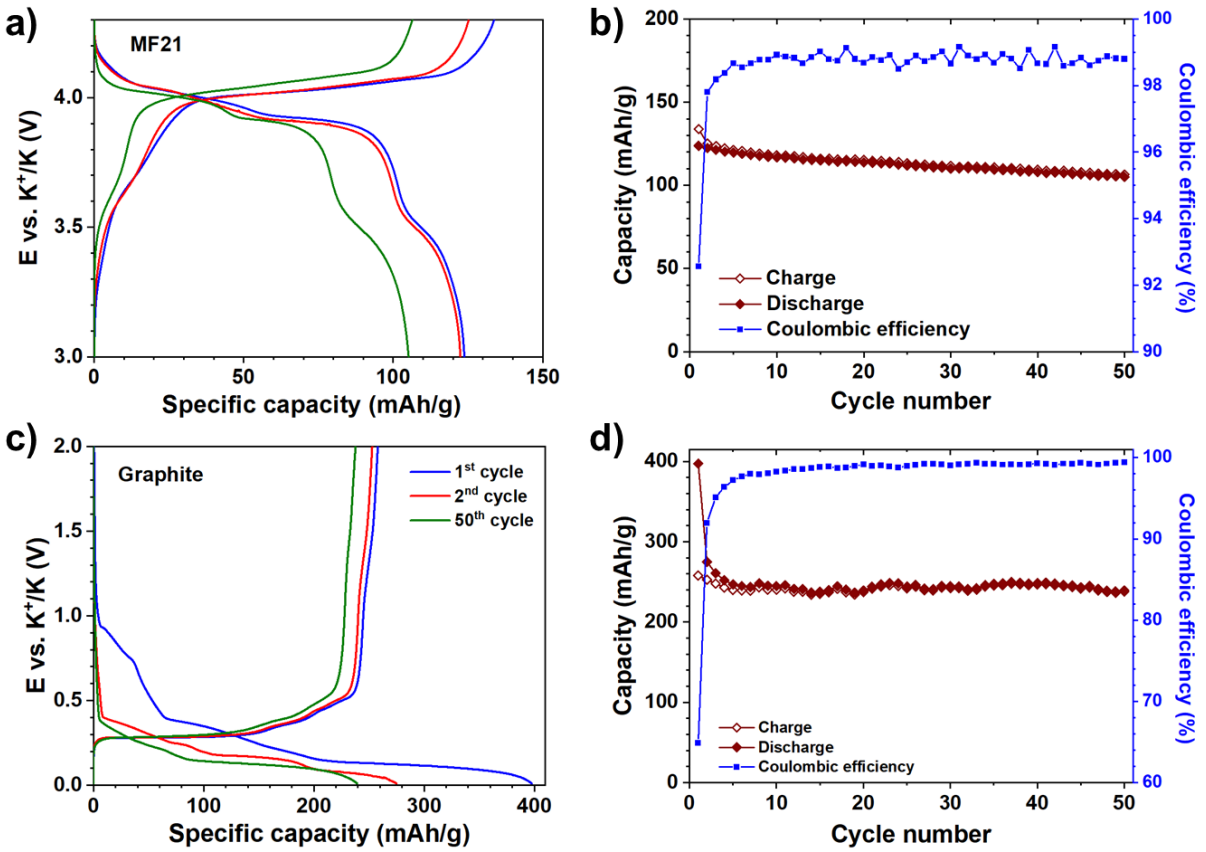

Figure 4.1. Galvanostatic profiles and cycling retention of MF21 (a,b) and graphite (c,d) at the current density of 25 mA g^{-1}.

4.3.2. Full cell electrochemistry with fresh electrodes

The performance of graphite//MF21 configuration is evaluated in Swagelok and coin-cell set-ups (Figure 4.2, Figure 4.3, and Figure 4.4) with a slight excess amount of MF21 to partially compensate for the irreversible capacity of the SEI formation. Under cathode-oriented condition, MF21 shows a similar first cycle as in half-cell. However, while MF21 is fully charged, the discharge of graphite stops at the middle of the intercalation (*ca.* 0.2 V), resulting in a much lower capacity than that obtained in half-cell (Figure 4.1c). During the cell discharge, MF21 exhibits an excellent reversibility with only 3 % of capacity loss in the discharge. In contrast, graphite shows a remarkably worse performance than its counter electrode in this process with only 52 % of its initial discharge capacity can be extracted up to 3.47 V, and concurrently, the cell voltage response reaches 0.41 V with a discharge capacity of 76 mAh g^{-1} (CE = 61 %). During the second half of the cathode reaction, the potential of graphite endures at *ca.* 3.5 V, inducing an overcharge which probably corresponds to electrolyte decomposition. Consequently, the cell voltage declines to negative values, and hence, a severe battery failure.

Under anode-oriented condition (Figure 4.2b), during the cell charge, graphite displays a similar potassiation curve as in half-cell (Figure 4.1c). The formation of SEI contributes a

similar amount to the total discharge capacity of graphite, and the absence of K metal as counter electrode prevents, in principle, the unwanted reaction with the electrolyte. Meanwhile, MF21 undergoes an overcharge with a long plateau above 4.5 V, resulting from electrolyte oxidation at high potential beyond its ESW[251]. However, in the cell-discharge process, both electrodes exhibit unsatisfied performances: large irreversible capacity (52.6 %) on graphite and incomplete reduction on MF21. The cell voltage response demonstrates two distinguished plateaus at *ca.* 2.9 and 3.8 V in each half cycle, as well as the overcharge plateau is observed above 4.3 V.

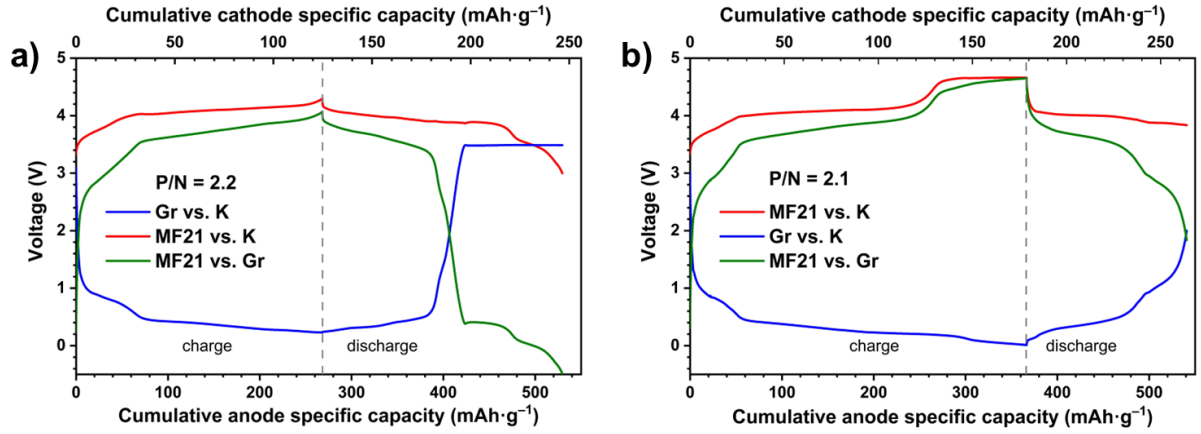

Figure 4.2. The first cycle of graphite//MF21 Swagelok cell with two different protocols: (a) cathode orientation (P/N = 2.2) and (b) anode orientation (P/N = 2.1).Red: Positive electrode potential (V vs. K^+/K), Blue: Negative electrode potential (V vs. K^+/K), Green: Cell voltage response (V). The potential range was limited referring to MF21 (a) and graphite (b), respectively.

The cycling performance of graphite and MF21 in the anode-oriented cell is followed up to 20 cycles (Figure 4.3). Similar phenomena, *i.e.*, overcharge on cathode, SEI-like contribution at the beginning of discharge and low reversibility at the anode, are observed in the second cycle (Figure 4.3a,b). The overall shape of cell potential profile in the range of 2.0-4.3 V shows almost no difference from the first cycle. As observed in the first cycle, overcharge above 4.5 V in the second one derives from the irreversible capacity of graphite, but its capacity steadily reduces together with the improvement in the cycling reversibility of graphite after a few cycles (Figure 4.3c). The cell capacity decreases slightly and retains at *ca.* 80 mAh g^{-1}, while the CE of the cell increases up to 93 % and remains stable at this value during the measurement (Figure 4.3d). Based on the shape of the cell response curves in Figure 4.2 and Figure 4.3, the voltage limits are 4.3 V for the charge (before the electrolyte oxidation) and 2.0 V for the discharge (full charge of graphite).

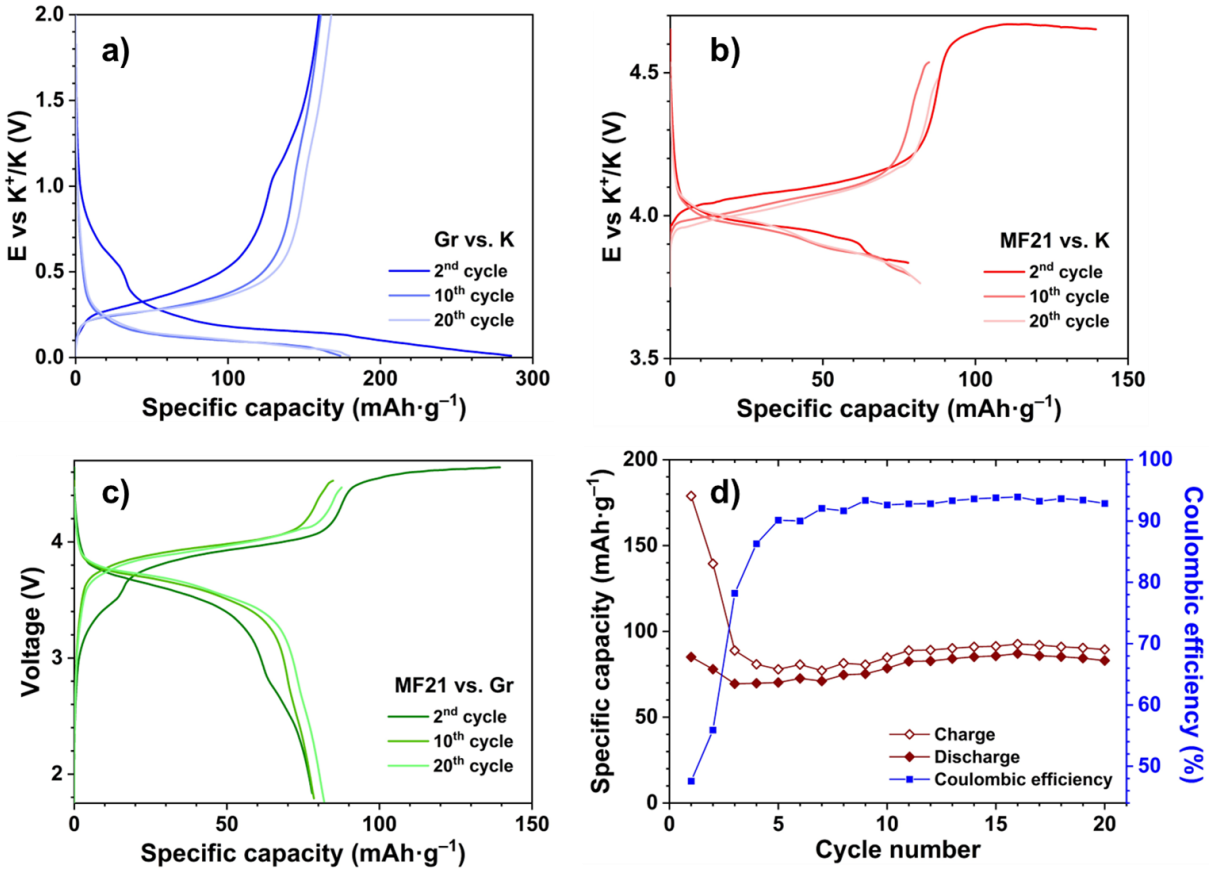

Figure 4.3. Galvanostatic profiles of (a) graphite vs. K^+/K, (b) MF21 vs. K^+/K, (c) cell voltage response and (d) cycling retention of graphite//MF21 Swagelok full cell (P/N = 2.1) under anode orientation recorded at I = 10 mA g^{-1}.

The overall performance of graphite//MF21 full cell at P/N = 2.1 is re-assessed in coin cell configuration (Figure 4.4). The shape of potential response here resembles that obtained in anode-oriented Swagelok cell. The ICE of the coin cell is 61.5 % likely owing to unfinished charge/discharge of the electrodes encountered in Swagelok cells. During the long-term measurement, the cell capacity decreases gradually and remains 50 mAh g^{-1} after 20 cycles. The CE reaches 96 % after 4 cycles, then decreases steadily, and the measurement finishes with the CE of 85 % at the 20th cycle.

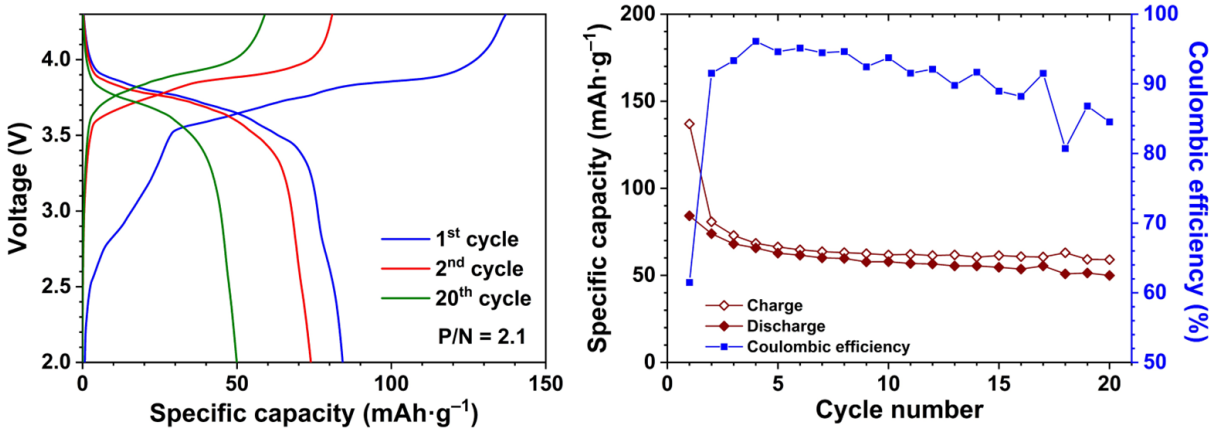

Figure 4.4. Galvanostatic profiles (left) of the 1st (blue), 2nd (red) and 20th (green) cycles and cycling retention (right) of graphite//MF21 coin cell at P/N = 2.1.

It is noticeable from the three-electrode experiments that SEI formation on graphite to some extent causes high capacity loss. Therefore, to optimize the P/N ratio, pre-cycled graphite electrodes are employed instead of fresh ones. As SEI formation occurs only in the first cycle (Figure 4.1c), graphite electrodes are cycled for one discharge/charge in half-cells, then reassembled with MF21 at P/N = 1.6, 1.7, 1.8, 2.0, 2.3, 2.6 in coin cells.

4.3.3. Cycling performance of precycled graphite//MF21 full cells

Figure 4.5 shows the cycling profiles of graphite//MF21 with SEI preformation. The galvanostatic curves of the first cycle at all ratios exhibit no significant difference with an average discharge voltage of *ca.* 3.6 V. Most of the cells display similar initial discharge capacity of *ca.* 110 mAh g^{-1} with ICE > 80 % (except P/N = 1.6). Apparently, SEI preformation of graphite significantly improves the performance in terms of initial discharge capacity and CE. The cycling retention and reversibility, in these conditions, rather depend on the P/N ratio. The graphite//MF21 full cell with the highest P/N ratio of 2.6 shows a remarkably terrible performance than the others. After 20 cycles, the CE is lower than 96 % and the battery loses 61 % of the initial discharge capacity (Table 4.1). In contrast, the cells with lower P/N ratios demonstrate better cycling retention with more than 50 % of the initial capacity remaining after 20 cycles. Surprisingly, a slight excess of either anode (P/N = 1.7, 1.8) or cathode (P/N = 2.3) display better results than the theoretical ratio (P/N = 2.0). The best cyclability is observed for the cell with P/N ratio of 1.8 with 76 % of the initial capacity remaining after 20 cycles and 65.5 % after 70 cycles (Table 4.1). The reversibility of the cell at this ratio increases faster than the other cells, reaching 98 % after 20 cycles and 99 % after 40 cycles. Although the cycling performance of this configuration is modest compared with several commercialized/published SIBs, PIBs and graphite//$LiFePO_4$ system (Table 4.2). with further optimizations, practical K-

ion cell with MnFe-PBA and graphite as electrodes could be a good candidate in the market of 4-volt batteries.

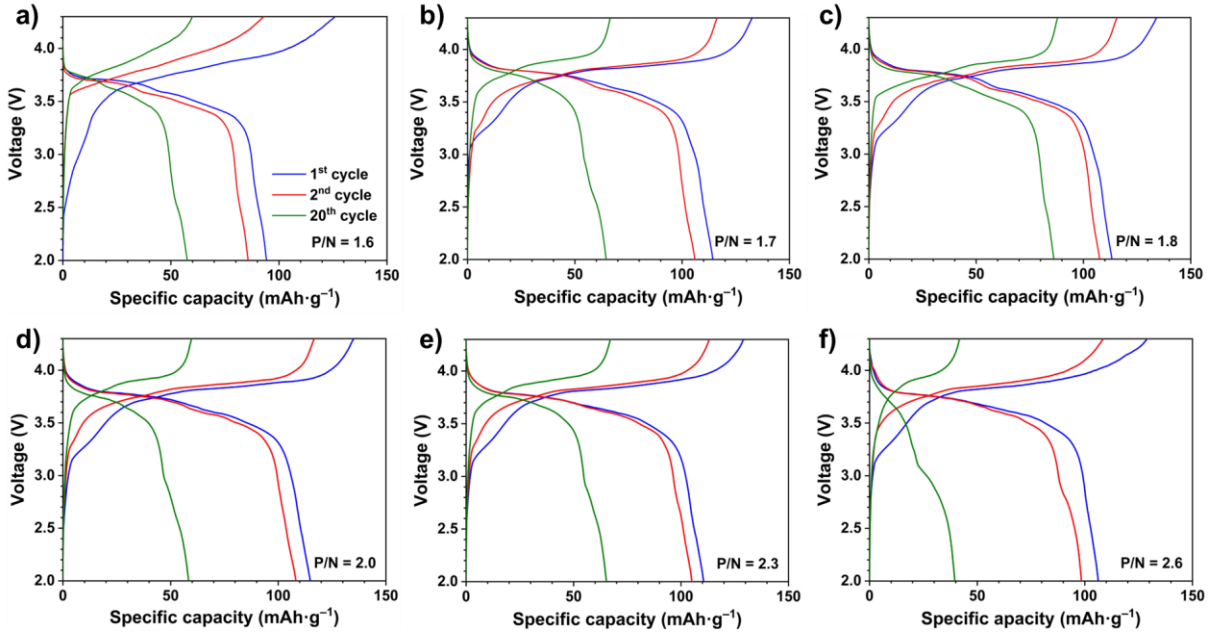

Figure 4.5. Galvanostatic profiles of the 1st (blue), 2nd (red) and 20th (green) cycles of graphite//MF21 full cells at the P/N ratios varying from 1.6 to 2.6 (respectively from (a) to (f)) recorded at the current density I = 10 mA g^{-1} versus MF21.

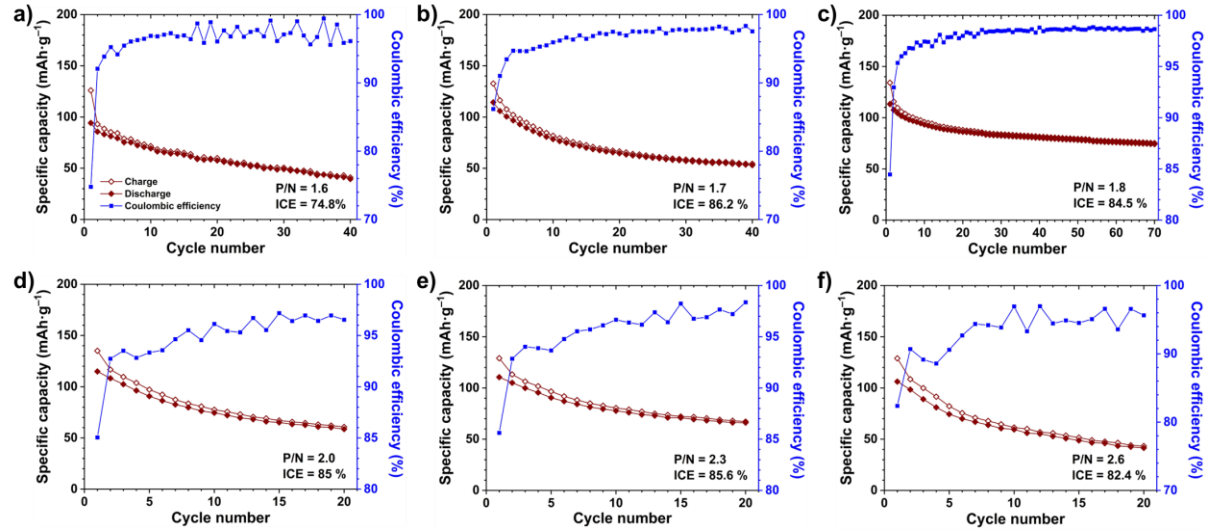

Figure 4.6. Cycling retention and coulombic efficiency of graphite//MF21 full cells at different P/N mass ratios, from 1.6 (a) to 2.6 (f) with a current density I = 10 mA g^{-1} versus MF21.

Table 4.1. Summary of cycling retention and CE of graphite//MF21 at P/N = 1.6-2.6 after 2,10,20, 40 and 70 cycles. The discharge capacity of each cycle is normalized to that of the first cycle.

P/N	**2nd cycle**		**10th cycle**		**20th cycle**		**40th cycle**		**70th cycle**	
	Norm. DC	CE (%)	Norm. DC	CE (%)	Norm. DC	CE (%)	Norm. DC	CE (%)	Norm. DC	CE (%)
1.6	0.910	92	0.736	97	0.611	96	0.419	96	–	–
1.7	0.926	91	0.686	96	0.565	97	0.464	98	–	–
1.8	0.949	93	0.823	97	0.761	98	0.710	99	0.655	99
2.0	0.942	93	0.649	96	0.510	96	–	–	–	–
2.3	0.951	93	0.703	97	0.598	98	–	–	–	–
2.6	0.927	93	0.560	97	0.390	96	–	–	–	–

Norm. DC: normalized discharge capacity

Table 4.2. Practical discharge capacity and cycling retention of a selection of SIBs and PIBs comparing with $LiFePO_4$ | graphite full cell.

Cathode	**Anode**	**Electrolyte**	**P/N ratio**	**Cell type**	**Potential range (V) / current density**	**Average operating voltage (V)**	**Q_{DC1} (mAh g^{-1}) / ICE (%) / number of cycles / retention (%)**	**Ref.**
$LiFePO_4$	Graphite	1 M $LiBF_4$ in EC-DEC (1:1)	N/A	Pouch cell	2.5 – 4.0 / C/2	3.2[6]	82 / N/A / 80 / 80	[252]
$Na_3V_2(PO_4)_2F_3$	Hard carbon	1 M $NaPF_6$ in EC-DMC (1:1)	N/A	18650 cell	2 – 4.25 / 1C (*)	3.4	~100 / 76.9 / 4000 / 80	[245]
$Na_xMnFe(CN)_6$	Hard carbon		N/A	Pouch cell	1.5 – 3.5 / 1C	3.3	~100 / N/A / 500 / >95	[246]
$K_{1.75}MnFe(CN)_6$	Graphite	0.7 M KPF_6 in EC-DEC (1:1)	N/A	CR2032	1.5 – 4.5 / 30 mA g^{-1}	3.5 – 3.6	110 / 60 / 60 / 74.5	[95]
$K_2MnFe(CN)_6$	Graphite	KFSI / $[C_3C_1pyrr][FSI]$	1.7		1.5 – 4.3 / 15 mA g^{-1}		91 / 58 / 200 / ~100	[249]
$K_2MnFe(CN)_6$	Graphite	7 mol kg^{-1} KFSI in DME	2.1		1.5 – 4.3 / 1C		104 / N/A / 100 / 85	[253]
$K_2MnFe(CN)_6$	Graphite	2.6 M KFSI in TEP	N/A		1.5 – 4.2 / 15 mA g^{-1}		79.6 / <45 / 30 / ~100	[247]
$K_2MnFe(CN)_6$	KC_8		2.0		2 – 4.25 / 0.5C		120 / >80 / 1000 / 80	[100]
$K_2MnFe(CN)_6$	Graphite(**)		1.67		1.5 – 4.2 / 15 mA g^{-1}		145 / ~99 / 110 / 91	[94]
MF21	Graphite(***)	5 M KTFSI in DME	1.8		2 – 4.3 / 10 mA g^{-1}		113 / 85 / 70 / 66	This work

(*)1C = 150 mA g^{-1} *(**) precycled graphite for 12 times* *(***) precycled graphite for 1 time*

[249,253] *electrolytes were pretreated with K metal*

4.4. Summary and perspective

The cycling performance of K-ion full cells using $K_{1.67}Mn_{0.65}Fe_{0.35}[Fe(CN)_6]$ (MF21) and graphite as electrodes in highly concentrated electrolyte was investigated with and without SEI preformation by precycling graphite in half cell vs. K metal. Severe issues such as overcharge or huge irreversibility coming from SEI formation were encountered when using directly fresh graphite electrodes in full cells, yet they can be tackled by using precycled graphite. With the positive-to-negative mass ratio of 1.8, equivalent to 10 % excess of graphite, the prototype MF21 | precycled graphite shows a promising performance with comparable outputs to the reported K-ion systems and typical $LiFePO_4$ | graphite cell. Indeed, it is too early to transfer this young technology to mass production, however, with further optimization on the materials, electrolyte, and cell configurations, PIBs based on PBA and graphite can join the race of 4-volt batteries.

GENERAL CONCLUSIONS AND PERSPECTIVES

PBAs and graphite are among the best positive and negative electrode active materials for PIBs, respectively. Both can deliver high specific capacities with good cyclability and therefore, PIB full cells with comparable energy and power densities to SIBs and graphite//$LiFePO_4$ LIBs. However, in practice several challenges remain.

The electrochemical performance of graphite strongly depends on three major factors which all originate in the electrolyte employed: the compatibility towards the electrode, the cation solvation, and the SEI formation. Glyme-based electrolytes were found to be more compatible to graphite than the carbonate electrolytes used in both SIBs and PIBs. Interestingly, an increased salt concentration in glyme-based electrolytes can modify the electrochemical mechanism: from K^+–solvent co-intercalation to bare K^+ intercalation, which is more favorable. The latter occurs at a lower potential (~0.2 V vs. ~0.8 V), delivers a close to two-fold capacity increase (~300 mAh g^{-1} vs.~170 mAh g^{-1}), and has much better capacity retention. By Raman spectroscopy combined with DFT calculations, the cation solvation was found to be a key factor altering the electrochemical mechanism when using 1, 3, and 5 M KFSI in DME. At lower salt concentrations (e.g., 1 M), the K^+ ions are surrounded by 2-3 DME molecules, while at 5 M, an HCE, less than 2. The complementary results also explain the transition from co-intercalation to intercalation observed at 3 M, the border between lower and higher concentrations. Here the SEI was somewhat surprisingly found to have no influence on directing the (co)intercalation mechanism, but to be an important factor for the capacity retention. Although the 5 M KFSI in DME electrolyte enhances the overall cell performance, electrolyte degradation leading to the very SEI formation from it hinders its use it in full cell application. The large contribution from SEI formation can cause a severe irreversibility, leading to rapid capacity fade and short cycle life Therefore, designing an electrolyte possessing an adequate cation solvation and forming a stable SEI with low contribution to the total capacity is essential to obtain practical PIBs based on graphite as negative electrode.

MF21 ($K_{1.67}Mn_{0.65}Fe_{0.35}[Fe(CN)_6]$), the representative of PBAs studied in this research demonstrate a high capacity (~ 130 mAh g^{-1}), and relatively good cyclability towards K metal. A complement of *ex situ* Mössbauer spectroscopy, *operando* XRD and *operando* XAS insightfully reveal the electrochemical mechanism of MF21, in terms of redox reactions of the TMs and structural evolution, which is summarized in Figure G1.

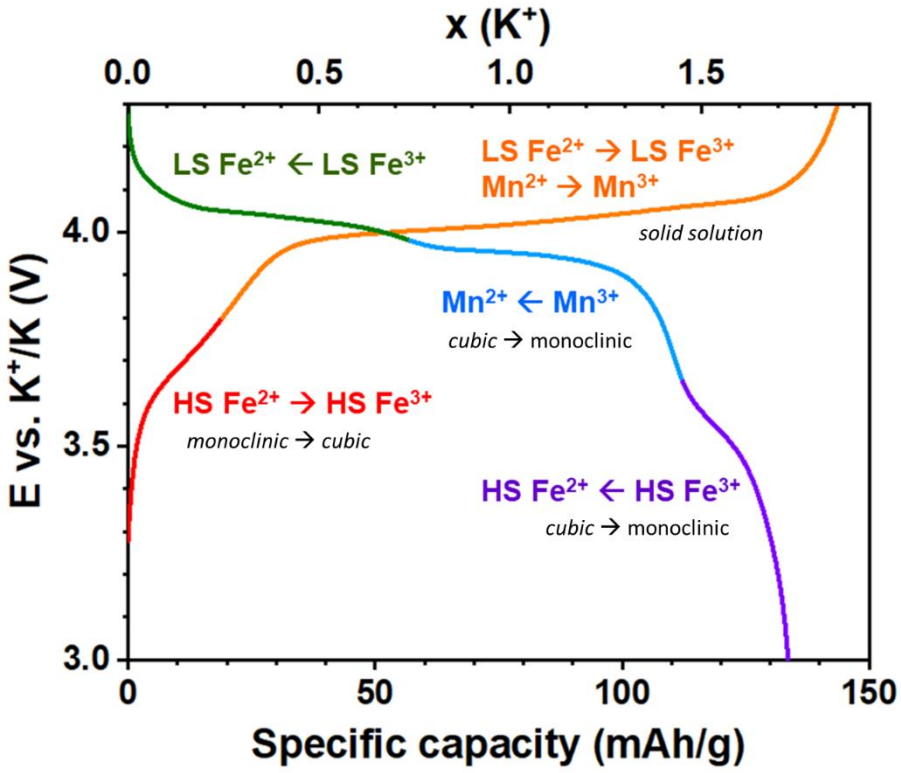

Figure G1. Galvanostatic profile of MF21 vs. K^+/K with identification of redox reactions and structural evolution.

Finding a good composition of two TM sites is a tricky task for PBAs. So far, Mn-Fe-based PBAs are the most attractive materials of this family. From the electrochemistry point of view, HS Mn is preferred to HS Fe, as the reactions $Mn^{2+} \leftrightarrow Mn^{3+}$ occur at higher potential (~ 4 V vs. K^+/K), and the Mn-contained PBAs delivered higher capacity.[95] EXAFS analysis on Mn K edge spectra shows a strong modification on the Mn–N bonding due to the Jahn-Teller effect. The Jahn-Teller effect causes a severe distortion in all dimensions (both axial and equatorial bonds) of the Mn in MF21, consequently, leads to the volume expansion observed in the XRD. However, this lattice distortion was mitigated by doping Fe at HS metal site. Perhaps, a slight increase in the HS Fe/Mn ratio can reduce the influence of Jahn-Teller effect but maintain the electrochemical merits of MnFe-PBAs. On the other hand, a modification of morphology and crystallinity via synthesis optimization can improve the performance. To date, the main synthetic route for PBAs is simple precipitation in aqueous solution. Adding a protector (e.g., ascorbic acid) can prevent the oxidation of HS Fe and the defects coming from coordinated water. Using chelating agent, such as EDTA, can slow down the reaction and increase the crystallinity.[94]

MF21 | precycled graphite full cell at the best P/N ratio (P/N = 1.8) displays high working potential (3.5-3.6 V) and good initial capacity (110 mAh g^{-1}), quite comparable to some SIBs

and $LiFePO_4$ | graphite LIBs. Finally, one important question: Is there any future for PIBs? Probably yes, but more efforts are required to enhance the reversibility and cyclability. Unlike LIBs, in PIBs, the SEI makes more contribution to the cycling performance of the cells. Therefore, the electrolyte composition must be optimized to reduce the contribution of SEI formation during the cell charging. Additionally, such factors as mass loading of the active materials, binder, electrode formulation, electrode area, separators, and even cell pressure play important roles in determination the lifetime of a PIB. The optimizations of these parameters will pave the way for PIBs to go to mass production.

SCIENTIFIC PRODUCTS

Publications:

(1) J. Touja, P. N. Le Pham, N. Louvain, L. Monconduit and L. Stievano, *Chem. Commun.*, **2020**, 56, 14673–14676.

(2) P. N. Le Pham, V. Gabaudan, A. Boulaoued, G. Åvall, F. Salles, P. Johansson, L. Monconduit and L. Stievano, *Energy Storage Materials*, **2022**, 45, 291–300.

Oral communications:

(1) *Cationic solvation of potassium bis(fluorosulfonyl) imide in monoglyme-based electrolytes: implications in the intercalation mechanism of K+ in graphite*, EUROMAT 2021, Visioconference.

(2) *Mössbauer and operando XAS investigation on the electrochemical mechanism of Prussian blue analogue in potassium-ion batteries*, 43èmes Journées du Groupe Francophone de Spectrométrie Mössbauer 2022, Nancy, France.

(3) *Prussian Blue Analogues for potassium-ion batteries: Application of complementary operando X-ray techniques*, 241st ECS Meeting 2022, Vancouver, Canada.

Poster:

(1) The details of the solvation of KFSI in DME: An electrolyte for potassium-ion batteries, Swiss Battery Days 2021, Switzerland (Visio).

REFERENCES

1. Poullikkas, A. A comparative overview of large-scale battery systems for electricity storage. *Renew. Sustain. Energy Rev.* **27**, 778–788 (2013).
2. Liang, Y. *et al.* A review of rechargeable batteries for portable electronic devices. *InfoMat* **1**, 6–32 (2019).
3. Alhamali, A., Farrag, M. E., Bevan, G. & Hepburn, D. M. Review of Energy Storage Systems in electric grid and their potential in distribution networks. in *2016 Eighteenth International Middle East Power Systems Conference (MEPCON)* 546–551 (IEEE, 2016). doi:10.1109/MEPCON.2016.7836945.
4. Kubota, K., Dahbi, M., Hosaka, T., Kumakura, S. & Komaba, S. Towards K-Ion and Na-Ion Batteries as "Beyond Li-Ion". *Chem. Rec.* **18**, 459–479 (2018).
5. Goodenough, J. B. & Park, K. S. The Li-ion rechargeable battery: A perspective. *J. Am. Chem. Soc.* **135**, 1167–1176 (2013).
6. Yang, Z. *et al.* Electrochemical Energy Storage for Green Grid. *Chem. Rev.* **111**, 3577–3613 (2011).
7. Kwade, A. *et al.* Current status and challenges for automotive battery production technologies. *Nat. Energy* **3**, 290–300 (2018).
8. Tian, Y. *et al.* Promises and Challenges of Next-Generation "Beyond Li-ion" Batteries for Electric Vehicles and Grid Decarbonization. *Chem. Rev.* **121**, 1623–1669 (2021).
9. Dunn, B., Kamath, H. & Tarascon, J.-M. Electrical Energy Storage for the Grid: A Battery of Choices. *Science* **334**, 928–935 (2011).
10. Whittingham, M. S. & Gamble, F. R. The lithium intercalates of the transition metal dichalcogenides. *Mater. Res. Bull.* **10**, 363–371 (1975).
11. Manthiram, A. A reflection on lithium-ion battery cathode chemistry. *Nat. Commun.* **11**, 1550 (2020).
12. Yoshino, A. The Birth of the Lithium-Ion Battery. *Angew. Chem. Int. Ed.* **51**, 5798–5800 (2012).
13. Yazami, R. & Touzain, Ph. A reversible graphite-lithium negative electrode for electrochemical generators. *J. Power Sources* **9**, 365–371 (1983).
14. Mizushima, K., Jones, P. C., Wiseman, P. J. & Goodenough, J. B. LixCoO2 (0<x<-1): A new cathode material for batteries of high energy density. *Mater. Res. Bull.* **15**, 783–789 (1980).
15. Reddy, M. V., Mauger, A., Julien, C. M., Paolella, A. & Zaghib, K. Brief History of Early Lithium-Battery Development. *Materials* **13**, 1884 (2020).
16. Xie, J. & Lu, Y.-C. A retrospective on lithium-ion batteries. *Nat. Commun.* **11**, 2499 (2020).
17. Zaghib, K. *et al.* An improved high-power battery with increased thermal operating range: C–$LiFePO_4$//C–$Li_4Ti_5O_{12}$. *J. Power Sources* **216**, 192–200 (2012).
18. Viswanathan, V. V. *et al.* Effect of entropy change of lithium intercalation in cathodes and anodes on Li-ion battery thermal management. *J. Power Sources* **195**, 3720–3729 (2010).

19. Kulova, T. L., Fateev, V. A., Seregina, E. A. & Grigoriev, A. S. A Brief Review of Post-Lithium-Ion Batteries. *Int. J. Electrochem. Sci.* **15**, 7242–7259 (2020).
20. Chapter 2 - Technologies of energy storage systems. in *Grid-scale Energy Storage Systems and Applications* (eds. Wu, F.-B., Yang, B. & Ye, J.-L.) 17–56 (Academic Press, 2019). doi:10.1016/B978-0-12-815292-8.00002-2.
21. Zhang, H. *et al.* From Solid-Solution Electrodes and the Rocking-Chair Concept to Today's Batteries. *Angew. Chem. Int. Ed.* **59**, 534–538 (2020).
22. Yabuuchi, N., Kubota, K., Dahbi, M. & Komaba, S. Research Development on Sodium-Ion Batteries. *Chem. Rev.* **114**, 11636–11682 (2014).
23. Xu, J. *et al.* Potassium-based electrochemical energy storage devices: Development status and future prospect. *Energy Storage Mater.* **34**, 85–106 (2021).
24. Ponrouch, A. *et al.* Multivalent rechargeable batteries. *Energy Storage Mater.* **20**, 253–262 (2019).
25. Arroyo-de Dompablo, M. E., Ponrouch, A., Johansson, P. & Palacín, M. R. Achievements, Challenges, and Prospects of Calcium Batteries. *Chem. Rev.* **120**, 6331–6357 (2020).
26. Fang, G., Zhou, J., Pan, A. & Liang, S. Recent Advances in Aqueous Zinc-Ion Batteries. *ACS Energy Lett.* **3**, 2480–2501 (2018).
27. Deng, J., Luo, W.-B., Chou, S.-L., Liu, H.-K. & Dou, S.-X. Sodium-Ion Batteries: From Academic Research to Practical Commercialization. *Adv. Energy Mater.* **8**, 1701428 (2018).
28. Taylor, S. R. Abundance of chemical elements in the continental crust: a new table. *Geochim. Cosmochim. Acta* **28**, 1273–1285 (1964).
29. Zhang, J. *et al.* Development status and future prospect of non-aqueous potassium ion batteries for large scale energy storage. *Nano Energy* **60**, 340–361 (2019).
30. Marcus, Y. Thermodynamic functions of transfer of single ions from water to nonaqueous and mixed solvents: Part 3 - Standard potentials of selected electrodes. *Pure Appl. Chem.* **57**, 1129–1132 (1985).
31. Komaba, S., Hasegawa, T., Dahbi, M. & Kubota, K. Potassium intercalation into graphite to realize high-voltage/high-power potassium-ion batteries and potassium-ion capacitors. *Electrochem. Commun.* **60**, 172–175 (2015).
32. Kim, H. *et al.* Sodium intercalation chemistry in graphite. *Energy Environ. Sci.* **8**, 2963–2969 (2015).
33. Okamoto, Y. Density Functional Theory Calculations of Alkali Metal (Li, Na, and K) Graphite Intercalation Compounds. *J. Phys. Chem. C* **118**, 16–19 (2014).
34. Stevens, D. A. & Dahn, J. R. The Mechanisms of Lithium and Sodium Insertion in Carbon Materials. *J. Electrochem. Soc.* **148**, A803 (2001).
35. Hosaka, T., Kubota, K., Hameed, A. S. & Komaba, S. Research Development on K-Ion Batteries. *Chem. Rev.* **120**, 6358–6466 (2020).
36. Fan, L., Ma, R., Zhang, Q., Jia, X. & Lu, B. Graphite Anode for a Potassium-Ion Battery with Unprecedented Performance. *Angew. Chem. Int. Ed.* **58**, 10500–10505 (2019).
37. Jian, Z., Luo, W. & Ji, X. Carbon Electrodes for K-Ion Batteries. *J. Am. Chem. Soc.* **137**, 11566–11569 (2015).

38. Luo, W. *et al.* Potassium Ion Batteries with Graphitic Materials. *Nano Lett.* **15**, 7671–7677 (2015).
39. Cohn, A. P. *et al.* Durable potassium ion battery electrodes from high-rate cointercalation into graphitic carbons. *J. Mater. Chem. A* **4**, 14954–14959 (2016).
40. Niu, X. *et al.* Salt-concentrated electrolytes for graphite anode in potassium ion battery. *Solid State Ion.* **341**, 115050 (2019).
41. Jache, B., Binder, J. O., Abe, T. & Adelhelm, P. A comparative study on the impact of different glymes and their derivatives as electrolyte solvents for graphite co-intercalation electrodes in lithium-ion and sodium-ion batteries. *Phys. Chem. Chem. Phys.* **18**, 14299–14316 (2016).
42. Zhang, L., Wang, W. (Alex), Lu, S. & Xiang, Y. Carbon Anode Materials: A Detailed Comparison between Na-ion and K-ion Batteries. *Adv. Energy Mater.* **11**, 2003640 (2021).
43. Kim, H. *et al.* Exploiting Lithium-Ether Co-Intercalation in Graphite for High-Power Lithium-Ion Batteries. *Adv. Energy Mater.* **7**, 1700418 (2017).
44. Liu, M. *et al.* Deciphering the paradox between the Co-intercalation of sodium-solvent into graphite and its irreversible capacity. *Energy Storage Mater.* **26**, 32–39 (2020).
45. Yoon, G., Kim, H., Park, I. & Kang, K. Conditions for Reversible Na Intercalation in Graphite: Theoretical Studies on the Interplay Among Guest Ions, Solvent, and Graphite Host. *Adv. Energy Mater.* **7**, 1601519 (2017).
46. Åvall, G. *et al.* Highly Concentrated Electrolytes: Electrochemical and Physicochemical Characteristics of $LiPF_6$ in Propylene Carbonate Solutions. *J. Electrochem. Soc.* **168**, 050521 (2021).
47. Madec, L. *et al.* Paving the Way for K-Ion Batteries: Role of Electrolyte Reactivity through the Example of Sb-Based Electrodes. *ACS Appl. Mater. Interfaces* **10**, 34116–34122 (2018).
48. Wu, X. *et al.* Effects of functional binders on electrochemical performance of graphite anode in potassium-ion batteries. *Ionics* **25**, 2563–2574 (2019).
49. An, Y. *et al.* Commercial expanded graphite as a low–cost, long-cycling life anode for potassium–ion batteries with conventional carbonate electrolyte. *J. Power Sources* **378**, 66–72 (2018).
50. Tai, Z., Zhang, Q., Liu, Y., Liu, H. & Dou, S. Activated carbon from the graphite with increased rate capability for the potassium ion battery. *Carbon* **123**, 54–61 (2017).
51. Liu, Q., Rao, A. M., Han, X. & Lu, B. Artificial SEI for Super high-Performance K-Graphite Anode. *Adv. Sci.* **8**, 2003639 (2021).
52. Jian, Z., Xing, Z., Bommier, C., Li, Z. & Ji, X. Hard Carbon Microspheres: Potassium-Ion Anode Versus Sodium-Ion Anode. *Adv. Energy Mater.* **6**, 1501874 (2016).
53. Dai, H. *et al.* Superior potassium storage behavior of hard carbon facilitated by ether-based electrolyte. *Carbon* **179**, 60–67 (2021).
54. Nanjundan, A. K. *et al.* Potassium-Ion Storage in Cellulose-Derived Hard Carbon: The Role of Functional Groups. *Batter. Supercaps* **3**, 953–960 (2020).

55. Au, H. *et al.* A revised mechanistic model for sodium insertion in hard carbons. *Energy Environ. Sci.* **13**, 3469–3479 (2020).
56. Yamamoto, H. *et al.* Synthesizing higher-capacity hard-carbons from cellulose for Na- and K-ion batteries. *J. Mater. Chem. A* **6**, 16844–16848 (2018).
57. Wang, W. *et al.* Short-Range Order in Mesoporous Carbon Boosts Potassium-Ion Battery Performance. *Adv. Energy Mater.* **8**, 1701648 (2018).
58. Katorova, N. S., Luchkin, S. Yu., Rupasov, D. P., Abakumov, A. M. & Stevenson, K. J. Origins of irreversible capacity loss in hard carbon negative electrodes for potassium-ion batteries. *J. Chem. Phys.* **152**, 194704 (2020).
59. Franklin, R. E. & Randall, J. T. Crystallite growth in graphitizing and non-graphitizing carbons. *Proc. R. Soc. Lond. Ser. Math. Phys. Sci.* **209**, 196–218 (1951).
60. Oberlin, A. & Terriere, G. Graphitization studies of anthracites by high resolution electron microscopy. *Carbon* **13**, 367–376 (1975).
61. Li, Z. *et al.* Low Temperature Pyrolyzed Soft Carbon as High Capacity K-Ion Anode. *ACS Appl. Energy Mater.* **2**, 4053–4058 (2019).
62. Liu, Y. *et al.* Pitch-Derived Soft Carbon as Stable Anode Material for Potassium Ion Batteries. *Adv. Mater.* **32**, 2000505 (2020).
63. Wang, B. *et al.* A comprehensive review of carbons anode for potassium-ion battery: fast kinetic, structure stability and electrochemical. *J. Power Sources* **484**, 229244 (2021).
64. Gabaudan, V., Berthelot, R., Stievano, L. & Monconduit, L. Inside the Alloy Mechanism of Sb and Bi Electrodes for K-Ion Batteries. *J. Phys. Chem. C* **122**, 18266–18273 (2018).
65. Kim, H. *et al.* Recent Progress and Perspective in Electrode Materials for K-Ion Batteries. *Adv. Energy Mater.* **8**, 1702384 (2018).
66. McCulloch, W. D., Ren, X., Yu, M., Huang, Z. & Wu, Y. Potassium-Ion Oxygen Battery Based on a High Capacity Antimony Anode. *ACS Appl. Mater. Interfaces* **7**, 26158–26166 (2015).
67. Gabaudan, V. *et al.* SnSb *vs.* Sn: improving the performance of Sn-based anodes for K-ion batteries by synergetic alloying with Sb. *J. Mater. Chem. A* **7**, 15262–15270 (2019).
68. Ramireddy, T. *et al.* Insights into Electrochemical Behavior, Phase Evolution and Stability of Sn upon K-alloying/de-alloying via In Situ Studies. *J. Electrochem. Soc.* **164**, A2360–A2367 (2017).
69. Wang, Q. *et al.* Reaction and Capacity-Fading Mechanisms of Tin Nanoparticles in Potassium-Ion Batteries. *J. Phys. Chem. C* **121**, 12652–12657 (2017).
70. Kishore, B., G, V. & Munichandraiah, N. $K_2Ti_4O_9$: A Promising Anode Material for Potassium Ion Batteries. *J. Electrochem. Soc.* **163**, A2551–A2554 (2016).
71. Dong, S. *et al.* Novel Potassium-Ion Hybrid Capacitor Based on an Anode of $K_2Ti_6O_{13}$ Microscaffolds. *ACS Appl. Mater. Interfaces* **10**, 15542–15547 (2018).
72. Han, J. *et al.* Exploration of $K_2Ti_8O_{17}$ as an anode material for potassium-ion batteries. *Chem. Commun.* **52**, 11274–11276 (2016).
73. Kraft, A. What a chemistry student should know about the history of Prussian blue. *ChemTexts* **4**, 16 (2018).

74. Peng, J. *et al.* Prussian Blue Analogues for Sodium-Ion Batteries: Past, Present, and Future. *Adv. Mater.* **34**, 2108384 (2022).
75. Yang, D. *et al.* Prussian blue without coordinated water as a superior cathode for sodium-ion batteries. *Chem. Commun.* **51**, 8181–8184 (2015).
76. Lu, Y., Wang, L., Cheng, J. & Goodenough, J. B. Prussian blue: a new framework of electrode materials for sodium batteries. *Chem. Commun.* **48**, 6544 (2012).
77. Yang, Y. *et al.* Prussian blue and its analogues as cathode materials for Na-, K-, Mg-, Ca-, Zn- and Al-ion batteries. *Nano Energy* **99**, 107424 (2022).
78. Hosaka, T. & Komaba, S. Development of Nonaqueous Electrolytes for High-Voltage K-Ion Batteries. *Bull. Chem. Soc. Jpn.* **95**, 569–581 (2022).
79. Hurlbutt, K., Wheeler, S., Capone, I. & Pasta, M. Prussian Blue Analogs as Battery Materials. *Joule* **2**, 1950–1960 (2018).
80. Wu, X. *et al.* Highly Crystallized $Na_2CoFe(CN)_6$ with Suppressed Lattice Defects as Superior Cathode Material for Sodium-Ion Batteries. *ACS Appl. Mater. Interfaces* **8**, 5393–5399 (2016).
81. Miessler, G. L. *Inorganic chemistry*. (Pearson Education India, 2008).
82. Ma, L. *et al.* Accommodating diverse ions in Prussian blue analogs frameworks for rechargeable batteries: The electrochemical redox reactions. *Nano Energy* **81**, 105632 (2021).
83. Chen, J. *et al.* Prussian blue, its analogues and their derived materials for electrochemical energy storage and conversion. *Energy Storage Mater.* **25**, 585–612 (2020).
84. Cattermull, J., Pasta, M. & Goodwin, A. L. Structural complexity in Prussian blue analogues. *Mater. Horiz.* **8**, 3178–3186 (2021).
85. Rajagopalan, R., Tang, Y., Ji, X., Jia, C. & Wang, H. Advancements and Challenges in Potassium Ion Batteries: A Comprehensive Review. *Adv. Funct. Mater.* **30**, 1909486 (2020).
86. Boström, H. L. B. & Brant, W. R. Octahedral tilting in Prussian blue analogues. *J. Mater. Chem. C* **10**, 13690–13699 (2022).
87. Li, W. *et al.* Chemical Properties, Structural Properties, and Energy Storage Applications of Prussian Blue Analogues. *Small* **15**, 1900470 (2019).
88. Li, H. *et al. Operando* Electrochemical X-ray Diffraction and Raman Spectroscopic Studies Revealing the Alkali-Metal Ion Intercalation Mechanism in Prussian Blue Analogues. *J. Phys. Chem. Lett.* **13**, 479–485 (2022).
89. Shi, W. *et al.* Berlin green-based battery deionization-highly selective potassium recovery in seawater. *Electrochimica Acta* **310**, 104–112 (2019).
90. Wu, X. *et al.* Low Defect $FeFe(CN)_6$ Framework as Stable Host Material for High Performance Li-Ion Batteries. *ACS Appl. Mater. Interfaces* **8**, 23706–23712 (2016).
91. Crumbliss, A. L., Lugg, P. S. & Morosoff, N. Alkali metal cation effects in a Prussian blue surface modified electrode. *Inorg. Chem.* **23**, 4701–4708 (1984).
92. Itaya, K., Uchida, I. & Neff, V. D. Electrochemistry of polynuclear transition metal cyanides: Prussian blue and its analogues. *Acc. Chem. Res.* **19**, 162–168 (1986).

93. Wu, X., Jian, Z., Li, Z. & Ji, X. Prussian white analogues as promising cathode for non-aqueous potassium-ion batteries. *Electrochem. Commun.* **77**, 54–57 (2017).
94. Deng, L. *et al.* Defect-free potassium manganese hexacyanoferrate cathode material for high-performance potassium-ion batteries. *Nat. Commun.* **12**, 2167 (2021).
95. Bie, X., Kubota, K., Hosaka, T., Chihara, K. & Komaba, S. A novel K-ion battery: hexacyanoferrate(II)/graphite cell. *J. Mater. Chem. A* **5**, 4325–4330 (2017).
96. Jiang, X., Zhang, T., Yang, L., Li, G. & Lee, J. Y. A Fe/Mn-Based Prussian Blue Analogue as a K-Rich Cathode Material for Potassium-Ion Batteries. *ChemElectroChem* **4**, 2237–2242 (2017).
97. Xue, L. *et al.* Low-Cost High-Energy Potassium Cathode. *J. Am. Chem. Soc.* **139**, 2164–2167 (2017).
98. Jiang, L. *et al.* Building aqueous K-ion batteries for energy storage. *Nat. Energy* **4**, 495–503 (2019).
99. Kjeldgaard, S. *et al.* Strategies for synthesis of Prussian blue analogues. *R. Soc. Open Sci.* **8**, 201779 (2021).
100. Wu, X. *et al.* The Quest for Stable Potassium-Ion Battery Chemistry. *Adv. Mater.* **34**, 2106876 (2022).
101. Hironaka, Y., Kubota, K. & Komaba, S. P2- and P3-K_xCoO_2 as an electrochemical potassium intercalation host. *Chem. Commun.* **53**, 3693–3696 (2017).
102. Hwang, J.-Y., Kim, J., Yu, T.-Y., Myung, S.-T. & Sun, Y.-K. Development of P3-$K_{0.69}CrO_2$ as an ultra-high-performance cathode material for K-ion batteries. *Energy Environ. Sci.* **11**, 2821–2827 (2018).
103. Wang, X. *et al.* Earth Abundant Fe/Mn-Based Layered Oxide Interconnected Nanowires for Advanced K-Ion Full Batteries. *Nano Lett.* **17**, 544–550 (2017).
104. Wu, X., Leonard, D. P. & Ji, X. Emerging Non-Aqueous Potassium-Ion Batteries: Challenges and Opportunities. *Chem. Mater.* **29**, 5031–5042 (2017).
105. Fedotov, S. S. *et al.* $AVPO_4F$ (A = Li, K): A 4 V Cathode Material for High-Power Rechargeable Batteries. *Chem. Mater.* **28**, 411–415 (2016).
106. Recham, N. *et al.* Preparation and Characterization of a Stable $FeSO_4F$-Based Framework for Alkali Ion Insertion Electrodes. *Chem. Mater.* **24**, 4363–4370 (2012).
107. Hosaka, T., Shimamura, T., Kubota, K. & Komaba, S. Polyanionic Compounds for Potassium-Ion Batteries. *Chem. Rec.* **19**, 735–745 (2019).
108. Wu, Z. *et al.* Potassium-ion battery cathodes: Past, present, and prospects. *J. Power Sources* **484**, 229307 (2021).
109. Chihara, K., Katogi, A., Kubota, K. & Komaba, S. $KVPO_4F$ and $KVOPO_4$ toward 4 volt-class potassium-ion batteries. *Chem. Commun.* **53**, 5208–5211 (2017).
110. Wernert, R. *et al.* Controlling the Cathodic Potential of $KVPO_4F$ through Oxygen Substitution. *Chem. Mater.* **34**, 4523–4535 (2022).
111. Fedotov, S. S., Samarin, A. S. & Antipov, E. V. $KTiOPO_4$-structured electrode materials for metal-ion batteries: A review. *J. Power Sources* **480**, 228840 (2020).
112. Li, M., Wang, C., Chen, Z., Xu, K. & Lu, J. New Concepts in Electrolytes. *Chem. Rev.* **120**, 6783–6819 (2020).

113. Touja, J., Le Pham, P. N., Louvain, N., Monconduit, L. & Stievano, L. Effect of the electrolyte on K-metal batteries. *Chem. Commun.* **56**, 14673–14676 (2020).
114. Wang, L. *et al.* Graphite as a potassium ion battery anode in carbonate-based electrolyte and ether-based electrolyte. *J. Power Sources* **409**, 24–30 (2019).
115. Zhang, C. *et al.* Chelate Effects in Glyme/Lithium Bis(trifluoromethanesulfonyl)amide Solvate Ionic Liquids, Part 2: Importance of Solvate-Structure Stability for Electrolytes of Lithium Batteries. *J. Phys. Chem. C* **118**, 17362–17373 (2014).
116. Hosaka, T., Matsuyama, T., Kubota, K., Tatara, R. & Komaba, S. KFSA/glyme electrolytes for 4 V-class K-ion batteries. *J. Mater. Chem. A* **8**, 23766–23771 (2020).
117. Xu, K. Electrolytes and Interphases in Li-Ion Batteries and Beyond. *Chem. Rev.* **114**, 11503–11618 (2014).
118. Wang, H., Zhai, D. & Kang, F. Solid electrolyte interphase (SEI) in potassium ion batteries. *Energy Environ. Sci.* **13**, 4583–4608 (2020).
119. He, G. & Nazar, L. F. Crystallite Size Control of Prussian White Analogues for Nonaqueous Potassium-Ion Batteries. *ACS Energy Lett.* **2**, 1122–1127 (2017).
120. Yoon, S. U., Kim, H., Jin, H.-J. & Yun, Y. S. Effects of fluoroethylene carbonate-induced solid-electrolyte-interface layers on carbon-based anode materials for potassium ion batteries. *Appl. Surf. Sci.* **547**, 149193 (2021).
121. Ells, A. W., May, R. & Marbella, L. E. Potassium Fluoride and Carbonate Lead to Cell Failure in Potassium-Ion Batteries. *ACS Appl. Mater. Interfaces* **13**, 53841–53849 (2021).
122. Li, Y., Lu, Y., Adelhelm, P., Titirici, M.-M. & Hu, Y.-S. Intercalation chemistry of graphite: alkali metal ions and beyond. *Chem. Soc. Rev.* **48**, 4655–4687 (2019).
123. Seidl, L. *et al.* Intercalation of solvated Na-ions into graphite. *Energy Environ. Sci.* **10**, 1631–1642 (2017).
124. Armand, M. & Tarascon, J.-M. Building better batteries. *Nature* **451**, 652–657 (2008).
125. Whittingham, M. S. Lithium Batteries and Cathode Materials. *Chem. Rev.* **104**, 4271–4302 (2004).
126. Larcher, D. & Tarascon, J.-M. Towards greener and more sustainable batteries for electrical energy storage. *Nat. Chem.* **7**, 19–29 (2015).
127. Ahmed, S. M., Suo, G., Wang, W. A., Xi, K. & Iqbal, S. B. Improvement in potassium ion batteries electrodes: Recent developments and efficient approaches. *J. Energy Chem.* **62**, 307–337 (2021).
128. Hui, J. *et al.* Achieving Fast and Efficient K^+ Intercalation on Ultrathin Graphene Electrodes Modified by a Li^+ Based Solid-Electrolyte Interphase. *J. Am. Chem. Soc.* **140**, 13599–13603 (2018).
129. Ding, H., Zhou, J., Rao, A. M. & Lu, B. Cell-like-carbon-micro-spheres for robust potassium anode. *Natl. Sci. Rev.* **8**, nwaa276 (2021).
130. Zhang, Q., Cheng, X., Wang, C., Rao, A. M. & Lu, B. Sulfur-assisted large-scale synthesis of graphene microspheres for superior potassium-ion batteries. *Energy Environ. Sci.* **14**, 965–974 (2021).

131. Chen, H. *et al.* Bifunctional Sulfonated Graphene-Modified $LiNi_{0.5}Mn_{1.5}O_4$ for Long-Life and High-Energy-Density Lithium-Ion Batteries. *ACS Appl. Energy Mater.* **4**, 5963–5972 (2021).
132. Zhao, J., Zou, X., Zhu, Y., Xu, Y. & Wang, C. Electrochemical Intercalation of Potassium into Graphite. *Adv. Funct. Mater.* **26**, 8103–8110 (2016).
133. Carboni, M., Naylor, A. J., Valvo, M. & Younesi, R. Unlocking high capacities of graphite anodes for potassium-ion batteries. *RSC Adv.* **9**, 21070–21074 (2019).
134. Qin, L. *et al.* Localized High-Concentration Electrolytes Boost Potassium Storage in High-Loading Graphite. *Adv. Energy Mater.* **9**, 1902618 (2019).
135. Xiao, N., McCulloch, W. D. & Wu, Y. Reversible Dendrite-Free Potassium Plating and Stripping Electrochemistry for Potassium Secondary Batteries. *J. Am. Chem. Soc.* **139**, 9475–9478 (2017).
136. Qian, Y. *et al.* Understanding mesopore volume-enhanced extra-capacity: Optimizing mesoporous carbon for high-rate and long-life potassium-storage. *Energy Storage Mater.* **29**, 341–349 (2020).
137. Kim, H., Yoon, G., Lim, K. & Kang, K. A comparative study of graphite electrodes using the co-intercalation phenomenon for rechargeable Li, Na and K batteries. *Chem. Commun.* **52**, 12618–12621 (2016).
138. Zhang, X. *et al.* Dendrite-Free and Long-Cycling Sodium Metal Batteries Enabled by Sodium-Ether Cointercalated Graphite Anode. *Adv. Funct. Mater.* **31**, 2009778 (2021).
139. Kim, H. *et al.* Sodium Storage Behavior in Natural Graphite using Ether-based Electrolyte Systems. *Adv. Funct. Mater.* **25**, 534–541 (2015).
140. Zhang, H., Yang, Y., Ren, D., Wang, L. & He, X. Graphite as anode materials: Fundamental mechanism, recent progress and advances. *Energy Storage Mater.* **36**, 147–170 (2021).
141. Jache, B. & Adelhelm, P. Use of Graphite as a Highly Reversible Electrode with Superior Cycle Life for Sodium-Ion Batteries by Making Use of Co-Intercalation Phenomena. *Angew. Chem. Int. Ed.* **53**, 10169–10173 (2014).
142. Goktas, M. *et al.* Graphite as Cointercalation Electrode for Sodium-Ion Batteries: Electrode Dynamics and the Missing Solid Electrolyte Interphase (SEI). *Adv. Energy Mater.* **8**, 1702724 (2018).
143. Westman, K. *et al.* Diglyme Based Electrolytes for Sodium-Ion Batteries. *ACS Appl. Energy Mater.* **1**, 2671–2680 (2018).
144. Jung, S. C., Kang, Y.-J. & Han, Y.-K. Origin of excellent rate and cycle performance of Na^+-solvent cointercalated graphite vs. poor performance of Li^+-solvent case. *Nano Energy* **34**, 456–462 (2017).
145. Zhang, X. *et al.* Comprehensive Insights into Electrolytes and Solid Electrolyte Interfaces in Potassium-Ion Batteries. *Energy Storage Mater.* **38**, 30–49 (2021).
146. Gu, M., Fan, L., Zhou, J., Rao, A. M. & Lu, B. Regulating Solvent Molecule Coordination with KPF_6 for Superstable Graphite Potassium Anodes. *ACS Nano* **15**, 9167–9175 (2021).
147. Liu, X. *et al.* Highly Concentrated KTFSI : Glyme Electrolytes for K/Bilayered-V_2O_5 Batteries. *Batter. Supercaps* **3**, 261–267 (2020).

148. Goutev, N., Ohno, K. & Matsuura, H. Raman Spectroscopic Study on the Conformation of 1,2-Dimethoxyethane in the Liquid Phase and in Aqueous Solutions. *J. Phys. Chem. A* **104**, 9226–9232 (2000).
149. Morcrette, M. *et al.* In situ X-ray diffraction techniques as a powerful tool to study battery electrode materials. *Electrochimica Acta* **47**, 3137–3149 (2002).
150. Frisch, M. J. *et al.* Gaussian 16 Revision A.03. (2016).
151. Zhao, Y. & Truhlar, D. G. The M06 suite of density functionals for main group thermochemistry, thermochemical kinetics, noncovalent interactions, excited states, and transition elements: two new functionals and systematic testing of four M06-class functionals and 12 other functionals. *Theor. Chem. Acc.* **120**, 215–241 (2008).
152. Tomasi, J., Mennucci, B. & Cammi, R. Quantum Mechanical Continuum Solvation Models. *Chem. Rev.* **105**, 2999–3094 (2005).
153. Hanwell, M. D. *et al.* Avogadro: an advanced semantic chemical editor, visualization, and analysis platform. *J. Cheminformatics* **4**, 17 (2012).
154. O'boyle, N. M., Tenderholt, A. L. & Langner, K. M. cclib: A library for package-independent computational chemistry algorithms. *J. Comput. Chem.* **29**, 839–845 (2008).
155. Kashinski, D. O. *et al.* Harmonic Vibrational Frequencies: Approximate Global Scaling Factors for TPSS, M06, and M11 Functional Families Using Several Common Basis Sets. *J. Phys. Chem. A* **121**, 2265–2273 (2017).
156. Rappe, A. K., Casewit, C. J., Colwell, K. S., Goddard, W. A. & Skiff, W. M. UFF, a full periodic table force field for molecular mechanics and molecular dynamics simulations. *J. Am. Chem. Soc.* **114**, 10024–10035 (1992).
157. Frenkel, D. & Smit, B. *Understanding molecular simulation: from algorithms to applications*. vol. 1 (Elsevier, 2001).
158. Goktas, M. *et al.* Stable and Unstable Diglyme-Based Electrolytes for Batteries with Sodium or Graphite as Electrode. *ACS Appl. Mater. Interfaces* **11**, 32844–32855 (2019).
159. Agubra, V. A. & Fergus, J. W. The formation and stability of the solid electrolyte interface on the graphite anode. *J. Power Sources* **268**, 153–162 (2014).
160. Mei, W., Jiang, L., Liang, C., Sun, J. & Wang, Q. Understanding of Li-plating on graphite electrode: detection, quantification and mechanism revelation. *Energy Storage Mater.* **41**, 209–221 (2021).
161. Birkenmaier, C., Bitzer, B., Harzheim, M., Hintennach, A. & Schleid, T. Lithium Plating on Graphite Negative Electrodes: Innovative Qualitative and Quantitative Investigation Methods. *J. Electrochem. Soc.* **162**, A2646–A2650 (2015).
162. Pramudita, J. C., Peterson, V. K., Kimpton, J. A. & Sharma, N. Potassium-ion intercalation in graphite within a potassium-ion battery examined using *in situ* X-ray diffraction. *Powder Diffr.* **32**, S43–S48 (2017).
163. Li, L. *et al.* Understanding High-Rate K^+ -Solvent Co-Intercalation in Natural Graphite for Potassium-Ion Batteries. *Angew. Chem. Int. Ed.* **59**, 12917–12924 (2020).
164. Yang, X., Su, Z., Wu, D., Hsu, S. L. & Stidham, H. D. Raman Analysis of a Conformational Distribution of Poly(ethylene oxide) and Its Model Compound in the Liquid State. *Macromolecules* **30**, 3796–3802 (1997).

165. Smith, G. D., Jaffe, R. L. & Yoon, D. Y. Conformations of 1,2-Dimethoxyethane in the Gas and Liquid Phases from Molecular Dynamics Simulations. *J. Am. Chem. Soc.* **117**, 530–531 (1995).

166. Ogawa, Y. *et al.* Vibration Spectra and Rotational Isomerism of Chain Molecules. V. 2,5-Dioxahexane, 2,5-Dithiahexane, and 2-Oxa-5-thiahexane. *Bull. Chem. Soc. Jpn.* **50**, 650–660 (1977).

167. Salama, M. *et al.* Unique Behavior of Dimethoxyethane (DME)/$Mg(N(SO_2CF_3)_2)_2$ Solutions. *J. Phys. Chem. C* **120**, 19586–19594 (2016).

168. Kashinski, D. O. *et al.* Harmonic Vibrational Frequencies: Approximate Global Scaling Factors for TPSS, M06, and M11 Functional Families Using Several Common Basis Sets. *J. Phys. Chem. A* **121**, 2265–2273 (2017).

169. Yamada, Y., Yaegashi, M., Abe, T. & Yamada, A. A superconcentrated ether electrolyte for fast-charging Li-ion batteries. *Chem. Commun.* **49**, 11194 (2013).

170. Jiang, L. *et al.* Inhibiting Solvent Co-Intercalation in a Graphite Anode by a Localized High-Concentration Electrolyte in Fast-Charging Batteries. *Angew. Chem. Int. Ed.* **60**, 3402–3406 (2021).

171. Wang, J. *et al.* Superconcentrated electrolytes for a high-voltage lithium-ion battery. *Nat. Commun.* **7**, 12032 (2016).

172. Kerner, M., Plylahan, N., Scheers, J. & Johansson, P. Thermal stability and decomposition of lithium bis(fluorosulfonyl)imide (LiFSI) salts. *RSC Adv.* **6**, 23327–23334 (2016).

173. Kimura, K., Motomatsu, J. & Tominaga, Y. Correlation between Solvation Structure and Ion-Conductive Behavior of Concentrated Poly(ethylene carbonate)-Based Electrolytes. *J. Phys. Chem. C* **120**, 12385–12391 (2016).

174. Xu, W. *et al.* A highly concentrated electrolyte for high-efficiency potassium metal batteries. *Chem. Commun.* **57**, 1034–1037 (2021).

175. Escher, I., Kravets, Y., Ferrero, G. A., Goktas, M. & Adelhelm, P. Strategies for Alleviating Electrode Expansion of Graphite Electrodes in Sodium-Ion Batteries Followed by In Situ Electrochemical Dilatometry. *Energy Technol.* **9**, 2000880 (2021).

176. Leifer, N., Greenstein, M. F., Mor, A., Aurbach, D. & Goobes, G. NMR-Detected Dynamics of Sodium Co-Intercalation with Diglyme Solvent Molecules in Graphite Anodes Linked to Prolonged Cycling. *J. Phys. Chem. C* **122**, 21172–21184 (2018).

177. Liu, Q., Wu, F., Mu, D. & Wu, B. A theoretical study on Na^+ solvation in carbonate ester and ether solvents for sodium-ion batteries. *Phys. Chem. Chem. Phys.* **22**, 2164–2175 (2020).

178. Matsuda, T., Takachi, M. & Moritomo, Y. A sodium manganese ferrocyanide thin film for Na-ion batteries. *Chem. Commun.* **49**, 2750 (2013).

179. Lee, H.-W. *et al.* Manganese hexacyanomanganate open framework as a high-capacity positive electrode material for sodium-ion batteries. *Nat. Commun.* **5**, 5280 (2014).

180. Lim, C. Q. X. & Tan, Z.-K. Prussian White with Near-Maximum Specific Capacity in Sodium-Ion Batteries. *ACS Appl. Energy Mater.* **4**, 6214–6220 (2021).

181. Zhao, S. *et al.* The Rise of Prussian Blue Analogs: Challenges and Opportunities for High-Performance Cathode Materials in Potassium-Ion Batteries. *Small Struct.* **2**, 2000054 (2021).

182. Wang, B. *et al.* Prussian Blue Analogs for Rechargeable Batteries. *iScience* **3**, 110–133 (2018).
183. Arabolla Rodríguez, R. *et al.* Unveiling the role of Mn-interstitial defect and particle size on the Jahn-Teller distortion of the LiMn2O4 cathode material. *J. Power Sources* **490**, 229519 (2021).
184. Fichtner, M. Recent Research and Progress in Batteries for Electric Vehicles. *Batter. Supercaps* **5**, 1–10 (2022).
185. Au, H., Crespo-Ribadeneyra, M. & Titirici, M.-M. Beyond Li-ion batteries: performance, materials diversification, and sustainability. *One Earth* **5**, 207–211 (2022).
186. Anoopkumar, V., Bibin, J. & Mercy, T. D. Potassium-Ion Batteries: Key to Future Large-Scale Energy Storage? *ACS Appl. Energy Mater.* **3**, 9478–9492 (2020).
187. Yang, Y. *et al.* Prussian blue and its analogues as cathode materials for Na-, K-, Mg-, Ca-, Zn- and Al-ion batteries. *Nano Energy* **99**, 107424 (2022).
188. Hurlbutt, K., Wheeler, S., Capone, I. & Pasta, M. Prussian Blue Analogs as Battery Materials. *Joule* **2**, 1950–1960 (2018).
189. Zhou, A. *et al.* Hexacyanoferrate-Type Prussian Blue Analogs: Principles and Advances Toward High-Performance Sodium and Potassium Ion Batteries. *Adv. Energy Mater.* **11**, 2000943 (2021).
190. Deng, L. *et al.* Defect-free potassium manganese hexacyanoferrate cathode material for high-performance potassium-ion batteries. *Nat. Commun.* **12**, 2167 (2021).
191. Paolella, A. *et al.* A review on hexacyanoferrate-based materials for energy storage and smart windows: challenges and perspectives. *J. Mater. Chem. A* **5**, 18919–18932 (2017).
192. Chen, J. *et al.* Prussian blue, its analogues and their derived materials for electrochemical energy storage and conversion. *Energy Storage Mater.* **25**, 585–612 (2020).
193. Du, G. & Pang, H. Recent advancements in Prussian blue analogues: Preparation and application in batteries. *Energy Storage Mater.* **36**, 387–408 (2021).
194. Ma, L. *et al.* Accommodating diverse ions in Prussian blue analogs frameworks for rechargeable batteries: The electrochemical redox reactions. *Nano Energy* **81**, 105632 (2021).
195. Shi, W. *et al.* Berlin green-based battery deionization-highly selective potassium recovery in seawater. *Electrochimica Acta* **310**, 104–112 (2019).
196. Wu, X. *et al.* Low Defect $FeFe(CN)_6$ Framework as Stable Host Material for High Performance Li-Ion Batteries. *ACS Appl. Mater. Interfaces* **8**, 23706–23712 (2016).
197. Crumbliss, A. L., Lugg, P. S. & Morosoff, N. Alkali metal cation effects in a Prussian blue surface modified electrode. *Inorg. Chem.* **23**, 4701–4708 (1984).
198. Itaya, K., Uchida, I. & Neff, V. D. Electrochemistry of polynuclear transition metal cyanides: Prussian blue and its analogues. *Acc. Chem. Res.* **19**, 162–168 (1986).
199. Moritomo, Y., Urase, S. & Shibata, T. Enhanced battery performance in manganese hexacyanoferrate by partial substitution. *Electrochimica Acta* **210**, 963–969 (2016).
200. Zhou, A. *et al.* Size-, Water-, and Defect-Regulated Potassium Manganese Hexacyanoferrate with Superior Cycling Stability and Rate Capability for Low-Cost Sodium-Ion Batteries. *Small* **15**, 1902420 (2019).

201. Bie, X., Kubota, K., Hosaka, T., Chihara, K. & Komaba, S. A novel K-ion battery: hexacyanoferrate(ii)/graphite cell. *J Mater Chem A* **5**, 4325–4330 (2017).
202. Xue, L. *et al.* Low-Cost High-Energy Potassium Cathode. *J Am Chem Soc* **139**, 2164–2167 (2017).
203. Deng, L. *et al.* Defect-free potassium manganese hexacyanoferrate cathode material for high-performance potassium-ion batteries. *Nat. Commun* **12**, 2167 (2021).
204. Mullaliu, A., Asenbauer, J., Aquilanti, G., Passerini, S. & Giorgetti, M. Highlighting the Reversible Manganese Electroactivity in Na-Rich Manganese Hexacyanoferrate Material for Li- and Na-Ion Storage. *Small Methods* **4**, 1900529 (2020).
205. Li, Y., Lam, K. H. & Hou, X. Reactant Concentration and Aging-Time-Regulated Potassium Manganese Hexacyanoferrate as a Superior Cathode for Sodium-Ion Batteries. *ACS Appl. Energy Mater.* **4**, 13098–13109 (2021).
206. Li, J. *et al.* Tin modification of sodium manganese hexacyanoferrate as a superior cathode material for sodium ion batteries. *Electrochimica Acta* **342**, 135928 (2020).
207. Matsuda, T., Takachi, M. & Moritomo, Y. A sodium manganese ferrocyanide thin film for Na-ion batteries. *Chem. Commun.* **49**, 2750 (2013).
208. Jo, I.-H., Lee, S.-M., Kim, H.-S. & Jin, B.-S. Electrochemical properties of $NaxMnFe(CN)_6 \cdot zH_2O$ synthesized in a Taylor-Couette reactor as a Na-ion battery cathode material. *J. Alloys Compd.* **729**, 590–596 (2017).
209. Camacho, P. S. *et al.* Impact of Synthesis Conditions in Na-Rich Prussian Blue Analogues. *ACS Appl. Mater. Interfaces* **13**, 42682–42692 (2021).
210. Morozova, P. A. *et al.* Exploring the Role of Crystal Water in Potassium Manganese Hexacyanoferrate as a Cathode Material for Potassium-Ion Batteries. *Crystals* **11**, 895 (2021).
211. Sun, Y. *et al.* Potassium manganese hexacyanoferrate/graphene as a high-performance cathode for potassium-ion batteries. *New J Chem* **43**, 11618–11625 (2019).
212. Jiang, M., Hou, Z., Ren, L., Zhang, Y. & Wang, J.-G. Prussian blue and its analogues for aqueous energy storage: From fundamentals to advanced devices. *Energy Storage Mate* **50**, 618–640 (2022).
213. Onuma, H. *et al.* Application of Ionic Liquid as K-Ion Electrolyte of Graphite//$K_2Mn[Fe(CN)_6]$ Cell. *ACS Energy Lett.* **5**, 2849–2857 (2020).
214. Bie, X., Kubota, K., Hosaka, T., Chihara, K. & Komaba, S. A novel K-ion battery: hexacyanoferrate(II)/graphite cell. *J. Mater. Chem. A* **5**, 4325–4330 (2017).
215. Xue, L. *et al.* Low-Cost High-Energy Potassium Cathode. *J. Am. Chem. Soc.* **139**, 2164–2167 (2017).
216. Lu, Y., Wang, L., Cheng, J. & Goodenough, J. B. Prussian blue: A new framework of electrode materials for sodium batteries. *Chem. Commun.* **48**, 6544–6546 (2012).
217. Wang, L. *et al.* Rhombohedral Prussian White as Cathode for Rechargeable Sodium-Ion Batteries. *J. Am. Chem. Soc.* **137**, 2548–2554 (2015).
218. Pasta, M. *et al.* Manganese-cobalt hexacyanoferrate cathodes for sodium-ion batteries. *J. Mater. Chem. A* **4**, 4211–4223 (2016).

219. Giorgetti, M. & Stievano, L. X-Ray Absorption Spectroscopy Study of Battery Materials. in *X-ray Characterization of Nanostructured Energy Materials by Synchrotron Radiation* (eds. Khodaei, M. & Petaccia, L.) 51–75 (InTech, 2017). doi:10.5772/66868.
220. Fehse, M., Iadecola, A., Simonelli, L., Longo, A. & Stievano, L. The rise of X-ray spectroscopies for unveiling the functional mechanisms in batteries. *Phys. Chem. Chem. Phys.* **23**, 23445–23465 (2021).
221. Mullaliu, A. *et al.* Operando XAFS and XRD Study of a Prussian Blue Analogue Cathode Material: Iron Hexacyanocobaltate. *Condens. Matter* **3**, 36 (2018).
222. Hayakawa, K. *et al.* Full Quantitative Multiple-Scattering Analysis of X-ray Absorption Spectra: Application to Potassium Hexacyanoferrat(II) and -(III) Complexes. *J. Am. Chem. Soc.* **126**, 15618–15623 (2004).
223. Aquilanti, G. *et al.* Operando characterization of batteries using x-ray absorption spectroscopy: Advances at the beamline XAFS at synchrotron Elettra. *J. Phys. Appl. Phys.* **50**, 074001 (2017).
224. Mullaliu, A. *et al.* Copper Electroactivity in Prussian Blue-Based Cathode Disclosed by Operando XAS. *J. Phys. Chem. C* **122**, 15868–15877 (2018).
225. Fehse, M. *et al.* Applying chemometrics to study battery materials: Towards the comprehensive analysis of complex operando datasets. *Energy Storage Mater.* **18**, 328–337 (2019).
226. Rodriguez-Carvajal, J. FullProf 2000: A Rietveld refinement and pattern matching analysis program. *Newsletter* **26**, 12–19 (2001).
227. Aquilanti, G. *et al. Operando* characterization of batteries using x-ray absorption spectroscopy: advances at the beamline XAFS at synchrotron Elettra. *J. Phys. Appl. Phys.* **50**, 074001 (2017).
228. Ravel, B. & Newville, M. ATHENA, ARTEMIS, HEPHAESTUS: data analysis for X-ray absorption spectroscopy using IFEFFIT. *J. Synchrotron Radiat.* **12**, 537–541 (2005).
229. Morcrette, M. *et al.* In situ X-ray diffraction techniques as a powerful tool to study battery electrode materials. *Electrochim Acta* **47**, 3137–3149 (2002).
230. Jiang, X., Zhang, T., Yang, L., Li, G. & Lee, J. Y. A Fe/Mn-Based Prussian Blue Analogue as a K-Rich Cathode Material for Potassium-Ion Batteries. *ChemElectroChem* **4**, 2237–2242 (2017).
231. Jiang, L. *et al.* Building aqueous K-ion batteries for energy storage. *Nat. Energy* **4**, 495–503 (2019).
232. Parajuli, D., Tanaka, H., Sakurai, K., Hakuta, Y. & Kawamoto, T. Thermal Decomposition Behavior of Prussian Blue in Various Conditions. *Materials* **14**, 1151 (2021).
233. Samain, L., Gilbert, B., Grandjean, F., Long, G. J. & Strivay, D. Redox reactions in Prussian blue containing paint layers as a result of light exposure. *J. Anal. At. Spectrom.* **28**, 524 (2013).
234. Okubo, M. *et al.* Ion-induced transformation of magnetism in a bimetallic CuFe Prussian blue analogue. *Angew. Chem. - Int. Ed.* **50**, 6269–6273 (2011).
235. Ojwang, D. O. *et al.* Structure Characterization and Properties of K-Containing Copper Hexacyanoferrate. *Inorg. Chem.* **55**, 5924–5934 (2016).

236. Miessler, G. L. *Inorganic chemistry*. (Pearson Education India, 2008).

237. Tian, C., Kan, E., Lee, C. & Whangbo, M.-H. π-Back-Donation Effect of the Cyanide Ligands on the Electron Correlation and Charge Transfer in Prussian Blue $RbMn[Fe(CN)_6]$. *Inorg. Chem.* **49**, 3086–3088 (2010).

238. Iadecola, A., Perea, A., Aldon, L., Aquilanti, G. & Stievano, L. Li deinsertion mechanism and Jahn–Teller distortion in $LiFe_{0.75}Mn_{0.25}PO_4$: an *operando* x-ray absorption spectroscopy investigation. *J. Phys. Appl. Phys.* **50**, 144004 (2017).

239. Mullaliu, A., Aquilanti, G., Conti, P., Giorgetti, M. & Passerini, S. Effect of Water and Alkali-Ion Content on the Structure of Manganese(II) Hexacyanoferrate(II) by a Joint Operando X-ray Absorption Spectroscopy and Chemometric Approach. *ChemSusChem* **13**, 608–615 (2020).

240. Lee, J.-H., Bae, J.-G., Lee, H. J. & Lee, J. H. Unveiling anomalous lattice shrinkage induced by Pi-backbonding in Prussian blue analogues. *J. Energy Chem.* **70**, 121–128 (2022).

241. Cattermull, J., Pasta, M. & Goodwin, A. L. Structural complexity in Prussian blue analogues. *Mater. Horiz.* **8**, 3178–3186 (2021).

242. Sugimoto, M. *et al.* Increase in the Magnetic Ordering Temperature (Tc) as a Function of the Applied Pressure for A2Mn[Mn(CN)6] (A = K, Rb, Cs) Prussian Blue Analogues. *Inorg. Chem.* **56**, 10452–10457 (2017).

243. Zhu, Y. *et al.* Selective edge etching to improve the rate capability of Prussian blue analogues for sodium ion batteries. *Inorg. Chem. Front.* **6**, 1361–1366 (2019).

244. Wang, W. *et al.* Reversible structural evolution of sodium-rich rhombohedral Prussian blue for sodium-ion batteries. *Nat. Commun.* **11**, 980 (2020).

245. Broux, T. *et al.* High Rate Performance for Carbon-Coated $Na_3V_2(PO_4)_2F_3$ in Na-Ion Batteries. *Small Methods* **3**, 1800215 (2019).

246. Bauer, A. *et al.* The Scale-up and Commercialization of Nonaqueous Na-Ion Battery Technologies. *Adv. Energy Mater.* **8**, 1702869 (2018).

247. Zhang, J. *et al.* Low-defect $K_2Mn[Fe(CN)_6]$-reduced graphene oxide composite for high-performance potassium-ion batteries. *Chem. Commun.* **57**, 8632–8635 (2021).

248. Lei, Y. *et al.* Unveiling the influence of electrode/electrolyte interface on the capacity fading for typical graphite-based potassium-ion batteries. *Energy Storage Mater.* **24**, 319–328 (2020).

249. Onuma, H. *et al.* Application of Ionic Liquid as K-Ion Electrolyte of Graphite//$K_2Mn[Fe(CN)_6]$ Cell. *ACS Energy Lett.* **5**, 2849–2857 (2020).

250. Kasnatscheew, J. *et al.* A Tutorial into Practical Capacity and Mass Balancing of Lithium Ion Batteries. *J. Electrochem. Soc.* **164**, A2479–A2486 (2017).

251. Touja, J., Le Pham, P. N., Louvain, N., Monconduit, L. & Stievano, L. Effect of the electrolyte on K-metal batteries. *Chem. Commun.* **56**, 14673–14676 (2020).

252. Shim, J. & Striebel, K. A. Cycling performance of low-cost lithium ion batteries with natural graphite and LiFePO4. *J. Power Sources* **119–121**, 955–958 (2003).

253. Hosaka, T., Kubota, K., Kojima, H. & Komaba, S. Highly concentrated electrolyte solutions for 4 V class potassium-ion batteries. *Chem. Commun.* **54**, 8387–8390 (2018).

Abstract

In the last two decades, Li-ion batteries have become predominant in the market of energy storage. Their production, however, cannot satisfy the exponentially growing energy demand nor the urge to electrify our society, which requires alternative technologies with lower cost but comparable energy densities. Na-ion batteries are making their ways into mass production, and recently, the science community shift their interest to K-ion batteries, which have been identified as a promising alternative with interesting performance and reasonable production cost.

This thesis was developed based on two major objectives: (i) understanding the electrochemical mechanism of graphite and of a representative Prussian blue analogue (PBA), which are respectively among leading negative and positive electrode materials for K-ion batteries, and (ii) coupling them to make a K-ion full cell. This work has been carried out in collaboration between ICGM and Chalmers University of Technology.

The influence of electrolyte concentration on the (co-)intercalation mechanisms of graphite has been thoroughly investigated by *operando* XRD, FT-Raman spectroscopy combined with DFT calculations. The solvation properties of electrolytes were found to be the principal factor governing the mechanism, which helps determining a suitable electrolyte for graphite. The electrochemistry of PBAs strongly depends on the structural evolution during cycling. the combination of *operando* (XRD, XAS) and *ex situ* (Mössbauer spectroscopy) techniques for studying a Mn-Fe-based PBA provides fruitful details on the reaction mechanism and helps explaining the cycling performance of this material in K-ion batteries.

In full cell, the formation of a solid electrolyte interphase (SEI) on graphite is the main cause of battery failure. An elimination of SEI formation by using precycled graphite helps determining the optimal mass ratio of two materials to obtain the best performance. Although the preliminary results do not approach those of current Li-ion and Na-ion technologies, with further optimizations of electrode and electrolytes formulation, K-ion batteries can be one of the possible energy storage technologies of the future.

Keywords: K-ion batteries, graphite, Prussian blue analogues, mechanism, full cell.

Résumé

Ces dernières années, les batteries Li-ion ont été prédominantes sur le marché du stockage de l'énergie. Cependant, leur production ne peut satisfaire la demande énergétique croissante ni l'électrification de la société, qui nécessite des technologies alternatives à moindre coût et des densités énergétiques comparables. Les batteries Na-ion sont en train de faire leur chemin vers la production de masse, et récemment, la communauté scientifique s'est tournée vers les batteries K-ion, qui ont été identifiées comme une alternative prometteuse avec des performances intéressantes et un coût de production raisonnable.

Cette thèse a été développée autour de deux objectifs majeurs : (i) comprendre le mécanisme électrochimique du graphite et d'un analogue du Bleu de Prusse (PBA), qui comptent respectivement parmi les principaux matériaux d'électrode négative et positive pour les batteries K-ion, et (ii) former une cellule complète K-ion en les couplant. Ce travail, financé par ALISTORE ERI a été réalisé en collaboration entre l'ICGM et la Chalmers University of Technology.

L'influence de la concentration d'électrolyte sur les mécanismes de (co-)intercalation du graphite a été étudiée en profondeur par la DRX en mode *operando*, et par spectroscopie FT-Raman combinée à des calculs DFT. Les propriétés de solvatation des électrolytes se sont révélées être le principal facteur régissant le mécanisme, ce qui pourra aider le choix d'un électrolyte adapté au graphite. L'électrochimie des PBA dépend fortement de l'évolution structurale au cours du cyclage. La combinaison des techniques *operando* (XRD, XAS) et *ex situ* (spectroscopie Mössbauer) appliquées à un PBA de référence à base de Mn et Fe apporte des précisions cruciales sur le mécanisme de réaction et permet d'expliquer les performances en cyclage de ce matériau en batterie K-ion.

En cellule complète, l'étape de formation de formation de la Solid Electrolyte Interphase (SEI) sur le graphite est la principale cause de défaillance de la batterie. L'élimination partielle de cette étape en utilisant du graphite précyclé aide à optimiser le rapport massique des deux matériaux afin d'obtenir les meilleures performances. Bien que les résultats préliminaires ne se rapprochent pas encore de ceux des technologies Li-ion et Na-ion actuelles, et nécessitent des optimisations supplémentaires des formulations d'électrodes et d'électrolytes, les batteries K-ion pourraient devenir l'une des technologies de stockage d'énergie possibles du futur.

Mots clés : batteries K-ion, graphite, analogues du Bleu de Prusse, mécanisme, cellules complètes.